3D Simulation of the Quasilinear Electron-Langmuir Wave Interaction in Type III Solar Radio Bursts

A thesis submitted for the degree of
Doctor of Philosophy

by

James Harding

School of Physics
University of Sydney
Australia

September, 2020

Dedicated to Minh,
with love and gratitude

Declaration of originality

To the best of my knowledge, this thesis contains no copy or paraphrase of work published by another person, except where duly acknowledged in the text. This thesis contains no material which has previously been presented for a degree at the University of Sydney or any other university.

James Harding

Included papers and attribution

Chapter 2 **Offset Power-Law Dependence of the Sun's Radial Electron Density Profile: Evidence and Implications**
J.C Harding, Iver H. Cairns, and Vasily V. Lobzin,
Published in The Astrophysical Journal, *877*,1 (2019).

I was primarily responsible for this work.

Chapter 3 **Electron-Langmuir wave resonance in three dimensions**
J.C. Harding, I. H. Cairns, and D.B. Melrose,
Published in Physics of Plasmas,*27*,2 2020.

I was primarily responsible for this work.

Acknowledgements

Primary thanks are due to my supervisor, Prof. Iver Cairns, with whom I first worked as a first year student in 2012. Iver has generously given me many invaluable research opportunities and has supported me graciously through all my studies. My associate supervisor, Prof. Don Melrose, has been a huge influence and support in finishing this PhD. I would like to extend special thanks to the undergraduate teaching coordinators A/Prof. Joe Khachan, A/Prof. Helen Johnston, Prof. Manjula Sharma, A/Prof. Sergio Leon-Saval and everyone I worked with at the School of Physics over the years. Teaching with them all was a true pleasure and an unmatchable learning experience.

I met my boyfriend Minh as I was about to begin my Honours year, so he hasn't known me when I wasn't studying and researching, with this thesis always at the back of my mind. To him go my eternal thanks for showing interest, giving advice and putting up with me during these years. This "space maths" work is for you.

Several people have made my time at the School of Physics at the University of Sydney enjoyable and worthwhile. There were many days when having coffee at Ralph's with Samira Tasnim got me through. If friendship with her was the sole reward of 4 years' work it would've been worth it. Patrick McCauley and Ron Maj made the office an exciting and bright place to come to work, and if we just had a few more years I'm sure we'd have solved the world's crises (at least the really major ones). And I can't imagine completing this without the frequent company of Jodie Vo, which comes with compulsory gin and cheese.

My family, particularly my father Chris and mother Teresa, were an essential support for me in various ways during my candidature. Thank you very much for getting me over the finish line.

My comrades at the University of Sydney NTEU allowed me, despite my greenness, to cut my teeth and help them to fight for a better university. Staff working conditions are indeed student learning conditions.

Lastly, I acknowledge the financial support of an Australian Government Research Training Program (RTP) scholarship, and a Postgraduate Research Support Scheme (PRSS) travel scholarship.

Abstract

This thesis presents a three-dimensional relativistically correct model of the electron beam-Langmuir wave interaction in the solar corona, as well as a model of the radial electron density profile of the ambient solar plasma through which an electron beam passes. 1D models of the beam/plasma interaction have long been used, as have empirical fits for the electron density profile. In support of the overall goal of this thesis, to develop a more realistic understanding of the plasma physics processes underlying Type III solar radio bursts, we first present strong evidence for a new and physically significant analytic model for the radial density profile in the corona. The thesis then demonstrates the need to develop a 3D picture of the resonance between streaming electrons and Langmuir waves, and the coupled evolution of this system. A new picture of quasilinear relaxation of electron beams is described qualitatively and quantitatively. This 3D picture changes the way electron distributions are considered in terms of their stability or instability to the growth of Langmuir waves. The thesis also develops a numerical method utilising the analytical development of the 3D model, with initial tests and examples described in detail.

The first chapter begins with an introduction to the thesis and provides a review of the solar radio burst and coronal physics literature. This is followed by three research chapters and a final chapter summarising conclusions from the previous chapters, and outlining future work.

Chapter 2, the first research chapter, puts forward a new model for the radial electron density profile in the solar corona. This is an offset power law model, $n_e(r) \propto (r - r_0)^{-\alpha}$ with radial offset r_0 from the centre of the Sun and power law index γ. In stark contrast with several commonly used models, the model parameters all have a clear physical interpretation in terms of the bulk flow of the solar wind and the source of coronal plasma. We find that the model fits very well to many published density data sets obtained by white light and

Chapter 3 begins to discuss the quasilinear relaxation of electron beams and their production of Langmuir waves. In this chapter we undertake a detailed study of the 3D quasilinear equations, using Legendre expansion and the choice of reasonable yet analytically useful distributions. In the 1D picture the resonance is one-to-one such that waves with wavenumber k are only resonant with electrons with the particular speed v_ϕ. It is shown that in 3D a wave may be exited by any electron with $v > v_\phi$, which changes significantly the growth rate of Langmuir waves and therefore the conditions for a particular electron distribution to be unstable.

Chapter 4 introduces a numerical method which describes the system of electrons and Langmuir waves in a 3D axisymmetric way. The numerical scheme is discussed in detail before initial tests are presented. These include the stability of the thermal level of waves for Maxwellian electrons, a thorough exploration of isotropic gap distributions of electrons, and numerical simulation of P_1 distributions of the type discussed analytically in Chapter 3. Diffusion of particles is explored analytically and numerically, and it is shown that indeed particles diffuse significantly in pitch angle as well as in momentum. In order to consider more realistic electron distributions reminiscent of available data, and also to increase the complexity of the cases considered by the numerical code, the quasilinear evolution of distributions of the form $\cos^{2N+1}\alpha$ is developed. It is shown that these higher-order and more anisotropic distributions evolve in a different way than the standard 1D theory would suggest, due to the 3D resonance condition and associated pitch angle diffusion.

Chapter 5 summarises the conclusions of this thesis and outlines the significant future work for this numerical model and line of investigation. The numerical code has great potential for further development and application both to artificial and realistic in-situ electron distribution data.

Contents

Chapter 1

Introduction and Literature review

Not long after Maxwell formulated his equations and predicted the existence of radio waves, and immediately after Hertz discovered them experimentally in the late 1880s, scientists expected the Sun to be an active radio source. Thomas Edison and Oliver Lodge unsuccessfully attempted to find solar radio emission in the 1890s[*McLean and Labrum*, 1985], and it was not until the wartime development of metre-wavelength radar that a solar signal was detected. In February 1942 a strong, noise-like and highly variable radio source was picked up, at the same time as the largest ever recorded sunspot group appeared on the Sun. This result was published after the war [*Appleton*, 1945; *Appleton and Hey*, 1946] and a new research field was born.

Solar storms were observed in 1947 using the flat surface of the sea as a "Lloyd's Mirror" interferometer [*Wild and McCready*, 1950; *McLean and Labrum*, 1985], results which cemented the link between intense solar radio emission and sunspot activity. In the following decade, solar radio emission was found to be made up of a slowly varying "Quiet Sun" component and a set of radio bursts which vary in frequency on a much smaller timescale and were classified by the way their frequency varies with time. These solar bursts were associated temporally and spatially with solar energetic events like flares [*Benz*, 1993] and were seen to be obviously nonthermal in origin. Finally, solar radio sources were observed to travel through the corona at extremely fast speeds (about 0.3c).

The most common of the family of solar radio phenomena, Type III radio bursts, are associated with a fast stream of electrons through the corona and are emitted at a frequency that is related to the number density of electrons

in the background plasma (see 2 for more detail). Any study of the underlying physics behind such events must include a model for the density profile in the corona. As is discussed below, theories about both the electron-Langmuir wave interaction and subsequent Type III radio emission are sensitive to density variations. We therefore present evidence for a new, physically significant and empirically well-supported radial density model for the solar corona as part of our investigation of the electron-Langmuir wave interaction.

With these observational clues, *Ginzburg and Zheleznyakov* [1958] formulated a two step theory to describe radio emission from a solar plasma. In this picture, which still underlies the consensus theory of radio emission, an electron beam is excited by an impulsive process (e.g. a solar flare) and travels through the ambient plasma of the corona. The interaction between the beam and the background plasma leads to excitation of plasma, or Langmuir, waves. The beam and the waves are resonant with each other in a specific way, such that growing Langmuir waves have a back-reaction on the electron beam that excited them. The second step in the process involves the excited Langmuir waves undergoing nonlinear process (e.g. wave-wave interaction and scattering by ion acoustic waves) which produce radio waves at the plasma frequency or its second harmonic. Efforts have been made to improve upon the Ginzburg and Zhelezniakov model but the underlying two stage process remains the same.

The first stage in the process, the interaction between an electron beam and the population of Langmuir waves driven by the propagation of the beam through the background plasma, is described by a set of quasilinear equations. Consideration of the propagation of very fast, narrow electron beams directed along open magnetic field lines out from the Sun led to the use of a one-dimensional approximation to describe the particle evolution. That is, the electron beam was described as a 1D distribution in the velocity component parallel to the magnetic field, $v_\parallel$, with the other components neglected. These simplifying assumptions were necessary for the field to advance and the evolution of the coupled electron-Langmuir wave system to be described up to an asymptotic condition. Namely, the excited Langmuir waves were expected to draw energy from the electrons, cause them to diffuse in velocity, and form a quasi-stable plateau distribution whereupon the instability is exhausted. In this picture, electrons with a given speed $v_\parallel$ are only resonant with Langmuir waves with the wavenumber $k = \omega_p/v_\parallel$. The 1D analysis also leads to the condition for a given electron distribution $f(v = v_\parallel)$ to be unstable to the growth

of Langmuir waves: that $\partial f/\partial v > 0$.

This thesis challenges these long-held and deeply-ingrained results about electron-Langmuir wave resonance. Attempts at two and three-dimensional extensions of the analytic theory have hitherto still relied upon parts of this picture derived from the 1D analytic theory. We show that, in fact, a 3D axisymmetric consideration of the quasilinear equations challenges both one-to-one resonance between Langmuir wave and electron beams and plateau formation.

1.1 The Sun and the Solar corona

There are five distinct layers of the solar atmosphere, which are identified predominantly by the temperature as it varies from the surface of the Sun out to the interplanetary medium (IPM) [*Aschwanden*, 2004; *Dulk*, 1985]. The photosphere, chromosphere, and transition region are relatively thin layers ($< 0.005 R_S \approx 3000$ km) where the temperature varies from ≈ 6000 K at the photosphere up to $\approx 10^6$ K in the solar corona. The magnetic field of the Sun also changes dramatically over these regions. A twisted, complex and strong magnetic field network exists in the chromosphere, which fans out from concentrated bundles into a more uniform distribution in the corona.

The corona is a highly inhomogenous, dynamic environment which supports a variety of plasma structures. Active regions on the Sun lead to density inhomogeneities at low heights, which can be probed in soft X-rays as their brightness is proportional to the electron number density squared (n_e^2). There is a quiet corona component, as well as coronal hole structures [*Cranmer*, 2009] from which the fast solar wind originates.

Two longstanding problems concerning the solar corona are, first, how the corona is heated to $> 10^6$K and second, how the bulk outflow is driven to form the solar wind. Fig 1.1 shows a simulated temperature profile of the lower corona, implying that there must be strong heating mechanisms acting above the solar surface. While various heating mechanisms have been proposed in the century since this problem was identified, a conclusive and settled picture of the mechanism and site of coronal heating is still elusive. Further detailed

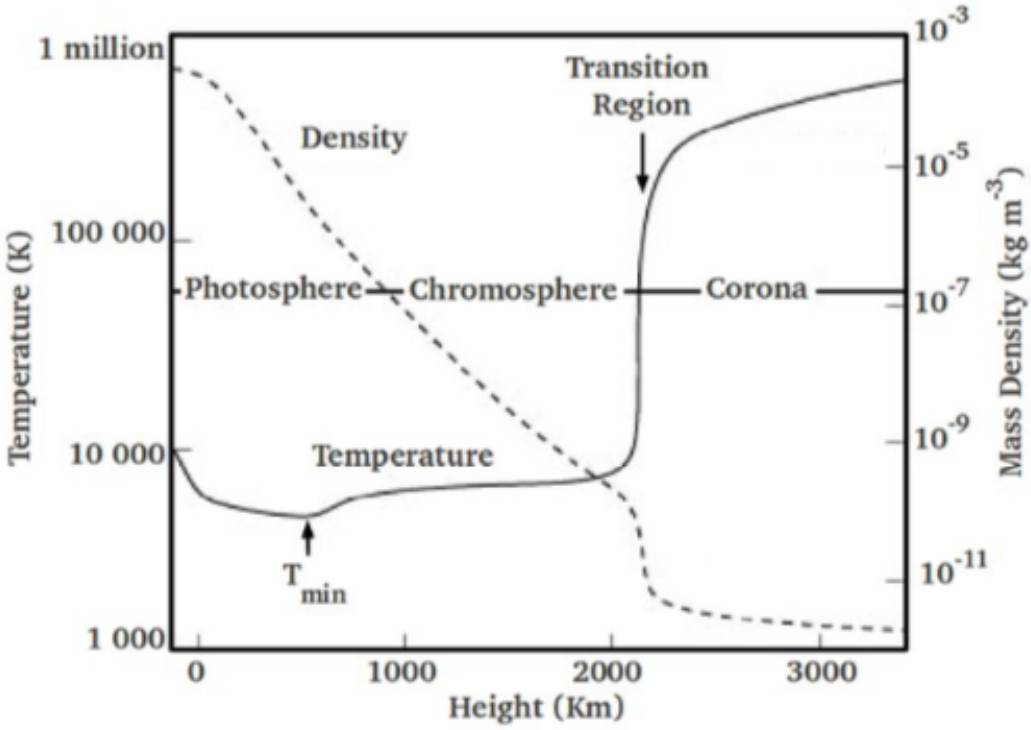

Figure 1.1: Mean temperature and density as a function of height above the photosphere, based on the VAL model [*Vernazza et al.*, 1973]. Image obtained from *Lang* [2001]

discussion of coronal heating can be found in *Klimchuk* [2006] and *De Moortel and Browning* [2015].The other problem, the acceleration of the solar wind, is discussed in Section 1.1.1.

1.1.1 The Solar Wind

The existence of gas outflows from the Sun with velocities ranging from 500 to 1500 km/s was first suggested by Biermann [1951] to explain observed motions of comet tails. The term *solar wind* was introduced by *Parker* [1958], who developed the first isothermal hydrodynamic theory for the supersonic solar wind. Parker also showed that the corona must be constantly streaming radially outwards with a flow velocity of $500 - 1000$ km/s, and solar rotation must, on a large scale, cause the Sun's magnetic field to form a spiral structure (the Parker spiral). Parker's prediction is shown in Figure 1.2. Deviations from the Parker solar wind, with acceleration and other mechanisms, have been

developed [*Usmanov et al.*, 2011; *Schulte in den Bäumen et al.*, 2012; *Tasnim and Cairns*, 2016; *Tasnim et al.*, 2018]. The solar wind is made up of two components: the fast wind, with a velocity around 800 km/s and the slow wind with a typical velocity of 400 km/s. The fast solar wind arises from open magnetic field lines, with almost all of it originating from coronal holes [*Cranmer*, 2009]. The slow solar wind originates from structures that have closed magnetic field lines.

Despite the developments in theoretical models of the solar wind (e.g. *Tasnim et al.* [2018] with an accelerating solar wind and nonradial components) and in observations closer to the Sun or at higher altitudes by the Helios [*Schutz and Karsten*, 1973] and Ulysses [*Wenzel et al.*, 1990] spacecraft respectively, the acceleration and origin of the solar wind remains a disputed question. Certain theories require acceleration to occur as far as $1R_S$ above the surface, for example ion-cyclotron heating of the corona [*Isenberg*, 2001] and acoustic wave breaking [*Stasiewicz*, 2006], whereas others occur close to or at the photosphere. These questions are particular timely as the impending first data and analysis of the NASA Parker Solar Probe [*Fox et al.*, 2016] promise to shed new light on the solar wind at low helioaltitudes, with ESA's Solar Orbiter [*Müller et al.*, 2013] to follow.

1.1.2 Density profiles

We have previously described a collection of complex structure in the low corona which leads to rapidly varying density fluctuations; however, observations of specific emission lines demonstrate that the structure fans out and becomes more indistinct with height. This corresponds to the spreading of the magnetic field out from concentrated bundles in the chromospheric network, and implies a more uniform distribution in the corona. It therefore makes sense to talk about a radial electron density profile $n_e(r)$, where n_e is the electron number density and r is the radial distance measured from the centre of the Sun.

Several density profile models have been proposed. A simple gas hydrodynamic argument leads to an exponential model $n_e(r) \propto \exp(B/r)$ with B a positive constant [*Newkirk*, 1961], conservation of electron number (assuming no acceleration) leads to a model with $n_e(r) \propto r^{-2}$, and there are also empirical models based on Taylor expansions of the Parker model (these models are discussed further in Chapter 2). Often, a density profile is a first order approximation used to advance theoretical or computational analysis, For example, the speed of the shock that excites Type II solar radio bursts can be calculated

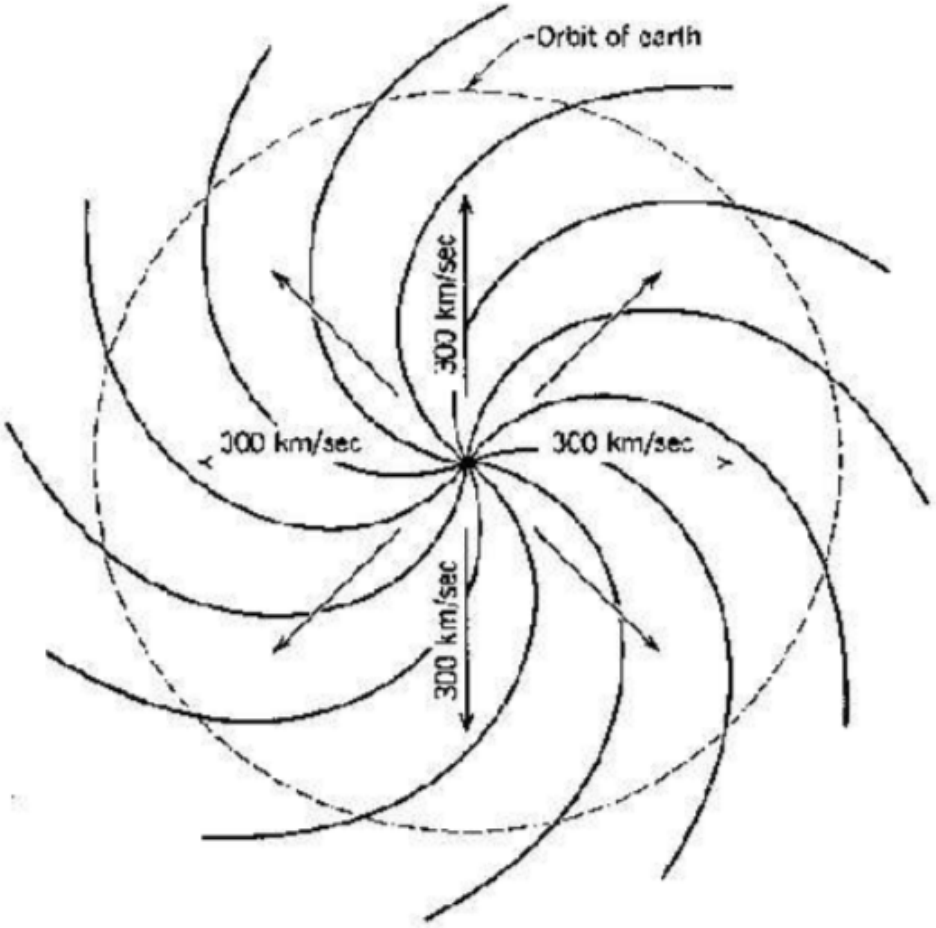

Figure 1.2: The Parker spiral: solar magnetic field lines in the equatorial plane, with the radial motion of the slow solar wind (arrows) shown as being constant at 300 km/s. [*Parker*, 1963]

using the Type II frequency drift rate and the coronal density profile. J.P. Wild in [*McLean and Labrum*, 1985] describes how a more accurate density profile revised the calculated speed by a factor of 2. Density profiles are also interesting in their own right. Coronal heating and acceleration leave signatures in the density profile, which will be discussed in greater depth in Chapter 2.

1.2 Plasmas and Langmuir waves

A plasma is characterised by a large degree of ionisation in its constituent atoms, which leads to collective effects over large distances and as such plasma can support a rich variety of wave phenomena. Plasmas are quasineutral, meaning for sufficiently large spatial scales there is no net separation of charge. This spatial scale is called the Debye wavelength λ_D, from which the Debye wavenumber $k_D = 2\pi/\lambda_D$ is defined. The Debye length is given by

$$\lambda_D = \sqrt{\frac{\epsilon_0 k_B T_e}{n_e e^2}}, \tag{1.1}$$

where T_e is the electron temperature, n_e the number density, and e is the charge on the electron.

The electrons and ions oscillate at frequencies given by the number density in unmagnetised plasmas. These plasma oscillations occur as electrons are displaced from the ions, and the resulting charge imbalance sets up electric fields that pull them back and re-establish quasineutrality. The electrons overshoot the ions, and an oscillation is maintained Electrons, being much lighter, can be considered to oscillate around fixed ions. The electron plasma frequency ω_p is

$$\omega_p = \sqrt{\frac{n_e e^2}{\epsilon_0 m_e}}. \tag{1.2}$$

Propagating versions (Tonks and Langmuir, 1929) of such oscillations are called Langmuir waves, and can travel through the plasma due to thermal effects. The dispersion relation for Langmuir waves is

$$\omega_L^2(k) = \omega_p^2 + \frac{3}{2} v_e^2 k^2 = \omega_p^2 \left(1 + \frac{3}{2}\frac{k^2}{k_D^2}\right), \tag{1.3}$$

where v_e is the thermal speed of electrons, related to the electron temperature T_e by $v_e = \sqrt{k_B T_e / m_e}$

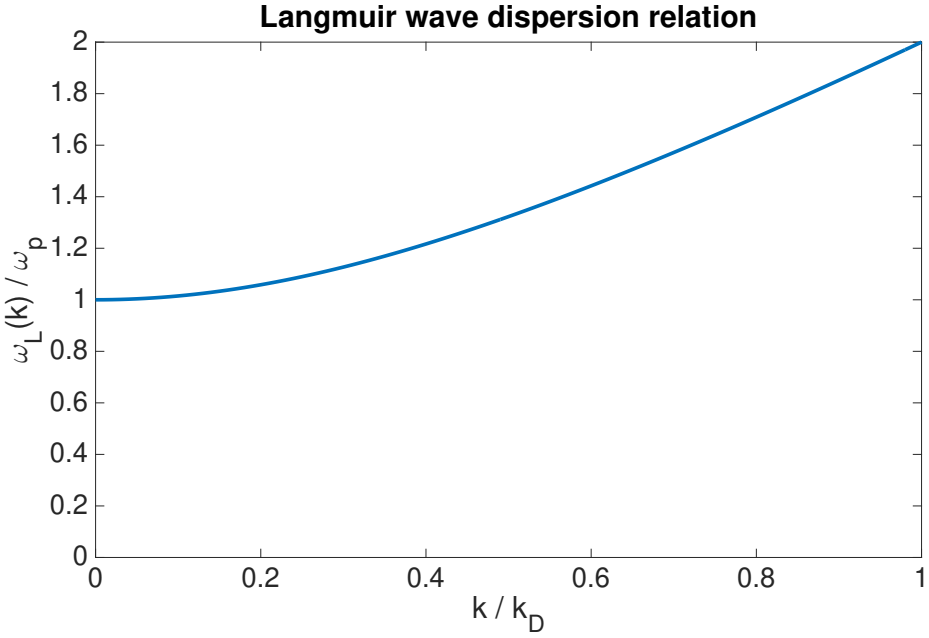

Figure 1.3: The dispersion relation for Langmuir waves. For most of the relevant parameter space, $\omega_L \approx \omega_p$; however, the difference is discussed in Chapter 4

Langmuir waves are most physically significant at $k < k_D$ as $v_e^2 k^2 \ll \omega_p^2$. Therefore, Langmuir waves can in most cases be considered to have $\omega \approx \omega_p$. The full dispersion relation is shown in Figure 1.3.

In the IPM, Langmuir waves have been observed to be very bursty and to be generated at large distances from the Sun - further than thought possible from electron beams, as will be made clear in section 1.5. Such Langmuir waves indicate the plasma environment between the Sun and Earth is highly inhomogeneous. Figure 1.4 shows bursty Langmuir waves measured at 31.1 kHz by the ISEE 3 spacecraft. Strong density fluctuations in the plasma can explain how a particle distribution that is unstable to Langmuir waves can persist and why the wave growth is bursty [*Robinson et al.*, 1992].

1.3 Plasma emission

A hot plasma may emit radiation coherently or incoherently. Incoherent emission is the result of individual particles shedding energy in an unorganised way, for example by bremsstrahlung. When radio signals were first detected

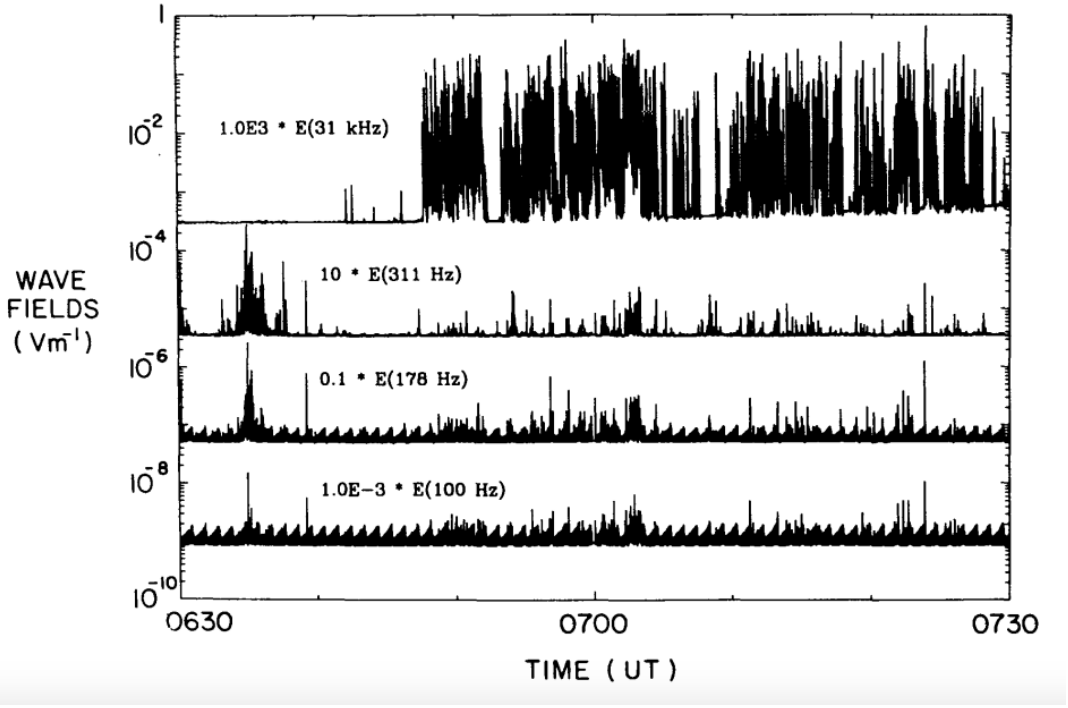

Figure 1.4: Bursty Langmuir waves seen in the 31.1 kHz channel of the International Sun-Earth Explorer-3 (ISEE-3) instrument, at the L-1 Lagrangian point [*Cairns and Robinson*, 1995].

from the Sun, the natural explanation was that they were produced by incoherent processes. However, as summarised by *Melrose* [1970], various features of transient solar radio bursts could not be explained by incoherent emission. Rather, a coherent process had to be involved. This means that electrons convert kinetic energy to electromagnetic energy via a more efficient and organised process, such as through plasma instabilities that drive the growth of specific wave modes. The main way to observationally distinguish coherent emission from incoherent emission is via a suitably high brightness temperature (T_b) - incoherent emission processes have upper limits on T_b. T_b is the theoretical temperature a black body would have to emit radio waves at the measured frequency and intensity.

In this thesis we are concerned primarily with the particular coherent emission mechanism called "plasma emission". Plasma emission results in radio waves near ω_p or $2\omega_p$. It is the mechanism that is most widely accepted for

Type III solar radio bursts and for some other types of bursts.

Figure 1.5 gives an overview of the stages of the plasma emission process. It assumes the existence of an electron beam, and we note that, as D.J. McLean puts it, the theory of Type IIIs is insensitive to the mechanism of electron beam acceleration [*McLean and Labrum*, 1985]. However, the characteristics of the beam are important, so electron beams will be discussed in further detail in Section 1.5. For the purposes of discussing the emission process however, it is sufficient to say that we have a stream of faster electrons moving through a background thermal plasma.

This fast population of electrons then loses energy and drives Langmuir waves via a streaming instability. The fast electrons are in resonance with Langmuir waves, the nature of which is a major topic of this thesis, particularly Chapters 3 and 4. The Langmuir waves driven by the electron beam (described as 'Langmuir turbulence' in Figure 1.5) then undergo nonlinear processes; scattering by ion acoustic waves can directly produce radio waves at the fundamental frequency f_p, while coalescence of two Langmuir waves produces radio waves at the second harmonic $2f_p$.

1.4 Solar Radio bursts

As we introduced earlier, a set of solar radio phenomena with short time scales and with brightness temperatures above the solar background level is supported by different mechanisms in the Sun-Earth system. Fig 1.6 is a schematic of a dynamic radio spectrum with common solar radio bursts and other emission. Types I, II, and III were discovered first and classified according to their frequency drift rate, df/dt [*Wild and McCready*, 1950]. As shown in Fig 1.6, Type I has the slowest drift and Type III the fastest (a steep, almost straight line on the spectrum). Types I, II, III and IV emission are expected to be caused by plasma emission, although the excitation process of Type I bursts is still an unsettled question. Type IV emission has been attributed to both plasma emission and to gyrosynchotron emission [*Dulk*, 1985].

While we do not discuss radio emission directly in this thesis, Type III solar radio bursts are both a major motivation and observational tool for striving to understand both electron density profiles and the electron-Langmuir wave interaction.

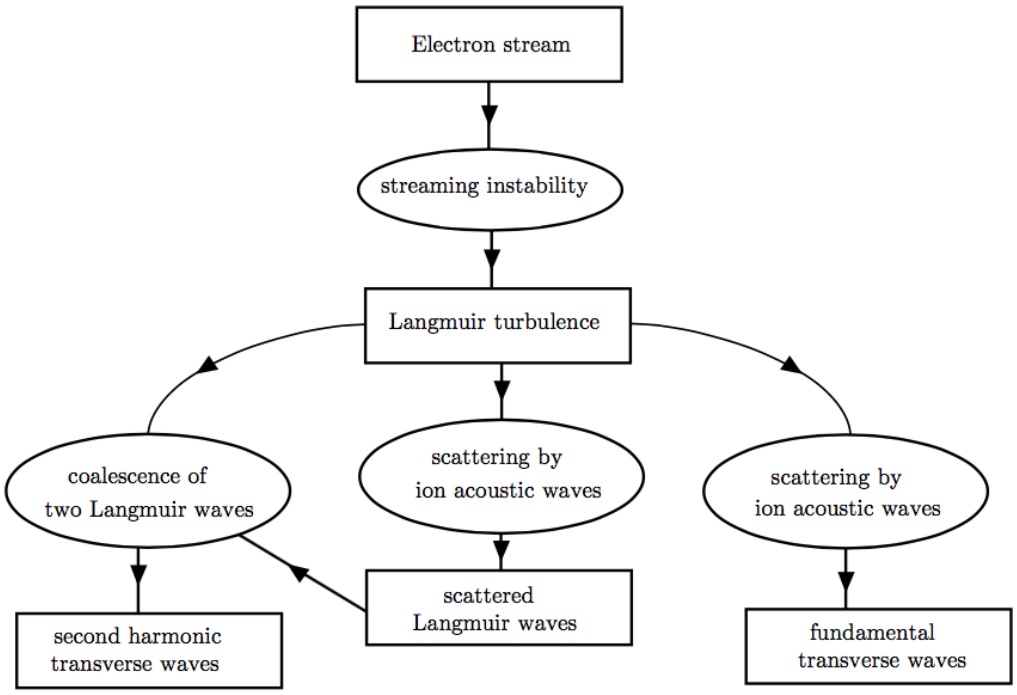

Figure 1.5: From *Melrose* [2009], the primary processes considered relevant in the theory of plasma emission.

1.4.1 Type III solar radio bursts

Type III radio bursts are frequent and intense transient radio phenomena, and as such are one of the most closely studied. Their tell-tale frequency drift was the first clue to their exciting mechanism: its curvature ruled out a theory by *Jaeger and Westfold* [1949] that the bursts' source was at a fixed height in the corona. *Wild* [1950] concluded that, like Type IIs, Type III bursts are excited by a travelling disturbance moving out though the corona, emitting radiation at the plasma frequency which decreases according to $f(p) \propto \sqrt{n_e}$. This interpretation implies very high speeds for the Type III exciter - on the order of $0.1c$, which was a speed unobserved and unexpected at that time in the solar corona. Example Type III dynamic spectra are shown in Figure 1.7.

With this interpretation, which as we have said in section 1.3, is up to this point not dependent on the acceleration mechanism of the 'disturbance', the plasma emission hypothesis for Type III solar radio bursts is an interesting theoretical problem because, as first outlined in *Sturrock* [1964], using the standard accepted theoretical framework, the two-stream instability should sat-

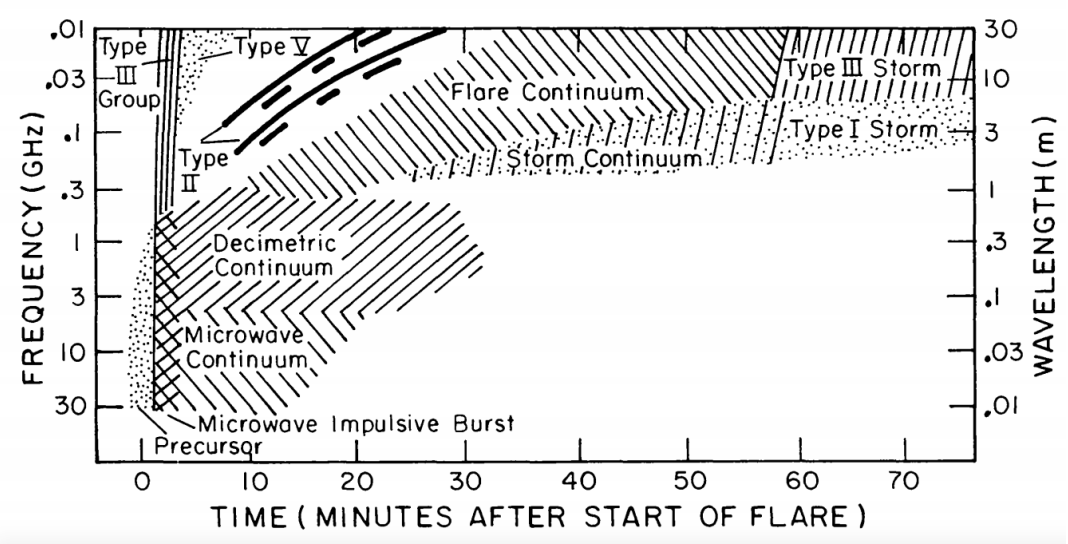

Figure 1.6: Schematic of a dynamic spectrum featuring idealised examples of solar radio burst types, showing the frequency domains, frequency drift rates and harmonic structure (for Type IIs specifically). From *Dulk* [1985]

urate extremely quickly, and electron beams should not propagate out of the lower corona. We will explore this issue more in Section 1.5

Type IIIs are not only a common unexplained radio phenomenon but are also useful tool in understanding the solar corona. As Type IIIs are released at the plasma frequency or its second harmonic, they can act as probes of the density and temperature [*McCauley et al.*, 2018], and their signature of electron beams leaves clues about energetic solar events [*Wild et al.*, 1963].

Reviews of Type III radio burst observations and theory can be found in *Reid and Ratcliffe* [2014], *Goldman* [1983], as well as plasma emission-focused reviews by *Robinson and Cairns* [2000] and *Melrose* [1990]. Numerical simulations of Type III dynamic spectra have been developed [*Li et al.*, 2008; *Li and Cairns*, 2013; *Li and Cairns*, 2014], using a pseudo-1D model of the streaming instability and electron beam-Langmuir wave resonance. As electron beams and Langmuir wave distributions are difficult to observe in situ, such simulations are useful to test theories of the underlying emission mechanism for Type IIIs, as well as models of the radio wave propagation out through the solar corona and into the IPM. Representative interplanetary Type III data is shown in Figure 1.8.

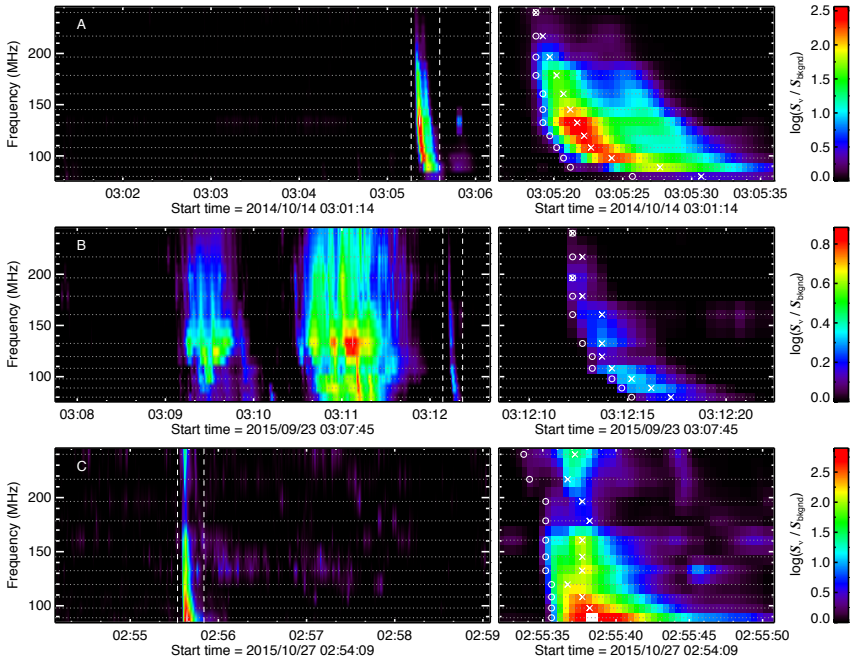

Figure 1.7: Type III radio bursts imaged with the Murchison Widefield Array (MWA) in Western Australia. Image produced by *McCauley et al.* [2018]

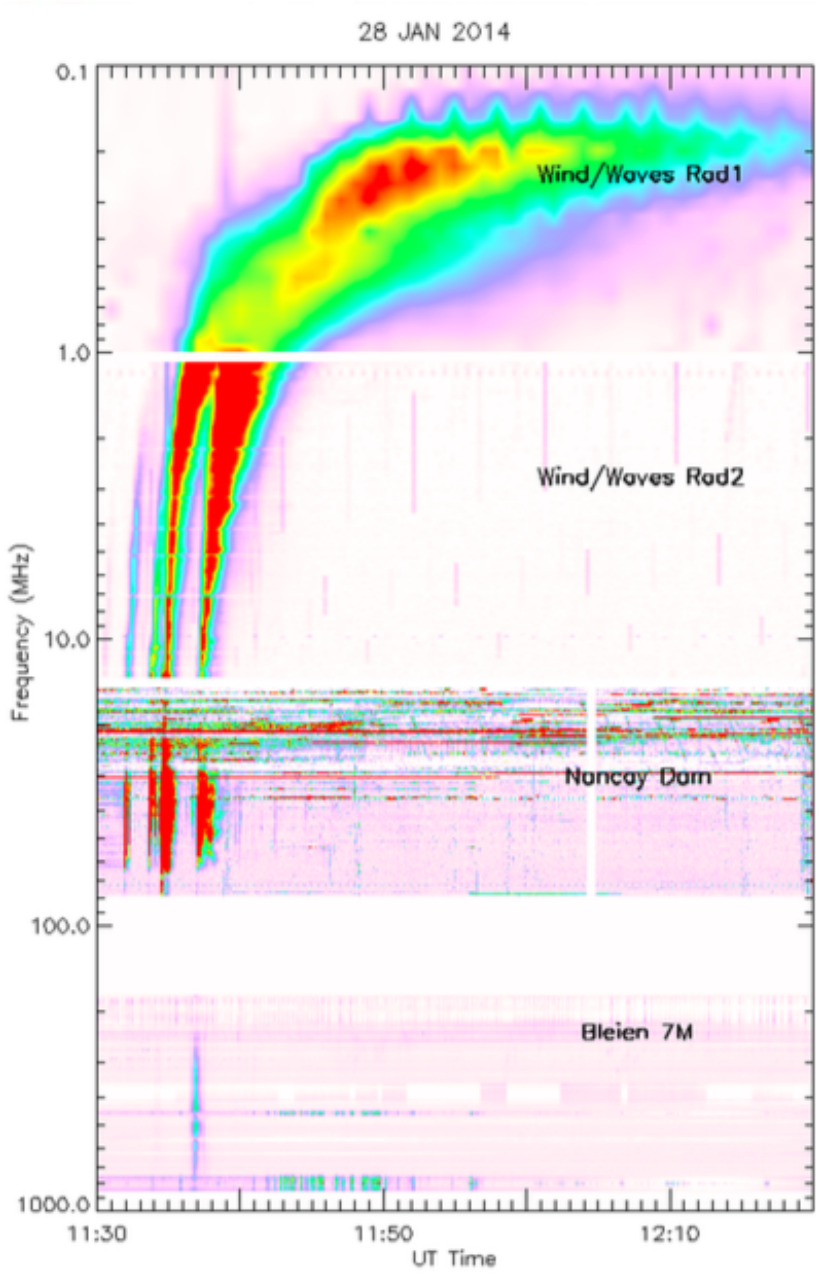

Figure 1.8: Multiple interplanetary type III bursts drifting from 1GHz down to < 1 MHz, observed using different instruments covering different frequency ranges[*Reid and Ratcliffe*, 2014].

1.5 Electron beams in theory and observation

Electron beams are excited by energetic events on the Sun such as flares [*Benz*, 1993], and much theoretical work has been devoted to explaining how this is possible, since as *Alfvén* [1939] pointed out, beams can be considered electric currents, which need a closed path in order to propagate. *Melrose* [1990] lays out the argument that either a return current must be set up or the external magnetic field strength is large enough to overcome the self-field of the beam. These arguments give a limit on the current leaving the Sun, $I \lesssim 10^{12}$ A, which is important in considering solar flare models. The formation of return currents is an open research field - for example, a comparison between observations and theory in solar flare loops was done by [*Battaglia, M. and Benz, A. O.*, 2008]. Both radio evidence and direct in-situ observation has led to significant advances in electron acceleration theory. Some of this radio evidence involves the solar radio bursts discussed in Section 1.4, and given the focus of this thesis we will focus on the beams associated with Type III bursts. A brief overview of the theory and observation of solar flares is nevertheless desirable.

1.5.1 Solar flares

Solar flares vary widely, and even in a particular flare there are many complex processes happening simultaneously. *Smerd et al.* [1975] identifies 6 different acceleration mechanisms, and the question of which mechanism excites particles for a given type of radiation is generally still disputed. Nevertheless it is accepted that the first phase of a solar flare, where there is bulk energisation of particles, is the phase that excites beams that produce Type IIIs. Such beams are made up of energetic electrons with $E > 10$ keV, [*Ramaty et al.*, 1980]. *Melrose and Dulk* [1987] summarises radio evidence for this conclusion, and [*Lin et al.*, 1981] provides in-situ evidence. Even more energetic and relativistic electrons with energies from 20 keV - 20 MeV have been found [*Lin et al.*, 1982] and have been associated with a secondary stage in the flare. In such a stage, electrons which have already gone through bulk energisation undergo rapid Fermi acceleration [*Bai et al.*, 1983; *Melrose*, 1983].

Magnetic reonnection is widely believed to be the driver of solar flares, and indeed most solar impulsive events. Alternate theories exist but are beyond the scope of this review. The CSHKP flare model [*Carmichael*, 1964; *Stur-*

rock, 1966; *Hirayama*, 1974; *Kopp and Pneuman*, 1976] is also known as tge 'standard model' of solar flare excitation. A simplified schematic from *Lang* [2006] is shown in Figure 1.9; in short, magnetic reconnection occurs high in the corona above a cusp loop magnetic structure. Electrons are excited both toward the Sun and outward - the particles that hit the chromosphere produce hard X-rays and gamma rays, as well as heating the chromospheric material. This material expands into the loop and releases intense EUV, soft X-rays and microwave radiation. Most importantly for the work of this thesis, electron beams are excited above the reconnection point, and plasma above the cusp can also be accelerated away from the Sun in Coronal Mass Ejections (CMEs).

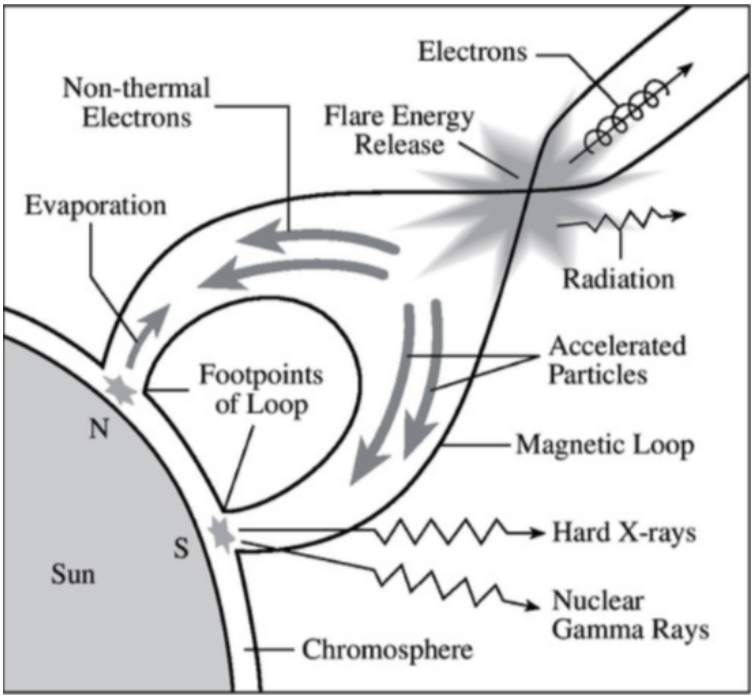

Figure 1.9: CSHKP flare model schematic, from *Lang* [2006]

This model explains several observed features of solar flares - energy coming from two distinct heights above the solar surface and hard X-ray production in more intense flares, for example. The most significant recent observing mission that gathered data on these effects was the Reuven Ramaty High Energy Solar Spectroscopic Imager (RHESSI) [*Lin et al.*, 2002]. In its 16 years of operation from 2002-2018 RHESSI provided fundamental insight into solar flares by observing the Sun in hard X-ray and gamma-ray wavelengths. The many flare

observations have and continue to support investigations into particle accelerations in solar flares - some of which are discussed in *Zharkova et al.* [2011] - including the fact that a significant proportion of the flare energy goes into particle acceleration.

1.5.2 Electron beam stability

From interplanetary Type III bursts and direct measurement of beams at 1AU, it is well known that electron beams can be stable enough to persist out of the low corona and out into interplanetary space. Figure 1.10 shows 2-dimensional electron beam data as well as reduced 1D distributions done in *Ergun et al.* [1998] - emphasising the reliance on the 1D $\partial f/\partial v$ analysis. As explained in more detail in Section 1.6, this presented a theoretical problem called Sturrock's Dilemma [*Sturrock*, 1964], because fast electron beams should be unstable to the growth of Langmuir waves, drawing energy from the beam and leaving it as a plateau distribution. Up to the present, competing explanations for the seemingly mutually exclusive existence of Type III bursts and stable electron beams have been developed. *Muschietti* [1990], *Robinson* [1993], *Robinson and Cairns* [2000], *Melrose* [2009] and *Reid and Ratcliffe* [2014] review these theories and note that, drawing from them, Sturrock's Dilemma can be resolved. However, due to plasma emission being 'insensitive' to the beam mechanics, it is difficult to identify with confidence which mechanism is operating in a given radio event. In Section 1.6, several theories that explain the stability of interplanetary beams are outlined.

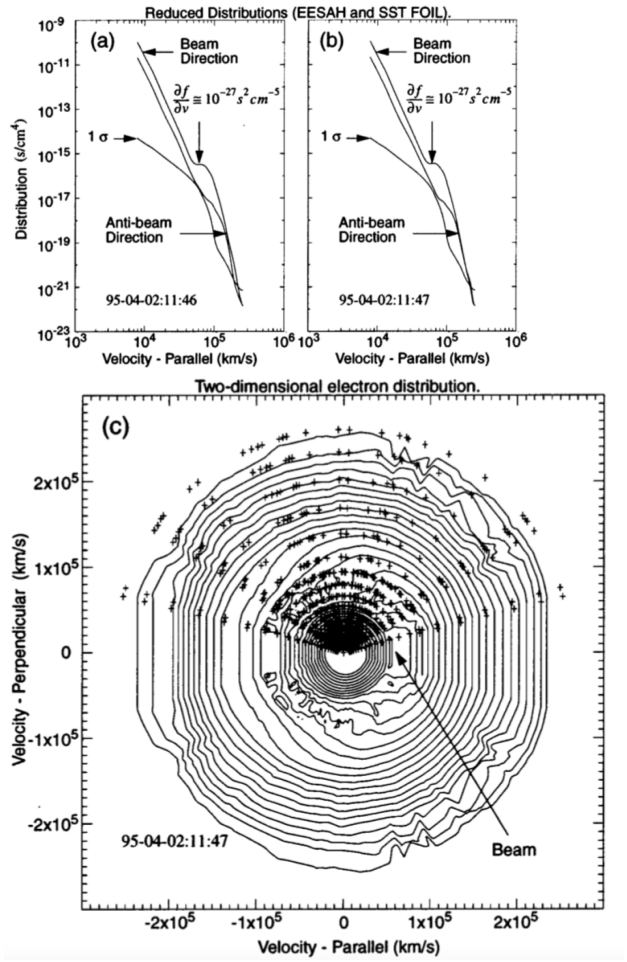

Figure 1.10: a,b) Reduced 1D distributions made from data in c), showing the reliance on 1D $\partial f/\partial v$ analysis for stability of electron distribution c) two dimensional electron distribution from *Ergun et al.* [1998]

1.6 Electron-Langmuir wave interaction

1.6.1 Quasilinear equations

The quasilinear (QL) equations describe the interaction between the Langmuir waves and the electron beam in the weak field approximation. Let $N_L(\mathbf{k})$ be the Langmuir wave occupation number, defined as the number of wave quanta per unit volume in $k-$space, and the classical electron distribution function by $f(\mathbf{p})$, normalised such that $\int d^3\mathbf{p}\ f(\mathbf{p}) = n_e$, where n_e is the number density of electrons. The ratio of electric energy to total energy for

Langmuir waves is denoted by $R_L(\mathbf{k})$ and the polarisation vector for Langmuir waves by $\mathbf{e}_L(\mathbf{k})$. Using these quantities, the probability per unit time that a particle with momentum $\mathbf{p}$ emits a Langmuir wave quantum in the range $d^3\mathbf{k}/(2\pi)^3$ is

$$w_L(\mathbf{k},\mathbf{p}) = \frac{2\pi e^2 R_L(\mathbf{k})}{\epsilon_0 \hbar |\omega_L(\mathbf{k})|} |\mathbf{e}_L(\mathbf{k}) \cdot \mathbf{v}|^2 \delta\big(\omega_L(\mathbf{k}) - \mathbf{k}\cdot\mathbf{v}\big). \tag{1.4}$$

Einstein showed that emission can be stimulated by the presence of existing emitted waves, and the rate of stimulated emission is given by $w_L(\mathbf{k},\mathbf{p})N_L(\mathbf{k})$. The total emission probability is therefore $w_L(\mathbf{k},\mathbf{p})\big(1+N_L(\mathbf{k})\big)$. Continuing with the single particle consideration, if the particle emits a Langmuir wave then the momentum of the particle decreases from $\mathbf{p}$ to $\mathbf{p}-\hbar\mathbf{k}$. The absorption probability is given by $w_L(\mathbf{k},\mathbf{p})N_L(\mathbf{k})$. Conversely, when an electron absorbs a Langmuir wave quantum its momentum changes from $p-\hbar\mathbf{k}$ to $\mathbf{p}$.

Now consider the full particle distribution $f(\mathbf{p})$. The rate of emission by particles undergoing the transition $\mathbf{p} \to \mathbf{p}-\hbar\mathbf{k}$ is given by $w_L(\mathbf{k},\mathbf{p})\big(1+N_L(\mathbf{k})\big)f(\mathbf{p})$. The total rate of emission per unit volume is then given by integrating over $\mathbf{p}$:

$$w_{em} = \int d^3\mathbf{p}\; w_L(\mathbf{k},\mathbf{p})\big(1+N_L(\mathbf{k})\big)f(\mathbf{p}). \tag{1.5}$$

Similarly, the rate of absorption by particles undergoing the transition $\mathbf{p}-\hbar\mathbf{k} \to \mathbf{p}$ is given by
$w_L(\mathbf{k},\mathbf{p})N_L(\mathbf{k})f(\mathbf{p}-\hbar\mathbf{k})$, and the total rate of absorption per unit volume is

$$\omega_{abs} = \int d^3\mathbf{p}\; w_L(\mathbf{k},\mathbf{p})N_L(\mathbf{k})f(\mathbf{p}-\hbar\mathbf{k}). \tag{1.6}$$

Finally, this allows us to write down the equation governing the changes to $N_L(\mathbf{k})$:

$$\frac{dN_L(\mathbf{k})}{dt} = \int d^3\mathbf{p}\; w_L(\mathbf{k},\mathbf{p})\Big[\big\{1+N_L(\mathbf{k})\big\}f(\mathbf{p}) - N_L(\mathbf{k})f(\mathbf{p}-\hbar\mathbf{k})\Big] \tag{1.7}$$

Here, we take the first order expansion $f(\mathbf{p}-\hbar\mathbf{k}) = f(\mathbf{p}) - \hbar\mathbf{k}\cdot\partial f(\mathbf{p})/\partial\mathbf{p}$. With this approximation (1.7) becomes

$$\frac{dN_L(\mathbf{k})}{dt} = \alpha_L(\mathbf{k}) - \gamma_L(\mathbf{k})N_L(\mathbf{k}), \tag{1.8}$$

where

$$\alpha_L(\mathbf{k}) = \int d^3\mathbf{p}\; w_L(\mathbf{k},\mathbf{p}) f(\mathbf{p}), \tag{1.9}$$

$$\gamma_L(\mathbf{k}) = -\int d^3\mathbf{p}\; w_L(\mathbf{k},\mathbf{p}) \hbar\mathbf{k} \cdot \frac{\partial f}{\partial \mathbf{p}}. \tag{1.10}$$

Here α_L and γ_L describe spontaneous emission and damping of Langmuir waves respectively.

The second QL equation describes the back reaction of the Langmuir waves on the particle distribution. The rate of change of $f(\mathbf{p})$ increases by the emission of waves associated with the transition $\mathbf{p} + \hbar\mathbf{k} \rightarrow \mathbf{p}$ and absorption, where $\mathbf{p} - \hbar\mathbf{k} \rightarrow \mathbf{p}$. The rate of change decreases by the corresponding reverse processes. The particle distribution $f(\mathbf{p} \pm \hbar\mathbf{k})$ is Taylor expanded to second order, whereupon the particle equation is found to evolve according to

$$\frac{df(\mathbf{p})}{dt} = \frac{\partial}{\partial p_i}[A(\mathbf{p})_i f(\mathbf{p})] + \frac{\partial}{\partial p_i}\left[D_{ij}(\mathbf{p})\frac{\partial f(\mathbf{p})}{\partial p_j}\right], \tag{1.11}$$

where

$$A(\mathbf{p})_i = \int \frac{d\mathbf{k}}{(2\pi)^3}\; w_M(\mathbf{k},\mathbf{p})\hbar k_i, \tag{1.12}$$

$$D_{ij}(\mathbf{p}) = \int \frac{d\mathbf{k}}{(2\pi)^3} w_M(\mathbf{k},\mathbf{p})\hbar^2 k_i k_j N_M(\mathbf{k}). \tag{1.13}$$

Here, $\mathbf{A}_i(\mathbf{p})$ describes the effect of spontaneous emission on electrons and $D_{ij}(\mathbf{p})$ desribes diffusion in momentum space.

1.6.2 1D theory

Assuming a 1D model and non-relativistic speeds, using the notation from *Melrose* [1986] and the plasma frequence definition Eq 1.2

$$\frac{\partial N(k)}{\partial t} + v_g \frac{\partial N(k)}{\partial x} = \alpha(k) - \gamma(k)N(k), \tag{1.14}$$

$$\frac{\partial f(v)}{\partial t} + v\frac{\partial f(v)}{\partial x} = \frac{\partial}{\partial v}\big[A(v)f(v)\big] + \frac{\partial}{\partial v}\left[D(v)\frac{\partial f(v)}{\partial v}\right], \tag{1.15}$$

where

$$v_g = 3\frac{v_e^2}{v}, \tag{1.16}$$

$$\alpha(k) = \frac{e^2}{4\epsilon_0 \hbar}\frac{v^3}{\omega_p^2}(k_D^2 - k^2)f(v)\Big|_{v=\omega/k}, \tag{1.17}$$

$$\gamma(k) = -\frac{\pi e^2}{m_e \epsilon_0}\frac{kv^3}{\omega_p^2}\frac{\partial f(v)}{\partial v}\Big|_{v=\omega/k}, \tag{1.18}$$

$$A(v) = \frac{e^2}{8\pi m_e \epsilon_0}\frac{(kv)^2}{\omega_p^2}(k_D^2 - k^2)\Big|_{k=\omega/v}, \tag{1.19}$$

$$D(v) = \frac{e^2\hbar}{2m^2\epsilon_0}\frac{k^3 v^2}{\omega_p^2}N(k)\Big|_{k=\omega/v}. \tag{1.20}$$

Features of the 1D theory evident in these equations include the condition for wave growth, which can be seen in the term given by Eq 1.18. Whether waves grow or are damped at a given wavenumber k depends on the sign of $\partial f/\partial v$, at and only at the resonant velocity $v = \omega/k$. Diffusion of the waves is, by hypothesis, only in one dimension.

Solutions to the 1D quasilinear equation have been found. The electron distribution function evolve towards a plateau distribution, e.g *Grognard* [1975, 1982]; *Li et al.* [2008]. The effect of the coupled interaction is shown in Fig 1.11. The formation of the plateau distribution and the exhaustion of the instability lead to a major contradiction early in the development of the quasilinear theory of the electron-Langmuir wave interaction. *Sturrock* [1964] showed that if the instability occurs unimpeded in plasma conditions such as are found in the lower corona, the beam should lose energy almost immediately. And yet, Type III exciter beams persist out to the interplanetary medium and are still unstable to Langmuir wave growth. Sturrock's dilemma led to the development of a number of theoretical explanations, one of which is Stochastic Growth Theory [*Robinson et al.*, 1993a; *Cairns and Robinson*, 1998] in which density fluctuations suppress the instability. Other theories involved waves emitted by the electrons at the front of the beam spatially could be reabsorbed by those behind [*Ryutov and Sagdeev*, 1970; *Zaitsev et al.*, 1972; *Mel'Nik et al.*, 1999]. We outline the most important of these theories below.

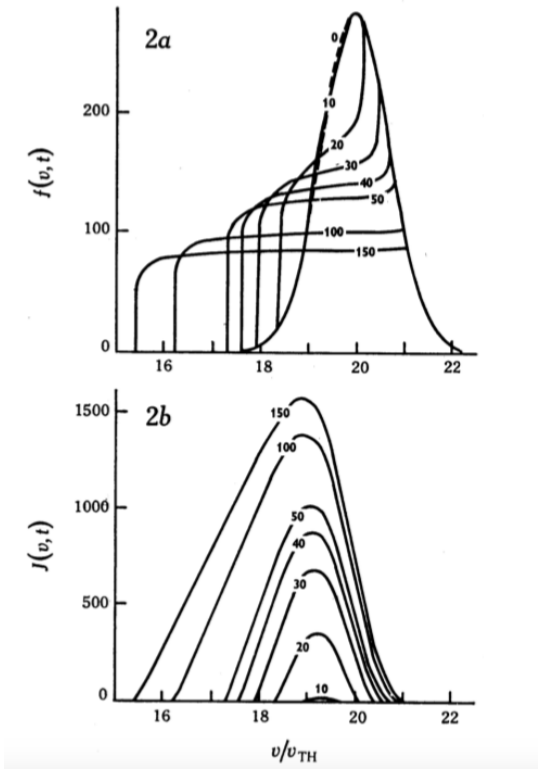

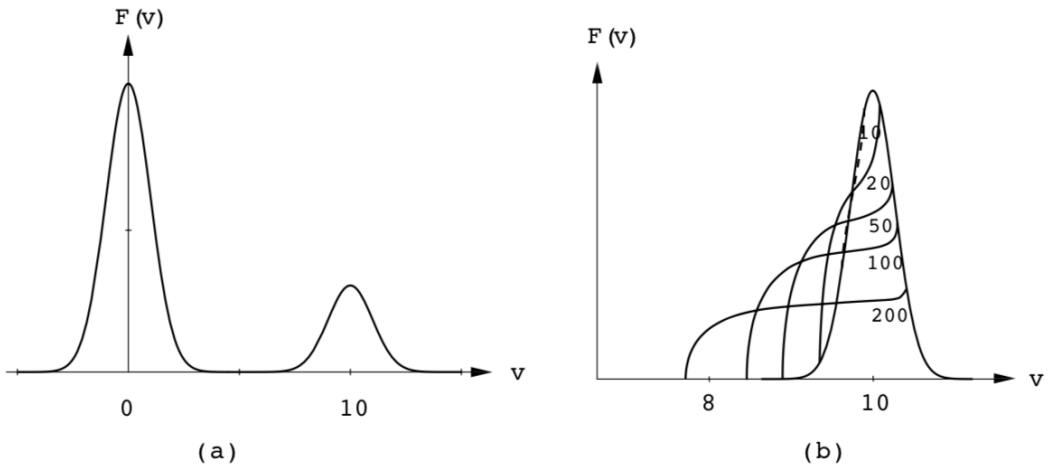

Figure 1.11: Plateau formation in the 1D quasinilear relaxation theory, with the numbers indicating timesteps. With increasing time, the particle distribution (left) forms a plateau distribution and the waves (right) grow with the peak shifting to lower phase speed. The left, from *Grognard* [1975]; right, from *Grognard* [1985].

1.6.3 Time-of-flight and re-absorption models

The Sturrock Dilemma [*Sturrock*, 1964] does not take into account a very simple idea that is important in beam dynamics: as a distribution of particles moves through space, the faster particles arrive at a given position earlier than slower ones. Even if one has a plateau distribution at one point in space, at a greater distance the fast particles arrive first meaning that the beam has essentially re-formed. This advection affect was explored with a numerical model by *Grognard* [1982, 1984] who found that the quasilinear relaxation and advection effects could balance each other and the beam persists.

Utilising this advection effect, a mechanism that has been proposed is that the beam distribution function propagates in a form that allows the Langmuir waves generated by electrons at the front of the beam are re-absorbed by electrons at the back. This means that the energy going into the Langmuir waves is recirculated amongst the electrons rather than being lost entirely to the beam. *Ryutov and Sagdeev* [1970] put forward an idealised model of this effect which was then employed by *Zaitsev et al.* [1972] in their treatment of the Type III problem. Numerical modelling based on this mechanism was developed [*Takakura and Shibahashi*, 1976; *Magelssen and Smith*, 1977] and extended by *Kontar et al.* [1998]; *Mel'Nik et al.* [1999], who showed the beam propagating as a "beam plasma structure"

However, as described in *Melrose* [1990] and *Mel'Nik et al.* [1999], while this theory allows inhomogenous distributions on a global scale, it relies on the wave distribution being locally homogenous. Observations indicate that the Langmuir waves involved in Type III events are in fact highly inhomogeneous (Figure 1.4). These are described further in Section 1.6.4. The

1.6.4 Stochastic Growth Theory

Observed Langmuir waves are strongly inhomogeneous, being observed to appear in intense isolated clumps [*Gurnett and Anderson*, 1976, 1977; *Gurnett*, 1978; *Lin et al.*, 1981]. Earlier quasilinear theory relied on the wave distribution being locally homogeneous; however, *Melrose and Cramer* [1989] showed that this condition could be relaxed. Clumpy distributions of Langmuir waves can undergo quasilinear relaxation under plausible conditions, and the energy density equal to the average energy density of the clumps. Stochastic growth theory

(SGT) argues that the beams driving interplanetary Type IIIs are marginally stable [*Robinson et al.*, 1992, 1993b], which relies on a similar argument to *Grognard* [1984], where the beam is re-formed due to time-of-flight effects. There is a balance between QL relaxation and advection, with a small positive growth rate for Langmuir waves that balances wave losses to damping and EM emission. Density fluctuations then perturb the marginally stable beam such that Langmuir waves grow randomly, and when local wave levels reach the threshhold for electrostatic decay there is a burst of product waves via the 3 wave interaction [*Robinson et al.*, 1993b, 1994]. *Robinson and Cairns* [1993] elaborates on the predicted emissivities of the radio wave products of this theory and compares them favourably with spacecraft data. *Cairns and Robinson* [1998] examines the constraints on modulational instabilities compared to SGT and shows that Langmuir waves driven by beams with realistic coronal parameters have wavenumbers too high for modulational instability, whereas SGT is reasonable at all heliocentric distances under almost all circumstances.

1.6.5 Modulational instabilities

Modulational instabilities apply in the context of strong Langmuir turbulence; if the energy density due to the Langmuir waves is W_L then the generally accepted condition for weak turbulence theory to apply is [*Melrose*, 1986]

$$\frac{W_L}{n_e T_e} \lesssim 10^{-4}, \tag{1.21}$$

otherwise strong turbulence effects must be taken into account.

Strong turbulence theory is based on the Zakharov equations [*Zakharov and Shabat*, 1972] which describe the envelope of the Langmuir waves and the density fluctuations of the electrons. Modulational instabilities involve the ponderomotive force driving Langmuir turbulence to higher wavenumbers *Nishikawa* [1968]. The instability proceeds as follows [*Muschietti*, 1990; *Melrose*, 1986]:

The ponderomotive force at the spatial position of the wave packet causes a local reduction in electron density, which focuses the Langmuir waves by refraction. In this way, an initially uniform envelope of Langmuir wave turbulence breaks up into envelopes with smaller natural lengths. These sites of enhanced turbulence have an even stronger associated ponderomotive force, and so the process is unstable. In Langmuir wave collapse, this process proceeds until

the envelopes are only a few Debye lengths across and then the energy can be extracted by the background electrons [*Pelletier*, 1982].

This has been applied to the Type III problem [*Papadopoulos et al.*, 1974; *Zakharov et al.*, 1985], most significantly as a way to limit the growth of resonant Langmuir waves and preserve the beam. The theory also includes direct emission of harmonic ($2f_p$) radiation by nonlinear currents produced by Langmuir wave collapse. Certain modern observations, such as intense and short-lived Langmuir wave peaks observed in-situ, have been interpreted as evidence of modulational instability and collapse [*Thejappa et al.*, 1993, 2013]. However, *Cairns and Robinson* [1998]; *Graham et al.* [2012a,b] and others have laid down a set of serious obstacles to modulational instabilities proceeding in any Type III context which have yet to be answered convincingly.

1.6.6 3D Axisymmetric models

A 3D distribution that is expressed in spherical polar coordinates can be expanded in spherical harmonics $Y_{\ell m}$. If we write the electron and Langmuir wave distributions in spherical polar coordinates, i.e. $f(\mathbf{p}, \mathbf{x}, t) = f(p, \alpha, \phi_p, \mathbf{x}, t)$ and $N(\mathbf{k}, \mathbf{x}, t) = N(k, \theta, \phi_k, \mathbf{x}, t)$ then axisymmetry implies

$$\begin{aligned} f(\mathbf{p}) &= f(p, \alpha), \\ N(\mathbf{k}) &= N(k, \theta), \end{aligned} \tag{1.22}$$

In this case, the spherical harmonics reduce to a simpler form - the Legendre polynomials P_ℓ. Legendre polynomials are a complete set of orthogonal polynomials and the wave and particle distributions can therefore be formally expanded such that

$$\begin{aligned} f(p, \alpha) &= \sum_{\ell=0}^{\infty} f_\ell(p) P_\ell(\cos\alpha), \\ N(k, \theta) &= \sum_{\ell=0}^{\infty} N_\ell(k) P_\ell(\cos\theta). \end{aligned} \tag{1.23}$$

The Legendre polynomials are given explicitly by the Rodrigues formula

$$P_l(x) = \frac{1}{2^\ell \ell!} \frac{d^\ell}{dx^\ell} \left[(x^2 - 1)^\ell \right]. \tag{1.24}$$

This expansion separates the magnitude (p, k) and angular (α, θ) dependencies of the particle/wave distributions, and so will transform the quasilinear

equations with two degrees of freedom into a set of partial differential equations with one degree of freedom. This complete expansion was performed explicitly by *Melrose and Stenhouse* [1977] and in matrix form by *Hoyng and Melrose* [1977],

$$\mathbf{N_L} = \begin{pmatrix} N_0(k) \\ N_1(k) \\ \vdots \end{pmatrix}, \qquad \boldsymbol{f} = \begin{pmatrix} f_0(p) \\ f_1(p) \\ \vdots \end{pmatrix}. \tag{1.25}$$

The complete form of the quasilinear equations expanded in Legendre polynomials is quoted below. In this project we truncate the Legendre expansion at $\ell = \ell_{max}$, which modifies the expressions found in *Hoyng and Melrose* [1977]. Vector forms are now presented.

The wave equation is

$$\left[\frac{\partial}{\partial t} + \omega_p \boldsymbol{H}\left(\frac{3k}{k_D^2}\frac{\partial}{\partial z}\right)\right]\boldsymbol{N}_L = \boldsymbol{\sigma} - \boldsymbol{\Gamma}\boldsymbol{N}_L, \tag{1.26}$$

or, equivalently,

$$\frac{\partial N_\ell}{\partial t} + \frac{3\omega_p k}{k_D^2}\frac{\partial}{\partial z}\left(\frac{\ell}{2\ell-1}N_{\ell-1} + \frac{\ell+1}{2\ell+3}N_{\ell+1}\right) = \sigma_\ell - \sum_{m=0}^{\ell_{max}} \Gamma_{\ell m} N_m, \tag{1.27}$$

where

$$\sigma_n = \frac{2\pi^2 e^2 \omega_p}{\epsilon_0 \hbar k^3}\int_{p_\phi}^{\infty} dp \frac{p^2}{v} P_n\left(\frac{\omega_p}{kv}\right) f_n(p), \tag{1.28}$$

$$H_{nl} = \frac{n}{2n-1}\delta_{n,l+1} + \frac{n+1}{2n+3}\delta_{n,l-1}, \tag{1.29}$$

$$\begin{aligned}\Gamma_{nl} = {} & \frac{2\pi^2 e^2 \omega_p^2}{\epsilon_0 k^3}\sum_{s=|n-l|}^{\min\{|n-l|,\ell_{max}\}} \frac{2n+1}{2} A_{nsl} \\ & \times \left\{ \frac{p_\phi^2}{v_\phi^2} f_s(p_\phi) + \int_{p_\phi}^{\infty} dp \frac{2p}{c^2} P_s\left(\frac{\omega_p}{kv}\right) f_s(p) \right. \\ & \left. + \left[\left(\frac{\omega_p}{kc}\right)^2 - 1\right]\int_{p_\phi}^{\infty} dp \frac{p}{v v_\phi} P_s'\left(\frac{\omega_p}{kv}\right) f_s(p) \right\}.\end{aligned} \tag{1.30}$$

In (1.26) the total derivative with respect to time is on the left hand side; the matrix $\mathbf{H}$ is part of the spatial derivative term $\mathbf{v}_g \cdot \partial/\partial z$ and appears from the orthogonality relations and the assumption that the group velocity of

the waves $\mathbf{v}_g$ is in the direction of the magnetic field, $\hat{z}$. The term $P_s'(x) = d/dx\,(P_s(x))$ can be rewritten in terms of the associated Legendre polynomials P_ℓ^m. An important note about (1.30) is that the gradient of the distribution function $\partial f/\partial \mathbf{p}$ present in (1.10) is removed from (1.30) by partial integration. A full physical understanding of the three terms that make up (1.30) can be found in *Melrose and Stenhouse* [1977], a brief summary is that the first term corresponds to the contribution of the isotropic part of the distribution, the final term is due to anisotropy and the middle term is an explicitly relativistic contribution. Specifically, the term $\int_{p_\phi}^{\infty} dp\; 2p/c^2 P_s(\omega_p/kv) f_s(p)$ vanishes under a nonrelativistic assumption and emerges only after carefully considering the relationship between momentum and velocity, namely $p = m\gamma(v)v$, where γ is the Lorentz factor.

The particle equation (1.11) is treated in the same way. Before writing it down in Legendre expanded form, it is useful to see it in spherical polar coordinates under the axisymmetric assumption. Then (1.11) becomes:

$$\begin{aligned}\frac{df}{dt} = &\frac{1}{p^2}\frac{\partial}{\partial p}p^2\left\{D_{pp}\frac{\partial}{\partial p} - \frac{1}{p}D_{p\alpha}w(\mu_p)\frac{\partial}{\partial \mu_p} + A_p\right\} f \\ &- \frac{1}{p}\frac{\partial}{\partial \mu_p}w(\mu_p)\left\{D_{\alpha p}\frac{\partial}{\partial p} - \frac{1}{p}D_{\alpha\alpha}w(\mu_p)\frac{\partial}{\partial \mu_p}\right\} f,\end{aligned} \tag{1.31}$$

using the convenient variables $w(\mu_p) = (1-\mu_p^2)^{1/2}$ and $\mu_p = \cos\alpha$.

Expanding $f(\mathbf{p})$ in Legendre polynomials $P_\ell(\cos\alpha)$ and using the matrix form above, the derivatives in angle are performed and the resulting complete expansion is

$$\left(\frac{\partial}{\partial t} + v\mathbf{H}\frac{\partial}{\partial z}\right)\boldsymbol{f} = \frac{1}{p^2}\left\{\frac{\partial}{\partial p}\boldsymbol{P}\frac{\partial}{\partial p} + \frac{\partial}{\partial p}\boldsymbol{Q} + \boldsymbol{R}\frac{\partial}{\partial p} + \boldsymbol{S}\right\}\boldsymbol{f}, \tag{1.32}$$

where $\mathbf{P}$, $\mathbf{Q}$, $\mathbf{R}$ and $\mathbf{S}$ are matrices that are given by the Legendre orthogonality relations. Equivalently the component form of (1.32) is

$$\begin{aligned}&\frac{\partial f_l}{\partial t} + v\frac{\partial}{\partial z}\left(\frac{l}{2l-1}f_{l-1} + \frac{l+1}{2l+3}f_{l+1}\right) \\ &= \frac{1}{p^2}\sum_{m=0}^{\ell_{max}}\left\{\frac{\partial}{\partial p}P_{lm}\frac{\partial f_m}{\partial p} + \frac{\partial}{\partial p}Q_{lm}f_m + R_{lm}\frac{\partial f_m}{\partial p} + S_{lm}f_m\right\},\end{aligned} \tag{1.33}$$

where $\ell_{\max}$ is the index at which the expansion is truncated. Formally, one takes $\ell_{max} = \infty$. Explicitly, the matrix elements of the terms in (1.32) and (1.33) are [*Hoyng and Melrose*, 1977]

$$P_{\ell m} = \frac{e^2\hbar\omega_p^3}{4\pi\epsilon_0}\frac{p^2}{v^3}\sum_{s=|\ell-m|}^{\min\{\ell_{max},\ell+m\}}\frac{2\ell+1}{2}A_{\ell sm}\int_{\omega_p/v}^{\infty}\frac{dk}{k}N_s(k)P_s(\omega_p/kv), \quad (1.34)$$

$$Q_{\ell m} = \frac{e^2\omega_p^2}{4\pi\epsilon_0}\frac{p^2}{v^2}\log(v/V_e)\delta_{\ell l} - \frac{e^2\hbar\omega_p^3}{4\pi\epsilon_0}\frac{p}{v^3}\sum_{s=|\ell-m|}^{\ell+1}\frac{2\ell+1}{2s(s+1)}\lambda^{(1)}_{\ell sm} \times\int_{\omega_p/v}^{\infty}\frac{dk}{k}\left[\left(\frac{kv}{\omega_p}\right)^2-1\right]^{1/2}N_s(k)P_s^1\left(\frac{\omega_p}{kv}\right), \quad (1.35)$$

$$R_{\ell m} = \frac{e^2\hbar\omega_p^3}{4\pi\epsilon_0}\frac{p}{v^3}\sum_{s=|\ell-m|}^{\min\{\ell_{max},\ell+m\}}\frac{2\ell+1}{2s(s+1)}\lambda^{(1)}_{ms\ell}A_{\ell sm}\int_{\omega_p/v}^{\infty}\frac{dk}{k}\left[\left(\frac{\omega_p}{kv}\right)^2-1\right]^{1/2} \times N_s(k)P_s^1\left(\frac{\omega_p}{kv}\right), \quad (1.36)$$

$$S_{\ell m} = -\frac{e^2\hbar\omega_p^3}{4\pi\epsilon_0 v^3}\sum_{s=|\ell-m|}^{\min\{\ell_{max},\ell+m\}}\frac{2\ell+1}{2}A_{\ell sm}\int_{\omega_p/v}^{\infty}\frac{dk}{k}\frac{1}{2}\left[\left(\frac{kv}{\omega_p}\right)^2-1\right]N_s(k) \times\left[\lambda^{(1)}_{s\ell m}P_s\left(\frac{\omega_p}{kv}\right)+\frac{(s-2)!}{(s+2)!}\lambda^{(2)}_{s\ell m}P_s^2\left(\frac{\omega_p}{kv}\right)\right], \quad (1.37)$$

where

$$\lambda^{(1)}_{\ell sm} = \frac{1}{2}[s(s+1)+m(m+1)-\ell(\ell+1)], \quad (1.38)$$

$$\lambda^{(2)}_{s\ell m} = \frac{1}{2}\Big\{s(s+1)\big[\ell(\ell+1)+m(m+1)\big]-\big[\ell(\ell+1)-m(m+1)\big]^2\Big\}, \quad (1.39)$$

$$A_{\ell sm} \equiv \int_{-1}^{+1}P_\ell(x)P_s(x)P_m(x)dx = 2\frac{(\ell+s-m)!(\ell+m-s)!(s+m-\ell)!}{(\ell+s+m+1)!}\left[\frac{\Sigma!}{(\Sigma-\ell)!(\Sigma-s)!(\Sigma-m)!}\right]^2, \quad (1.40)$$

$$2\Sigma = \ell+s+m. \quad (1.41)$$

The equations (1.26 - 1.30) and (1.32 - 1.41) are the complete expansion of the 3D axisymmetric electron-Langmuir wave interaction in Legendre polynomials.

1.7 Two and Three-Dimensional studies

Axisymmetric numerical models for wave growth and electron evolution as a result of the backreaction have been developed before, notably by *Appert et al.* [1976] and *Ziebell et al.* [2008a,b, 2011]. These models emphasise effects for the resonant speed $v = v_\phi$, and the effects discussed in this thesis due to resonances with $v > v_\phi$ do not appear to have been considered before. However, we summarise the development of higher-dimensional work below.

In *Ziebell et al.* [2008a] a 3D analogue of the 1D equations is employed, with the 1D resonance and wave growth condition. A beam speed of $v_b = 5v_e$ is considered, which is small enough such that modulational effects need not be considered. However, such a small beam speed is generally considered inadequate to explain the source motion in Type III solar radio bursts. In *Ziebell et al.* [2008b] three-wave decay and scattering processes are included. These analyses find that Langmuir waves form a circular ring in $k-$ space, with 1D-like quasilinear relaxation. However, the electrons remain primarily 1D-like in Figure 1.12, with diffusion in 1D parallel to $\boldsymbol{B}$ that appears very similar to the quasilinear relaxation in Figure 1.11 [*Grognard*, 1975, 1985]. Examples of these results for quasilinear relaxation only are shown in Figure 1.12.Similarly, in *Ziebell et al.* [2014] and *Ziebell et al.* [2015] a 2D assumption is used - with this restriction there is no pitch angle diffusion operator.

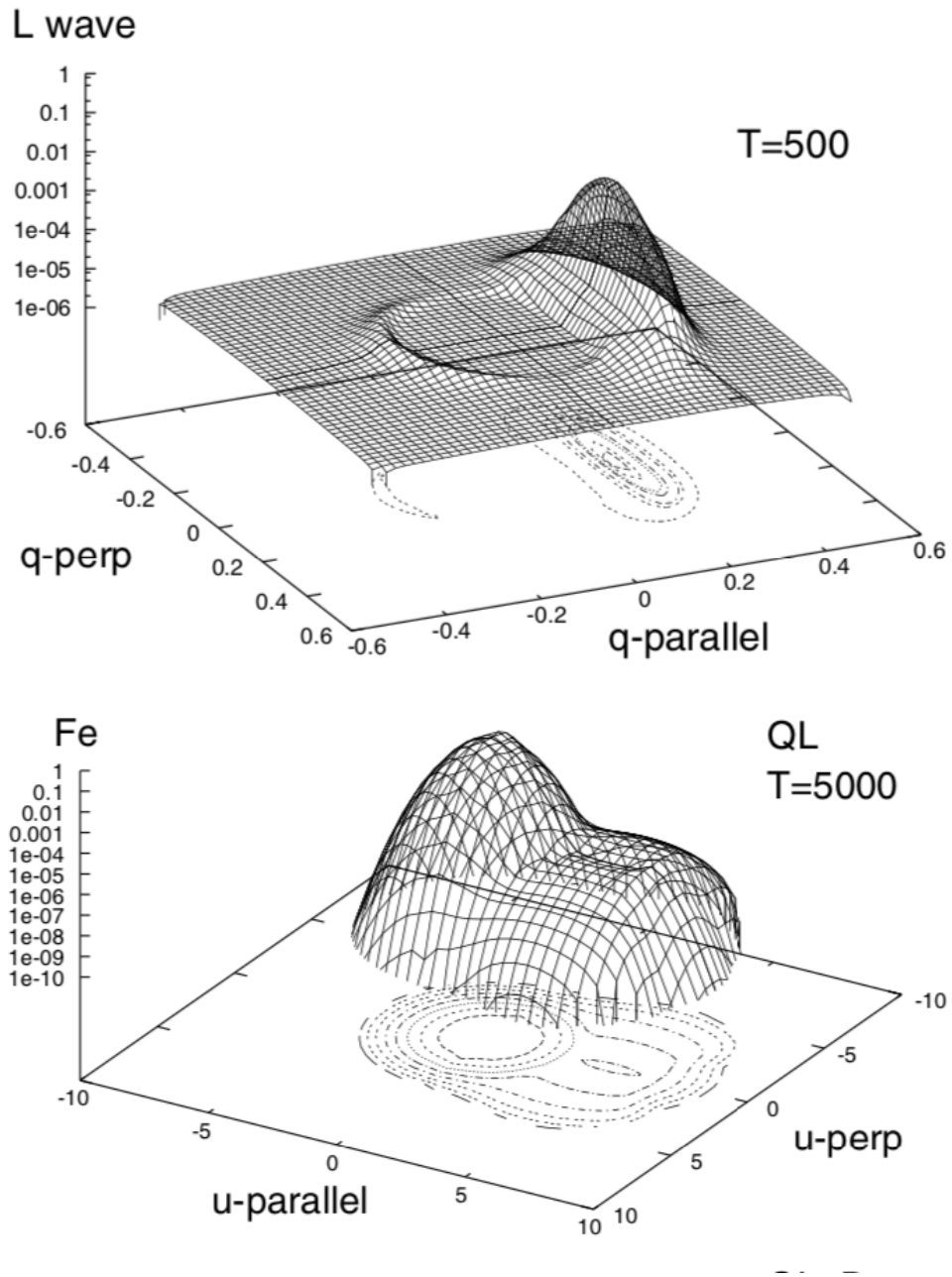

Figure 1.12: Wave (top) and particle (bottom) distributions from *Ziebell et al.* [2008b]. The waves form a circular ring with a peak that has a significant angular dimension, but the particles predominantly relax in $u_{\parallel}$.

These previously conducted 3D axisymmetric models emphasize the effects for the resonant speed, $v = v_{\phi}$, rather than the resonances with $v > v_{\phi}$ which

are developed in this thesis.

Chapter 2

Offset Power-Law Dependence of the Sun's Radial Electron Density Profile: Evidence and Implications

[Published as J.C. Harding, Iver H. Cairns and Vasily Lobzin Ap. J. *877* (2019)]

2.1 Abstract

The radial electron density profile $n_e(r)$ of the Sun's corona and solar wind contain information on the sources, heating, and acceleration of the coronal and solar wind plasma. Currently several empirically-derived density models are used to describe the corona, with varying degrees of success and little physical justification or predictive power. The offset power-law (OPL) profile $n_e(r) = A(r - r_0)^\alpha$, with radial offset r_0 and power-law index α, models radial outflow from r_0 that conserves total electron number and may be accelerated and heated (affecting α), thus having physical significance and predictive power. We fit the OPL model to multiple sets of published radial density profiles obtained from spectroscopic, white light, and radio data from different regions on the Sun and during different periods of solar activity. We demonstrate that this model fits these data very well, in every case better than the other commonly-used density models considered. The spectroscopic and white light data yield r_0 very close to one solar radius R_S (in detail $r_0 = (1.02 \pm 0.06)R_S$, where the the uncertainties are taken using a standard error of the mean) and

$< \alpha >= 2.4 \pm 0.2$, consistent with plasma originating near the chromosphere and acceleration similar to the nominal Parker solar wind model. Radio burst data yield flatter profiles $\alpha < 2$, suggesting that pre-flare activity alters the density profile by increasing the coronal density at large heights. We discuss the possible interpretations and implications for coronal physics and solar radio bursts.

2.2 Introduction

The heating of the solar corona and the acceleration of the solar wind are two of the most important and longstanding unsolved problems for space physics and astrophysics. Eclipse photographs and images from X-rays to the radio show that the number density of electrons $n_e(\mathbf{r})$ varies as a function of position $\mathbf{r}$ and reveal the existence of multiple time-varying structures that link the photosphere, chromosphere, and corona. These structures include sunspots, magnetic loops, active regions, and coronal holes. The radial profile of the density $n_e(r)$ is a fundamental quantity for understanding the domains between the photosphere and the corona and solar wind, often varying with heliolongitude and heliolatitude as a result of the foregoing structures. This radial density profile contain signatures of both heating and acceleration: heating because a heated plasma tends to expand, thereby altering the density profile, while acceleration leads to changes in the density profile because mass conservation requires that the electron number density and radial speed are coupled. Two components of the solar wind can be identified at solar minimum - the fast (> 750 kms^{-1}) and slow (< 500 km s^{-1}) solar wind. *Cranmer* [2009] Section 5 outlines the major theoretical paradigms for the acceleration of the solar wind as a whle, as well as a closer focus on the fast solar wind. It is well accepted that the fast wind originiates in coronal holes and the slow wind is related to streamer belt regions. *Abbo et al.* [2016] provides a review of the slow solar wind observations and modelling, which we refer to directly in Section 4. Unfortunately it is not easy to obtain accurate observations and models for the Sun's density profile, or to interpret them. The recent and impending launches of NASA's Parker Solar Probe [*Fox et al.*, 2016] and ESA's Solar Orbiter [*Müller et al.*, 2013], respectively, make it particularly timely to obtain better models and interpretations for the Sun's density profile and the associated acceleration and heating of the coronal and solar wind plasma.

Several techniques are currently used to measure coronal and solar wind

density profiles: spectroscopic observations, inversion of Thomson-scattered "white light" data, and the heights of the source regions of type II and III solar radio bursts. These are now described briefly in turn, together with their issues.

Spectroscopic techniques can yield the plasma flow speed via Doppler shifts of individual spectral lines and the electron density and temperature by comparing pairs of spectral lines [*Withbroe*, 1988; *Ko et al.*, 2002; *Strachan et al.*, 2002], sometimes in conjunction with Thomson scattering analyses and sometimes without. These typically involve line-of-sight effects, via projection of multiple possible source regions along the line-of-sight, although emission from one height may dominate. This is expected to be the case for lines-of-sight beyond the Sun's limb.

Thermal, white-light, solar radiation undergoes Thomson scattering by thermal electrons. With more scattering expected where n_e is larger and/or the radiation flux is larger, the radiation intensity across the Sun should depend on both $n_e(\mathbf{r})$ and intrinsic variations in the radiation flux at the photosphere (and above). Typically the intensity of Thomson-scattered light in a given direction θ is written as a path integral [*Billings*, 1966; *Manchester et al.*, 2008; *Schmidt and Cairns*, 2016]

$$I(\theta, l_o) = A \int_{l_i}^{l_o} dl \; n_{sw}(\mathbf{r}) F(\mathbf{r}), \tag{2.1}$$

where F is a function that describes the geometry and source function of the radiation and dl is an increment along the path between the observer at l_o and the initial point l_i. Tomographic inversion, with or without approximations like localised radial fall-offs, is then used to extract the radial profile $n(r)$ along lines of specified, constant, heliolongitude and heliolatitude [*Munro and Jackson*, 1977; *Saito et al.*, 1977; *Kohl et al.*, 1998; *Guhathakurta et al.*, 1999; *Esser et al.*, 1999; *Hayes et al.*, 2001; *Strachan et al.*, 2002; *Gopalswamy et al.*, 2018].

Type II and III solar radio bursts contain information on $n_e(r)$ since they are produced at time-varying frequencies $f(t)$ near the electron plasma frequency $f_p(r)$ and near $2f_p(r)$ in the source region, as well as likely suffering scattering between the source and observer [*Melrose*, 1986]. The connection to the density is via

$$f_p(r) = 8.98 \; n_e(r)^{1/2} \text{ Hz} = f/k \; , \tag{2.2}$$

for n_e measured in m^{-3} and $k = 1$ for fundamental and $k = 2$ for harmonic radiation, respectively. One approach to finding $n_e(r)$ is to use the radiation's

frequency drift rate, via

$$\frac{df}{dt} = \frac{v_{\rm ex} f}{n_e}\frac{dn_e}{dr} \ , \tag{2.3}$$

where the speed v_{ex} of the source exciting the radiation is coupled to the density profile and frequency drift rate [*Ginzburg and Zheleznyakov*, 1958; *Wild and McCready*, 1950; *Suzuki and Dulk*, 1985; *Reiner et al.*, 2001]. However, neither v_{ex} or $n_e(r)$ is known *a priori*. An alternative is to combine the source motion $r(t) = r_{s0} + v_{ex}(t - t_0)$ for constant v_{ex} and $r(t_0) = r_{s0}$ with an offset power-law (OPL) model [*Lobzin et al.*, 2008]

$$n_e(r) = C(r - r_0)^{-\alpha} \ , \tag{2.4}$$

where r_0 is a radial offset and α is the power-law index: then [*Cairns et al.*, 2009]

$$f(t) = a(t - b)^{-\alpha/2} \tag{2.5}$$

with

$$a = mC^{1/2} v_{ex}^{-\alpha/2} \ , \ b = t_0 + (r_0 - r_{s0})/v_{ex} \ . \tag{2.6}$$

Thus α, a, and b can be obtained directly by fitting $f(t)$ to Eq. 2.5. Crucially, the power-law exponent α for the density profile can be obtained without needing to know $v_{\rm ex}$, r_0, r_{s0}, m, or C, a significant advance over most previous work on coronal density models which required either $v_{\rm ex}$ or $r(t)$ to be assumed [*Lobzin et al.*, 2008; *Cairns et al.*, 2009; *Lobzin et al.*, 2010].

A major problem with the radio approach is that both fundamental (especially) and harmonic radiation are subject to refraction towards low density regions and to scattering by high density regions. These density inhomogeneities can be on large scales (e.g., structures visible in eclipse and other images) and small scales (turbulence). Differences between the density profiles in radio data and both white-light and spectroscopic data are routinely interpreted in terms of scattering and/or ducting moving the radio waves from their true source height to larger heights at which radiation is released [*Duncan*, 1979; *Robinson and Cairns*, 1998; *Thejappa and MacDowall*, 2008; *Zucca et al.*, 2014; *McCauley et al.*, 2017; *Kontar et al.*, 2017; *McCauley et al.*, 2018; *Mann et al.*, 2018; *Zucca et al.*, 2018]. While current radio emission theories rely on density fluctuations to explain fundamental-to-harmonic frequency ratios and to restrict the intensity of fundamental radiation [*Robinson and Cairns*, 1998; *Li*

et al., 2008], it remains controversial how much scattering and ducting affect the apparent source heights and inferred density.

Longstanding issues exist concerning the applicability and physical interpretation of many published density models for the corona and solar wind. Table 2.1 summarises the functional forms of the Baumbach-Allen model [*Baumbach*, 1937; *Allen*, 1947] and those of *Parker* [1958], *Newkirk* [1961], *Saito et al.* [1977], *Leblanc et al.* [1998] and *Cairns et al.* [2009]. The functional forms of these models are evidently quite different. One major reason for the proliferation of models is simple: often their functional forms do not fit observed density profiles well, therefore motivating searches for replacements. Quantitative scaling of models up and down in magnitude, for instance using a $2\times$ *Saito et al.* [1977] model, is also common and is interpreted reasonably in terms of the entire density profile shifting up or down in magnitude due to variations in the plasma sources with solar activity and the local photospheric and chromospheric environment.

Another major reason for the proliferation is that for some models the physics is not obvious and is instead empirical. For instance, the *Newkirk* [1961] model is a fluid gravitational-settling model for constant temperature, with a Boltzmann factor involving the ratio of the gravitational potential energy and the thermal energy $k_B T$. In contrast, the Baumbach-Allen and Saito et al. models are strictly empirical fits to white-light data, while the *Parker* [1958] model and similar r^{-2} terms embody conservation of electrons for constant radial flow speed, and the *Leblanc et al.* [1998] model extends the r^{-2} [*Parker*, 1958] model by empirically adding the obvious Taylor series expansion terms involving r^{-4} and r^{-6}. The interpretations of the r^{-6} and r^{-16} terms in the Baumbach-Allen and Saito et al. models and the missing Taylor terms r^{-2N} terms (for integer N) are entirely unclear. In contrast, the physics of the *Cairns et al.* [2009] model is relatively simple: it corresponds to locally conical and radial outflow from a source on a sphere of radius r_0 (section III of *Parker* [1958]), for which electron conservation requires

$$n_e(r) v_p(r) (r - r_0)^2 = \text{constant}. \tag{2.7}$$

Accordingly, the index α in Eq. (2.4) contains information on the plasma outflow speed $v_p(r)$ and electron conservation while r_0 locates the source of the outflowing plasma. However, what should r_0 and α be and how well does this model fit data?

In this paper we address all the foregoing issues by quantitatively analysing published density profile data from multiple authors and testing all the above

models in an even-handed way. The focus is primarily on white-light and spectroscopic data, since these have less serious interpretative issues. The primary result found is that in all cases analysed the offset power law (OPL) form (2.4) [*Lobzin et al.*, 2008; *Cairns et al.*, 2009] works very well and is a much better fit than the other models. Sometimes a dual OPL form - that is, two separate fits to (2.4) over different ranges of r - is an improvement over the single OPL model. The range of α found for the corona and solar wind is $1.3 - 3.2$, with the chromospheric model of *Avrett and Loeser* [2008] having $\alpha = 0.74 \pm 0.02$. The average for the coronal and solar wind datasets is $\langle\alpha\rangle = 2.4 \pm 0.2$. Finding that $\langle\alpha\rangle$ is larger than 2 is direct physical evidence for outwards acceleration of the wind and the associated acceleration profile from Eq. (2.7) agrees well with published speed data. Both the 2 and 3−parameter fits show that $r_0 = (1.02 \pm 0.06)R_S$; the obvious physical interpretation is that the outwards acceleration of the coronal and solar wind plasma starts very close to the chromosphere and photosphere. Finally, comparisons with density profiles obtained from type II and III solar radio bursts provide strong evidence that these profiles are flatter, with smaller values of α. This is interpreted in terms of extra plasma being moved to larger heights before flares and radio bursts occur, not unreasonable for pre-heating scenarios. Although confirmation is needed, this suggests that the plasma density is higher at larger heights in these source regions, thereby directly reducing the need for scattering and ducting to be important and providing an argument that type II and III bursts are likely to occur preferentially in regions that are denser than the ambient corona and solar wind. This complements other analyses [*McCauley et al.*, 2018].

The paper proceeds as follows. Section 2 briefly describes the provenance of the data sets analysed. The results are presented in Section 3 and then discussed and interpreted in Section 4. The final section contains the conclusions.

Model	Baumbach-Allen	Parker	Newkirk
$n_e(r) =$	$Ar^{-6} + Br^{-16}$	Ar^{-2}	$Ae^{B/r}$
Model	Saito et al.	Leblanc et al.	Cairns et al. (OPL)
$n_e(r) =$	$Ar^{-2.14} + Br^{-6.13}$	$Ar^{-2} + Br^{-4} + Cr^{-6}$	$C(r - r_0)^{-\alpha}$

Table 2.1: Published density models for $n_e(r)$ in m^{-3}, with A, B, C, r_0, and α arbitrary constants.

2.3 Data provenance

Table 2.2 lists the references for the 12 coronal spectroscopic and/or white light datasets analysed in this paper in one column, together with the *Avrett and Loeser* [2008] chromospheric model and the *Magdalenić et al.* [2010] radio datasets. The coronal datasets are chosen since they are all well regarded by the solar community and were developed and published by multiple independent sets of authors using different instruments in different years and at multiple phases of several solar cycles. For instance, the density profiles obtained from white-light data are for multiple polar coronal holes in 1973 [*Munro and Jackson*, 1977] and 1996-97 [*Kohl et al.*, 1998; *Esser et al.*, 1999], an equatorial (solar minimum) and a polar coronal hole (solar maximum) [*Withbroe*, 1988], a polar coronal hole and plumes in 1996 [*Guhathakurta et al.*, 1999], an equatorial region in 1998 [*Hayes et al.*, 2001], and an equatorial streamer in 1997 [*Strachan et al.*, 2002]. Similarly, the profiles derived from spectroscopic data without white light data are above a mid-latitude active region in 1998 [*Ko et al.*, 2002]. The data of *Withbroe* [1988] come both from spectroscopic and white-light observations, which yield consistent results, for an equatorial and a polar coronal hole. Together, these datasets constitute a relatively unbiased set of data for this paper's analyses. The data cover the range $r/R_S \approx 1.1 - 6$.

The data for these datasets were obtained by applying the freeware program DataThief to pdf files of the published figures. The uncertainties estimated from this procedure are much less than 5% of the plotted values.

2.4 Analyses and Results

Figure 2.1 plots 9 of the 14 datasets for $n_e(r)$ referenced in Table 1, using a standard linear - linear format, together with the corresponding fits to Eq. (2.4) for $r_0 = 1$. Very good agreement with Eq. (2.4) is apparent. Table 2.2 quantifies the values of α and C for each fit, as well as the goodness-of-fit via the reduced Chi-squared parameter, χ^2_r. The uncertainties σ corresponding to each point in each dataset are either taken from the original references using DataThief or are assumed to be 5% of the particular sample's value. As usual, statistically significant fits have $\chi^2_r \approx 1$. Evidently the OPL fits to the datasets are statistically very good.

Figure 2.2 compares fits to the Baumbach-Allen and Saito et al. models, where the fitting variable is a multiplicative constant to the functional form in

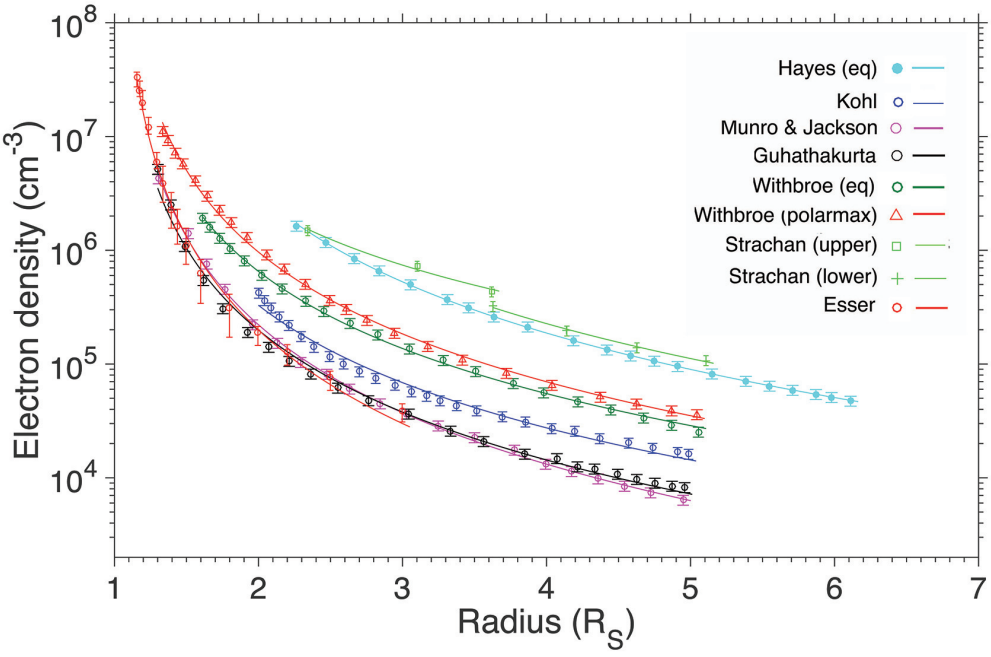

Figure 2.1: Density profiles $n_e(r)$ versus r/R_S on linear scales for 9 of the 12 spectroscopic and white-light datasets in Table 2.2, as indicated in the Key. Symbols identify data points and solid lines the corresponding OPL best-fits to Eq. (2.4) for $r_0 = R_S$.

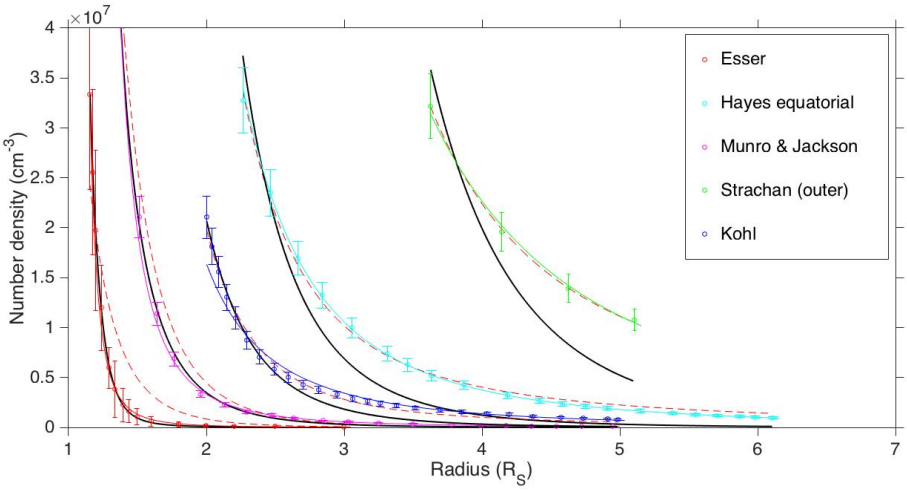

Figure 2.2: OPL fits compared to the *Baumbach* [1937] − *Allen* [1947] (black) and *Saito et al.* [1977] (dashed red) fits for selected datasets. The data and fits were multiplied by a factor for visibility: 1×, 20×, 15×, 100×, and 50× for the *Esser et al.* [1999], *Hayes et al.* [2001] "equatorial", *Munro and Jackson* [1977], *Strachan et al.* [2002] "outer", and *Kohl et al.* [1998] datasets, respectively.

Table 2.1, with the OPL model for several datasets. Clearly the former models do not have the right slopes in general to match the observations well, although the OPL does. The values of χ^2_r in Table 2.2 show that the OPL model provides a much better statistical fit to the datasets than the Baumbach-Allen model, with similar results (not shown) for the Saito et al. model.

A much more striking and direct argument for the OPL model is obtained by plotting all 12 datasets in a log-log format. The reason is that Eq. (2.4) predicts that power-laws in $(r - r_0)$ become straight lines. Figure 2.3 demonstrates directly that all 14 datasets (including the *Avrett and Loeser* [2008] model and *Magdalenić et al.* [2010] radio dataset) are very well represented as straight lines in this $\log n_e(r) - \log(r - R_S)$ space, corresponding to $r_0 = R_S$. This provides very strong and immediate evidence for Eq. (2.4)'s offset power-law model with $r_0 \approx R_S$.

It is apparent from Table 2.2 that the fits to Eq. (2.4) are strongly statistically significant for all the datasets considered. In contradistinction, the fits to the other models are statistically poor for all except 2 of the 12 spectroscopic or white-light datasets (the Guhathakurta et al. "inner" and Ko et al. datasets) and are much worse than for the OPL model in 13 of the 14 datasets analyzed. Indeed only for the *Magdalenić et al.* [2010] dataset is χ^2_r larger for the OPL

model than the scaled Baumback-Allen model, and even then the OPL provides an excellent statistical fit since $\chi^2_r = 0.08$.

Wide ranges of normalisation constants and power-law indices are apparent from the range of intercepts and slopes of the lines in Figure 2.3, as well as from the range of heights for a given n_e in Figures 2.1 - 2.3. Note that $C = n_e(r = 2R_S)$ for $r_0 = 1.0R_S$ by rewriting Eq. (2.4) as

$$n_e(r) = n_e(r = 2R_S) \left(\frac{1R_S}{r - 1.0R_S} \right)^{\alpha} . \tag{2.8}$$

From Table 1 the fitted values of α for the spectroscopic and white-light datasets lie in the range $1.3 - 3.2$ with typical uncertainties of ± 0.2, while $C = n_e(r = 2R_S)$ lies in the range $1.1 \times 10^5 - 3.4 \times 10^6$ cm^{-3}. In contrast the *Avrett and Loeser* [2008] chromospheric model has $\alpha = 0.74 \pm 0.02$ and $n_e(r = 2R_S) = (1.3 \pm 0.1) \times 10^7$ cm^{-3}, thereby having a much shallower slope and denser normalisation than the coronal datasets. A similar conclusion follows for the radio dataset of *Magdalenić et al.* [2010], which has $\alpha = 1.34 \pm 0.15$ and $n_e(r = 2R_S) = (3.0 \pm 1.0) \times 10^7$ cm^{-3}.

Figure 2.3 and Table 2.2 include the results of fitting the *Guhathakurta et al.* [1999] and *Kohl et al.* [1998] datasets with Eq. (2.4) in two separate ranges of r, whereas other data sets are fitted with Eq. (2.4) over the whole range. It is not shown here that fitting a single OPL model to these "inner" and "outer" domains leads to reasonable fits; however, the figure and table show that the two-region models provide superior fits, with clear evidence for different slopes in the two domains. Thus the coronal datasets sometimes support more complicated OPL models, providing evidence of additional density structures and associated physics.

Quantifying the observed value of the radial offset r_0 proceeds as follows. A first approach is to calculate the best fits to Eq. (2.4) for varying α and C but specific assumed values of r_0 for the coronal datasets and to seek the minimum value of χ^2 for these fits as a function of r_0. Figure 2.4 presents the results of this approach for several datasets, demonstrating that clear minima exist in the curves of $\chi^2(r_0)$ near $r_0 = (1.02 \pm 0.06)R_S$. These minima provide good justifications for the value $r_0 = 1.0R_S$ assumed in the analyses presented earlier.

The second approach is to fit the data to Eq. (2.4) for r_0, α and C all free parameters. Table 2.3 provides the resulting fit parameters and χ^2_r. Comparing the results in Tables 2.2 and 2.3 it is clear that the 3-parameter fits are even better than the 2-parameter fits, that in terms of the average and standard

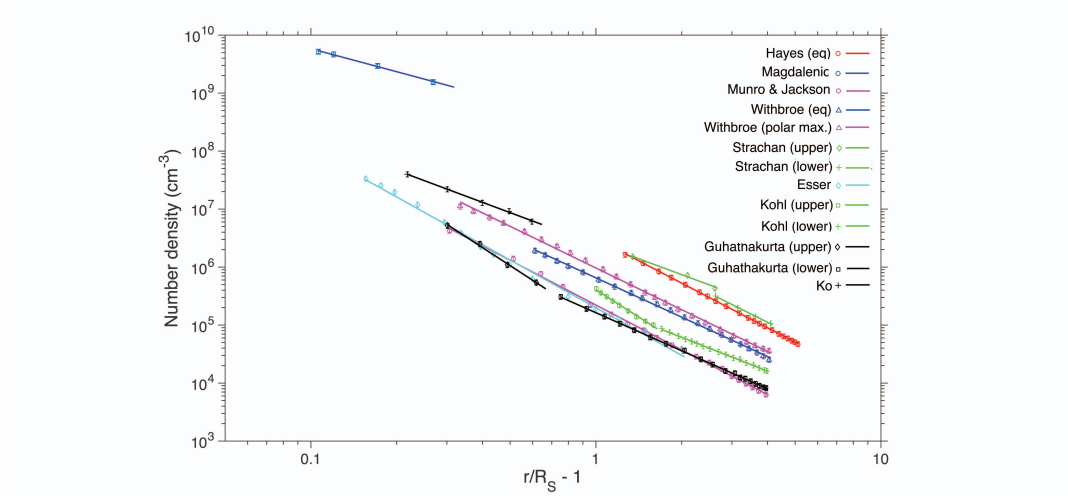

Figure 2.3: Density profiles $n_e(r)$ versus $(r - R_S)/R_S$ on log-log scales for all 14 of the datasets in Table 2.2, as indicated in the Key. Symbols identify data points and solid lines the corresponding OPL best-fits to Eq. (2.4) for $r_0 = R_S$.

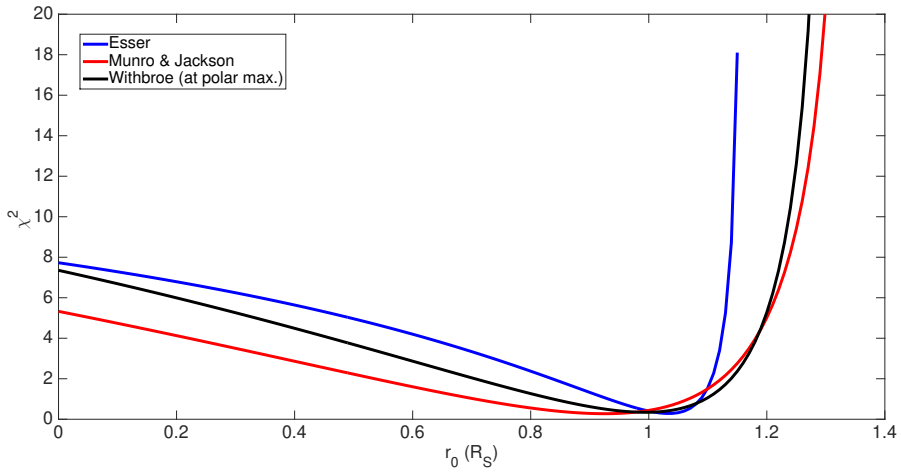

Figure 2.4: Solutions for χ^2_r as a function of r_0/R_S obtained by fitting Eq. (2.4) with α and C as free parameters for specified r_0 for the three datasets indicated. Clear minima in χ^2_r are evident near $r_0 = 1.02R_S$.

deviation $r_0 = (1.02 \pm 0.06)R_S$ discounting the outlier *Strachan et al.* [2002] values and the non-spectroscopic and non-white-light datasets, and that the values of α and C differ little between the 2- and 3-parameter fits. It is thus a very robust conclusion that r_0 corresponds closely to the very low corona, chromosphere, and photosphere.

2.5 Interpretation and Discussion

Tables 2.2-2.3 and Figures 2.1-2.4 show that the OPL model is a very good fit statistically and that $r_0 = (1.02 \pm 0.06)R_S$ on average. In comparison, the chromosphere's height of 10,000 - 40,000 km corresponds to about $(0.01 - 0.05)R_S$. We interpret this to mean that that the effective source surface for the outflowing coronal plasma and solar wind is within $0.21R_S$ of the chromosphere, thereby including the photosphere, chromosphere, and lowest portion of the corona, all being consistent within the error bars. The funnels of *Tu et al.* [2005] remain consistent with the values of r_0 found and the foregoing interpretation. The density profile results strongly imply that the effective source surface of the solar wind is much lower than the Alfven surface near $5 - 15R_S$ considered by *DeForest et al.* [2013] and *Tasnim and Cairns* [2016].

The *Cairns et al.* [2009] OPL model is justified physically in terms of conical outflow from a point on a sphere and mass conservation: specifically conservation of number flux via $\nabla.(n(\mathbf{r})\mathbf{v}(\mathbf{r})) = 0$ yields Eq. (2.7), which for constant wind speed $v_{sw} = v_p$ implies $\alpha = 2$ and

$$n_e(r) = A\,(r - r_0)^{-2} \quad . \tag{2.9}$$

If the solar wind is accelerating at small r, then we expect larger $n_e(r)$ at smaller r and smaller $n_e(r)$ at larger r to compensate. In terms of Eqs (2.4) and (2.7) we have

$$n_e(r) = Bv_w(r)^{-1}(r - r_0)^{-2} = C(r - r_0)^{-\alpha} \; . \tag{2.10}$$

Thus α should be larger than 2 if the wind accelerates from small to large r. The mean and standard deviation of the spectroscopic and white-light datasets in Table 2.2 is 2.4 ± 0.2. Accordingly, the combination of the very good OPL fits in Figures 2.1-2.3 with $< \alpha >= 2.4 \pm 0.2 > 2.0$ in Table 2.2 is prima facie evidence for solar wind acceleration at small r,assuming locally spherical outflow in a conical region. This assumption does not contradict the fact that the

solar corona is highly inhomogeneous and asymmetric.

Rearranging Eq. (2.10) yields

$$v(r) = \frac{B}{C}(r - r_0)^{\alpha-2}. \tag{2.11}$$

Thus, with $< \alpha >= 2.4 \pm 0.2$ from Table 2.2 Eq. (2.11) predicts that $v_r(r) \propto (r-r_0)^{0.4\pm0.2}$, while the median value $\alpha = 2.52$ yields $v_r(r) \propto (r-r_0)^{0.5}$. Figure 2.5 compares these predictions with the *Parker* [1958] model and the observational constraints for $v(r)$ from *Strachan et al.* [2002]. The figure demonstrates that the OPL prediction is consistent with the available constraints and is not too different from the Parker model. Put another way, the density profiles analyzed and velocity constraints considered are consistent with the OPL model and provide clear evidence for acceleration of the wind at low coronal heights. Future analyses of other density and velocity datasets will provide better constraints and better test the OPL model.

The expectation that the solar wind has its source in the low corona is straightforward for the fast wind which is accelerated along open field lines in coronal holes. The prediction for the slow solar wind is more complicated, as there are several competing (and possibly complementary) theories concerning its origin [*Abbo et al.*, 2016]. *Sheeley et al.* [1997] suggested that the slow wind originates at heights near streamer cusps ($2.5R_S$), with material ejected by interchange reconnection. Our velocity prediction in Figure 2.5 is not consistent with this result - neither in the magnitude of the radial speed nor in the source of the outflow. However, alternative models, such as the "S-Web" and the expansion factor models, have the slow wind's origin inside the classical source surface. *Jones and Davila* [2009] observed streamer blob structures lower in the corona, pointing out the fact that the *Sheeley et al.* [1997] investigation used a larger occulting disk (the LASCO C2 coronograph). Their results suggested a different ejection mechanism for the blobs, perhaps footpoint exchange or streamer detachment, which would occur at lower altitudes. The distribution of streamer blob speeds is also significantly faster than that of *Sheeley et al.* [1997]. Both papers fit their data to a model given below in Equation 2.12 and these fits have been represented in Figure 2.5.

$$v^2 = 2a(r - r_1). \tag{2.12}$$

The *Jones and Davila* [2009] fit agrees extremely well with the OPL prediction in Fig 2.5. We include the velocity range we extracted from the *Strachan*

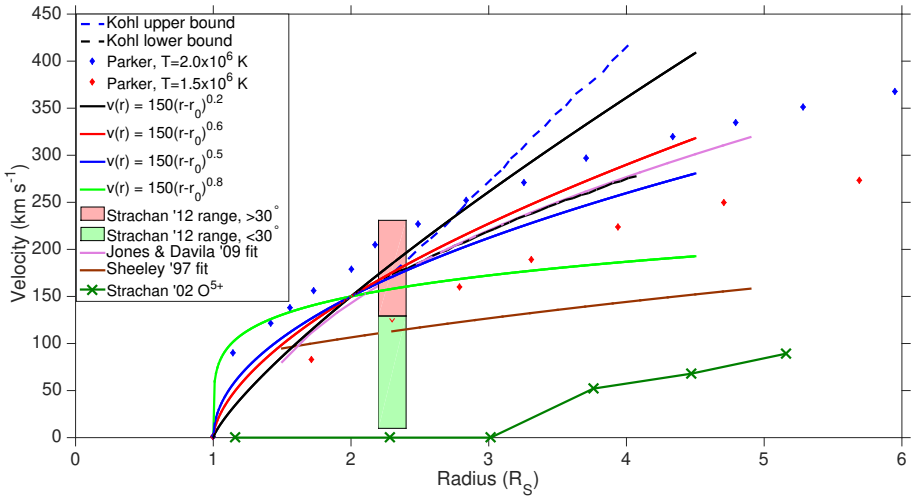

Figure 2.5: Comparisons of the OPL predictions for $v(r)$, given by Eq. (2.11) for various α and B/C is such that $v(r = 2r_0) = 150km/s$, with the constraints of *Strachan et al.* [2002] for the data of *Kohl et al.* [1998] and predictions from *Parker* [1958]. The velocity fit to Equation 2.12 from *Jones and Davila* [2009] is shown in purple. The *Sheeley et al.* [1997] streamer blob fit to the same and the *Strachan et al.* [2002] O^{5+} velocity profile are shown for contrast.

et al. [2012] global outflow velocity maps. These measurements were taken across the whole Sun at $r = 2.3R_S$. This suggests that velocity profiles in equatorial regions will be significantly lower than the OPL fits in Figure 2.5. As the factor B/C is a free parameter and expected to vary with time and position on the Sun this is not inconsistent with the OPL model, and is a rich direction for future analysis. Our final comment on the implication of our OPL results for the source of the solar wind outlflow is that the OPL model is not expected to strictly hold over the whole low corona at all times. We acknowledge the highly complex and asymmetric structure of the corona and this is not in conflict with our model. The O^{5+} measurement in a streamer core from *Strachan et al.* [2002] is an example of small-scale structure that may defy a strict application of the OPL model with $r_0 \approx 1R_S$.

Figure 2.6 compares the histograms of the indices α obtained from density profiles in this paper and from the frequency drift rates of type III solar radio bursts [*Cairns et al.*, 2009; *Lobzin et al.*, 2010]. (As explained near Eq. (2.5) the approach of these authors does not require knowledge of the exciter speed v_{ex} to predict α.) It is clear that the two histograms are different and that the values of α obtained from the radio bursts are much smaller (corresponding to flatter density profiles) than for the density profiles obtained from spectroscopic and white-light data. In detail, to two significant figures, the median, average, and standard deviation for α are 2.5, 2.4, and 0.2 versus 1.0, 1.3, and 1.1 for the spectroscopic and white-light density profiles in Table 2.2 and the radio studies (ignoring the outlier near 13.5), respectively.

The interpretation adopted for Figure 2.6's two different histograms for α is that the type II and III bursts occur in coronal regions which are no longer undisturbed but instead have a flatter density profile and have higher density plasma at larger heights. One model for this is that the higher density plasma was released previously from the active region as it evolved towards release of a CME / shock (for type II bursts) or else energetic electrons (for type III bursts), both involving magnetic reconnection. Put another way, evolution of the active region leads to plasma being ejected upward from the chromosphere or lower corona before the flare / CME, causing the corona's typically higher value of $\alpha > 2$ to become smaller. It is particularly attractive to consider a chromospheric source since $\alpha \approx 0.7$ in the chromospheric model of *Avrett and Loeser* [2008], so addition of chromospheric plasma to the corona will naturally reduce α.

The interpretation adopted above is not inconsistent with finding $\alpha \approx 1.34 \pm 0.15 < 2$ for the dataset of *Magdalenić et al.* [2010], which results from

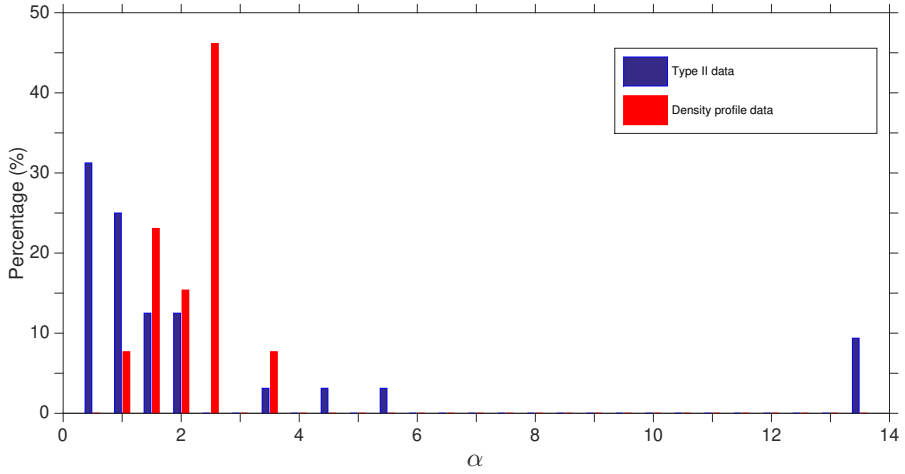

Figure 2.6: Histograms of α obtained for this paper's spectroscopic and white-light density profiles (red) and from analyses of type II solar radio bursts by *Cairns et al.* [2009] and *Lobzin et al.* [2010] (blue).

analysis of the source locations of radio bursts. The time for plasma moving at an average speed of 100 km s^{-1} (cf. Figure 2.5) to travel $0.5R_S$ is then 1.0 hr, so it would take a few hours for a steady enhanced density profile to be set up above an active region. If this new plasma is not heated as effectively, then one might expect that type II and III bursts pass through lower temperature plasma than for the standard corona. This should lead to more intense Langmuir waves and so radio emission, since the ratio of the electron beam speed to the background electron thermal speed will be larger.

Having a much flatter density profile during type IIs and IIIs than at other times provides an immediate explanation of the "ducting problem" for solar radio emission. Specifically the radio emission at a given frequency is actually generated further out (at larger $r - r_0$) than for the standard density model and so can be generated where (or at least closer to where) it is observed to originate, thus removing (or reducing) the need for ducting of the radiation from a lower height (where predicted by the standard density model) to the higher altitude where it is observed to come from.

Another consequence of having a much flatter density profile during the radio bursts than at other times is that the exciter speed of these sources is

underestimated: starting from Eq. (2.3) one can write

$$v_{ex} = \frac{1}{f}\frac{df}{dt} \times -\frac{(r - r_0)}{\alpha} \tag{2.13}$$

Thus for the same f, df/dt, and $(r - r_0)$, if α is smaller then v_{ex} is larger. In our case α is smaller and $(r - r_0)$ larger so v_{ex} is larger because of both factors. Using the median values above for the two sets of samples in Figure 2.6 yields a factor of 2.4 increase for v_{ex} via Eq. (2.13). This suggests exciter speeds a factor of 2.4 larger for the density profiles believed appropriate when the radio bursts are produced, making the standard estimate of $0.3c$ for the exciter speed become $0.7c - 0.8c$ and so relativistic.

Future analyses that image the locations of burst sources as functions of frequency and time [*McCauley et al.*, 2017; *Mann et al.*, 2018; *McCauley et al.*, 2018], in conjunction with spectroscopic or white-light observations of density profiles [*Zucca et al.*, 2014; *Mann et al.*, 2018; *Zucca et al.*, 2018] and this paper's theory should permit separation of the roles of α, v_{ex}, and ducting in determining the observed source locations, motion, and physics.

2.6 Conclusions

We presented strong evidence that the Offset Power Law (OPL) model applies very well to the radial electron density profile $n_e(r)$ of the Sun's corona and solar wind. This model, $n_e(r) = C(r - r_0)^{-\alpha}$, represents radial outflow from r_0 that conserves electron number and that may be accelerated or heated (thus changing the power law index α). Unlike commonly used empirical models it has physical significance and support, and the parameters r_0 and α may be used to predict measurable properties of the solar wind, namely its origin and velocity profile. The OPL model specifically fits very well multiple sets of published white light, spectroscopic, and radio-derived density profiles, in all but one case much better than the *Saito et al.* [1977] and Baumbach-Allen models. The non-radio fits yield a $r_0 = (1.02 \pm 0.06)R_S$ and $\langle\alpha\rangle = 2.4 \pm 0.2$. As discussed, r_0 close to $1R_S$ and $\alpha > 2$ are consistent with plasma originating at low altitudes near the chromosphere and an accelerating solar wind whose speed profile is comparable to the nominal Parker solar wind model. We note that electron density profiles derived from radio bursts are on average flatter, best fitted with $\alpha < 2$. We interpret this in terms of many radio bursts not travelling through the steeper density profile of the relatively quiescent corona; instead prior to flares or CMEs enhanced ejection of plasma from the host

active region increases the coronal density at larger heights and flattens the density profile. These changes lead to larger source heights for the same radio frequency, reducing the need to appeal to ducting and implying underestimation of the exciter speeds of type III bursts.

	Offset power law fit			Baumbach-Allen Fit		
Data	α	C	χ^2	a_6	a_{16}	χ^2_r
Guhathakurta et al.(inner)	3.2	1.15×10^5	0.24	8.66×10^6	2.32×10^8	0.55
Guhathakurta et al. (Outer)	2.18	1.63×10^5	0.04	9.62×10^6	0	43
Esser et al.	2.72	2.17×10^5	0.23	2.11×10^6	3.09×10^8	20.7.
Hayes et al. (equatorial)	2.56	3.11×10^6	0.01	2.51×10^8	3.45×10^3	46.8
Withbroe (equatorial)	2.25	6.52×10^5	0.17	3.49×10^7	6.00×10^8	20.7
Withbroe (polar max)	2.39	9.64×10^5	0.44	5.87×10^7	6.63×10^8	24.5
Avrett & Loeser	0.74	1.30×10^7	0.41			
Munro & Jackson	2.57	2.21×10^5	0.34	1.48×10^7	9.25×10^7	27.5
Kohl et al. (Inner)	3.13	4.07×10^5	0.08	2.56×10^7	1.14×10^9	0.375
Kohl et al. (Outer)	1.94	2.35×10^5	0.02	4.19×10^7	3.81×10^3	30.4
Strachan et al. (Inner)	1.82	2.61×10^6	0.24	2.64×10^8	4.49×10^3	29.5
Strachan et al. (Outer)	2.46	3.37×10^6	0.07	8.16×10^8	2.23×10^6	13.4
Magdalenic et al.	1.34	3.00×10^7	0.08	5.32×10^9	1.17×10^{10}	0.01
Ko et al.	1.83	2.44×10^6	0.06	8.90×10^7	2.89×10^8	0.39

Table 2.2: Comparisons of the 2-parameter OPL (α and C, with $r_0 = 1.0R_S$) and Baumbach-Allen models for the 14 datasets considered.

Data	A	α	r_0	χ^2_r
Guhathakurta et al. (inner)	1.43×10^5	3.96	0.90	0.21
Guhathakurta (outer)	1.67×10^5	2.19	0.99	0.04
Esser et al.	1.93×10^5	2.53	1.03	0.29
Hayes et al. (equatorial)	3.89×10^6	2.67	0.89	0
Withbroe (equatorial)	9.90×10^5	2.51	0.83	0.07
Withbroe (polar max)	1.20×10^6	2.55	0.93	0.27
Munro & Jackson	2.29×10^5	2.59	0.99	0.34
Kohl et al. (inner)	9.92×10^4	1.63	1.59	0.01
Kohl et al. (outer)	1.73×10^5	1.78	1.21	0.02
Strachan et al. (inner)	1.67×10^7	2.82	0	0.12
Strachan et al. (outer)	3.41×10^5	1.25	2.58	0
Magdalenic et al.	1.82×10^8	2.33	0.87	0.01
Ko	2.44×10^6	1.88	0.99	0.06

Table 2.3: Details of the 3-parameter OPL fits to the datasets.

Chapter 3

Electron-Langmuir wave resonance in three dimensions

[Published as J.C. Harding, Iver H. Cairns and Donald B. Melrose

Physics of Plasmas *27 (2) (2020]*

3.1 Abstract

In the one-dimensional (1D) treatment of Langmuir wave generation by a particle distribution via the kinetic beam instability, there is a one-to-one resonance between the electron speed v and the phase speed v_ϕ of the wave. The 1D condition for wave growth is $\partial f/\partial v > 0$ with $v = v_\phi$, and $f(v)$ evolves due to quasilinear relaxation towards a plateau distribution $\partial f/\partial v = 0$. We show here that none of these results apply in a 3D treatment of the problem. For a wave with wavevector $\mathbf{k}$ and phase speed v_ϕ, there is a many-to-one resonance with all electrons with $v > v_\phi$ moving obliquely to $\mathbf{k}$. Although growth requires a region with $\partial f/\partial v > 0$ below a peak in $f(v)$ the growth can be driven primarily by particles above the peak where $\partial f/\partial v < 0$, and growth can even occur at phase velocities v_ϕ where $\partial f/\partial v|_{v=v_\phi} < 0$. Resonance at $v \gg v_\phi$ favors diffusion of the particle distribution in angle, rather than plateau formation. These properties imply that intuition based on the 1D model can be seriously misleading, with far-reaching implications for modelling phenomena such as Type III solar radio bursts.

3.2 Introduction

The linear, quasilinear, and nonlinear interactions of electrons and Langmuir waves constitute one of the most basic and fundamental areas of plasma physics, with multiple applications in laboratory, space, and astrophysical plasmas. In general the first step is the excitation of Langmuir waves by an unstable electron distribution [*Ginzburg and Zheleznyakov*, 1958; *O'Neil and Malmberg*, 1968; *Malmberg and Wharton*, 1969; *Vedenov et al.*, 1961; *Drummond and Pines*, 1962; *Melrose*, 1986; *Cairns*, 1989]. The enhanced, nonthermal, population of Langmuir waves can then cause the electrons to diffuse, to lower energies due to the back-reaction to the wave growth and also in angle due to resonant wave-particle interactions, usually called "quasilinear relaxation" [*Vedenov et al.*, 1961; *Drummond and Pines*, 1962; *Grognard*, 1982; *Melrose*, 1986]. We assume the "weak beam" limit in which the background plasma determines the Langmuir wave dispersion. In this paper we are interested in the anisotropic part of the distribution and so we neglect damping due to the background isotropic population. This effect may be significant in the interplanetary medium for some regions of phase space, especially since solar wind electrons are well described by a kappa distribution [*Cairns et al.*, 2017; *Maksimovic et al.*, 1997],but not for the cases we investigate here. If the Langmuir waves achieve sufficient electric fields for their distributions in wavevector phase space, then nonlinear wave-wave processes can occur. Examples include the electrostatic decay process, other 3-wave processes that produce radio emission just above the electron plasma frequency f_p and near $2f_p$, often termed the "plasma emission", and modulational and other nonlinear self-focusing instabilities like the strong turbulence process of wave collapse [*Zakharov and Shabat*, 1972; *Papadopoulos et al.*, 1974; *Melrose*, 1982; *Grognard*, 1984; *Zakharov et al.*, 1985; *Melrose*, 1986; *Cairns and Fung*, 1988; *Papadopoulos et al.*, 1974; *Cairns and Robinson*, 1998; *Graham and Cairns*, 2013].

Starting in the late 1950s but extending to the present day, much of this theory was developed and applied to highly nonthermal solar radio bursts, particularly type III solar radio bursts. The basic model for type IIIs involves radiation produced near f_p and $2f_p$ by energetic electron beams and their coupled Langmuir waves [*Wild and McCready*, 1950; *Ginzburg and Zheleznyakov*, 1958; *Gurnett and Anderson*, 1976; *Lin et al.*, 1981; *Melrose*, 1982; *Goldman*, 1983; *Cairns*, 1984; *Cairns and Robinson*, 1998; *Robinson and Cairns*, 1998; *Reid and Ratcliffe*, 2014]. A picture of relatively narrow electron beams directed out from the Sun along magnetic field lines is suggested by an early

reconstruction of the electron distribution function near the Sun [*Grognard*, 1984]. Thus, a 1D model where electrons stream only along the magnetic field direction became widely accepted[*Sturrock*, 1964; *Grognard*, 1982]. However, subsequent observations of unstable electron beams have shown that the assumptions that justify a 1D approach do not always hold. For example, Type III electrons in the interplanetary medium (IPM) have a broad pitch-angle distribution, rather than being highly collimated [*Lin et al.*, 1981; *Ergun et al.*, 1998].

One of the major features of the 1D theory is a one-to-one resonance between electrons at speed v and waves with corresponding phase speed v_ϕ. In general Langmuir waves with a given wavevector $\mathbf{k}$ and frequency ω_L are resonant with electrons with velocities $\mathbf{v}$ such that $\omega_L(k) = \mathbf{k} \cdot \mathbf{v}$. This resonance condition, which may be written as $v_\phi = v \cos \Psi$, where Ψ is the angle between $\mathbf{k}$ and $\mathbf{v}$, allows resonance with $v_\phi \ll v$ at sufficiently large Ψ. We argue that such resonant interactions can dominate those with $v \approx v_\phi$, and lead to quite different results from those implied by the 1D model. In discussing the 3D case we assume axisymmetric distributions of waves and particles, and then expand both distributions and the quasilinear equations in Legendre polynomials [*Melrose and Stenhouse*, 1977; *Hoyng and Melrose*, 1977]. In exploring beam-driven wave growth, we consider several specific forms of the beam distribution $f(\mathbf{p})$ and based on these draw some general conclusions about the effects of resonant interactions between waves and particles in the 3D case. Although axisymmetric numerical models for the wave growth and the backreaction on the particles have been developed [*Appert et al.*, 1976; *Ziebell et al.*, 2008b,a, 2011], these models emphasize the effects for the resonant speed, $v \approx v_\phi$, rather than the resonances with $v \gg v_\phi$ of specific interest here.

In this paper we argue that long-held assumptions, based on the 1D model, regarding the nature of the beam instability are misleading, with potentially far-reaching implications. We use the simple model of a P_1 electron distribution, with specific analytical forms. Despite its simplicity, this model is instructive in that it clearly shows cases where electrons with velocities greater than the peak can excite Lanmguir waves with low v_ϕ. It allows us to examine in detail the conditions where this behaviour, completely at odds with the 1D theory, can occur. In the 1D picture, a plateau distribution forms in the asymptotic limit as the instability is exhausted [*Grognard*, 1982, 1984]. The short timescale on which plateau formation occurs implies that the beam is stopped almost immediately - the so-called Sturrock [*Sturrock*, 1964] dilemma - whereas type III beams are known to escape the corona and propagate through

the IPM. Several explanations have been offered for the observed perseverance of unstable electron beams through the solar corona and into IPM. Nonlinear processes could suppress the instability, for instance by re-distributing the Langmuir wave energy in phase space and other waves via 3-wave decay and coalescence processes or 4-wave modulational processes [*Papadopoulos et al.*, 1974; *Cairns and Robinson*, 1998; *Graham and Cairns*, 2013]. In addition, the corona is observed to be highly inhomogenous, with density clumps corresponding to bursty Langmuir waves [*Robinson et al.*, 1992]. Stochastic Growth Theory describes how this allows for a weak electron beam to persist even out to 1AU [*Cairns and Robinson*, 1998; *Robinson*, 1993]. Finally, the assumed fast saturation of the beam instability relies on the one-to-one resonance result from a 1D consideration. We argue that the 3D case allows an entirely different asymptotic state from plateau formation.

3.3 Theory

3.3.1 The quasilinear equations expanded in Legendre polynomials

The occupation number $N(\mathbf{k})$ of Langmuir waves evolves according to

$$\frac{dN(\mathbf{k})}{dt} = \alpha_L(\mathbf{k}) + \gamma_L(\mathbf{k})N(\mathbf{k}), \tag{3.1}$$

where α_L is the rate of spontaneous emission of waves and γ_L is the growth rate. Both J_L and γ_L are functions of the distribution $f(\mathbf{p})$ of electrons with momentum $\mathbf{p}$, normalised such that $\int d\mathbf{p}\ f(\mathbf{p}) = n_e$ is the number density of electrons, which obeys a quasilinear diffusion equation with the diffusion coefficients depending on $N(\mathbf{k})$.

We focus in this paper on the growth rate γ_L, defined such that waves grow for positive $\gamma_L > 0$ and waves damp for negative $\gamma_L < 0$. Assuming axisymmetry about the magnetic field (which is otherwise neglected), we write $f(\mathbf{p}) = f(p, \alpha)$ and $N(\mathbf{k}) = N(k, \theta)$, and expand in Legendre polynomials $P_l(\cos\alpha)$ and $P_l(\cos\theta)$, respectively. We also explicitly separate the thermal electron distribution $f_{\rm th}(p)$ from the beam component (with number densities $n_{\rm th}$ and n_b respectively), and assume that the thermal background is isotropic, with thermal speed V_e much less than the typical speed of the beam electrons.

The expansions give

$$f(p,\alpha) = f_{\rm th}(p) + \sum_{l=0}^{\infty} f_l(p) P_l(\cos\alpha), \tag{3.2}$$

$$N_{\rm L}(k,\theta) = \sum_{l=0}^{\infty} N_l(k) P_l(\cos\theta). \tag{3.3}$$

The electron distribution must satisfy $f(p,\alpha) > 0$ everywhere. The normalisation condition becomes

$$\int d\mathbf{p}\; f(\mathbf{p}) = 4\pi \int dp\; p^2 \left[f_0(p) + f_{\rm th}(p)\right] = n_b + n_{\rm th} = n_e, \tag{3.4}$$

such that the $l = 0$ term determines n_e, $n_{\rm th}$ and n_b.

We also expand $\alpha_L(k,\theta)$ and $\gamma_L(k,\theta)$ in Legendre polynomials. The quasi-linear equations then lead to a set of coupled equations for $N_l(k)$ and $f_l(p)$. Following *Melrose and Stenhouse* [1977] and *Hoyng and Melrose* [1977], the evolution of the waves is described by

$$\frac{dN_l(k)}{dt} = \alpha_l(k) + \frac{2l+1}{2} \sum_{m,n} a_{lmn} \gamma_m(k) N_n(k), \tag{3.5}$$

where a_{lmn} is the x-integral of the product of $P_l(x)P_m(x)P_n(x)$ and is nonzero only when the triangle inequality (i.e, $|l-n| \le m \le l+n$) is satisfied. The spontaneous emission α_l and growth term γ_l components are given by

$$\alpha_l(k) = \frac{2\pi^2 e^2 \omega_p^2}{\varepsilon_0 k^3} \int_{p_\phi}^{\infty} dp \frac{p^2}{v} f_l(p) P_l(\cos\chi_0), \tag{3.6}$$

$$\gamma_l(k) = -\frac{2\pi^2 e^2 \omega_p^2}{\epsilon_0 k^3} \Bigg\{ m^2 \gamma_\phi^2 f_l(p_\phi) + \int_{p_\phi}^{\infty} dp \frac{2p}{c^2} f_l(p) P_l(\cos\chi_0) + \\ - \frac{m^2}{p_\phi^2} \int_{p_\phi}^{\infty} dp\; p f_l(p) \cos\chi_0 P_l'(\cos\chi_0) \Bigg\}, \tag{3.7}$$

respectively, with $p_\phi = m\gamma_\phi v_\phi$, $\gamma_\phi = (1 - v_\phi^2/c^2)^{-1/2}$, and $\cos\chi_0 = v_\phi/v$. We are primarily interested in waves with $v_\phi \gg V_e$, which allows us to ignore the background contribution to the isotropic ($l = 0$) terms as $f_{th}(p) \ll f_0(p)$.

The second term in (3.7) includes relativistic factors, and in the nonrelativistic limit (3.7) becomes

$$\gamma_l(k) = \frac{2\pi^2 e^2 p_\phi}{\epsilon_0 k} \Bigg\{ - p_\phi f_l(p_\phi) + \int_{p_\phi}^{\infty} dp\; f_l(p) P_l'(\cos\chi_0) \Bigg\}. \tag{3.8}$$

The 3D resonance condition can be seen qualitatively in (3.8) in the integral term inside the brackets - each $\gamma_l(k)$ depends on the values of f_l at $p \geq p_\phi$, not simply at $p = p_\phi$. The full effect of this difference requires a detailed consideration of more specific forms of $f_l(p)$.

3.3.2 P_1 distributions

Let us consider a P_1 electron distribution - that is, $f(p,\alpha) = f_0(p) + f_1(p)\cos\alpha$. This is a weakly anisotropic distribution which is a possible first approximation to observed type III beams in the IPM [*Ergun et al.*, 1998].

The distribution function $f(p,\alpha)$ cannot be negative, which requires $f_1(p) \leq f_0(p)$ for a P_1 distribution. The simplest form, which can easily be generalised, is

$$f(p,\alpha) = f_0(p)(1+\cos\alpha), \tag{3.9}$$

corresponding to $f_1 = f_0$. We use this simple model, with specific choices of $f_0(p)$ to infer some general features of the 3D case. For such a P_1 particle distribution, one has

$$\gamma_0(k) = -\frac{2\pi^2 e^2 p_\phi^2}{\epsilon_0 k} f_0(p_\phi), \tag{3.10}$$

$$\gamma_1(k) = \frac{2\pi^2 e^2 p_\phi}{\epsilon_0 k}\left\{-p_\phi\, f_1(p_\phi) + \int_{p_\phi}^{\infty} dp\; f_1(p)\right\}. \tag{3.11}$$

The isotropic term in the expansion of $f(p,\alpha)$, $f_0(p)$, contains the number of particles, and must be positive. Therefore, $\gamma_0(k)$ is negative everywhere and cannot contribute to the growth of waves. This means that if the Langmuir waves grow, then γ_1 must be sufficiently positive to satisfy

$$\gamma_0(k) + \gamma_1(k)\cos\theta > 0. \tag{3.12}$$

An essential requirement for wave growth is thus $\gamma_1 > 0$. Consider the part of (3.11) in the brackets - the sign of the following term determines the sign of γ_1,

$$-p_\phi f_1(p_\phi) + \int_{p_\phi}^{\infty} dp\; f_1(p). \tag{3.13}$$

The second part of Eq (3.11), involving the integral, depends on electrons with $p \geq p_\phi$. This is clearly different from the 1D case which is driven only by electrons with $p = p_\phi$.

Double power law

We assume a P_1 particle distribution, as in Eq (3.9), with a peaked double power law form

$$f_0(p) = \begin{cases} C_1 p^b & p < p_1, \\ C_2 p^{-a} & p > p_1, \end{cases} \tag{3.14}$$

where C_1 and C_2 are such that f_1 is continuous at p_1 (Figures 3.1 and 3.2).

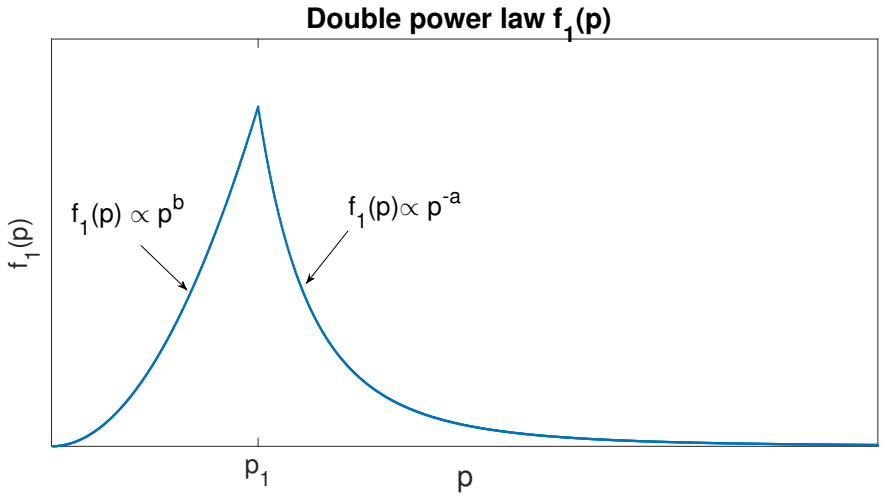

Figure 3.1: The peaked double power law form of $f_0(p)$ in Eq (3.14)

.

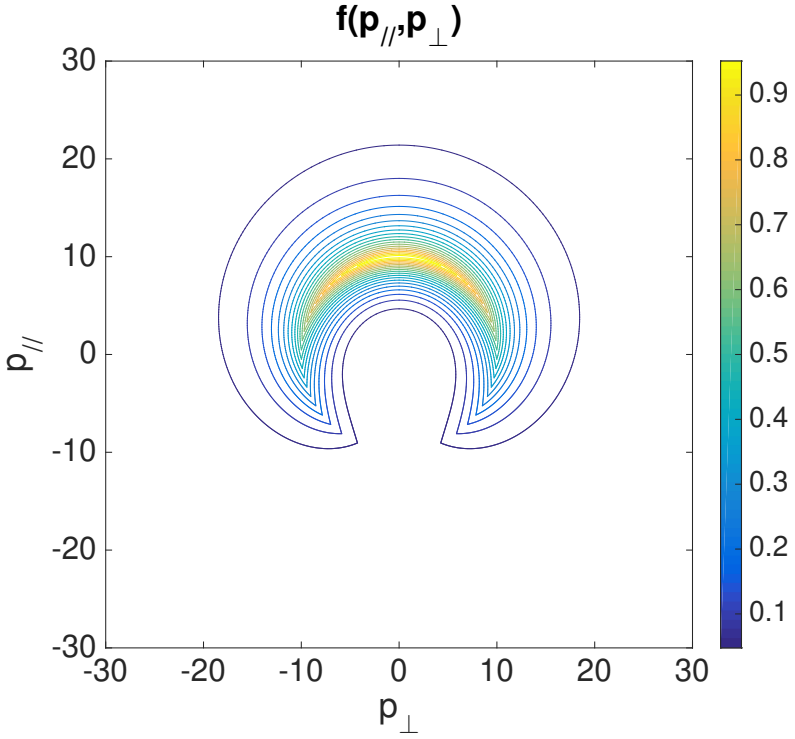

Figure 3.2: Countour plot of $f(p_{\|}, p_{\perp})$ normalised to the maximum at $(p_1, 0)$ in the case of a P_1 distribution described in Eq (3.9) with f_0 given by the peaked double power law of Eq (3.14).

From Eqs (3.9) - (3.14), one finds that $\gamma_0 + \gamma_1 = \gamma_L(k, \theta = 0) > 0$ when

$$\left(\frac{p_\phi}{p_1}\right)^{b+1} < \frac{a+b}{(a-1)(2b+1)}. \tag{3.15}$$

However, this constraint does not directly show us which electrons are contributing to the wave growth. We identify the electrons that contribute to growth as follows.

First we expand γ_1 for the double power law model (3.14) and separate it into the two components, as in Figure 3.3a. We also introduce a width Δp_1 in order to separate electrons with momenta close to the peak in the double

power law. For $p_\phi < p_1$, one has

$$\gamma_1(k) = \frac{2\pi^2 e^2 p_\phi}{\epsilon_0 k}\left\{-C_1 p_\phi^{b+1} + C_1\int_{p_\phi}^{p_1} dp\, p^b - C_2\int_{p_1}^{\infty} dp\, p^{-a}\right\}$$
$$\propto \frac{p_\phi}{k}\Bigg\{ - C_1 p_\phi^{b+1} + C_1\int_{p_\phi}^{p_1-\Delta p_1} dp\, p^b + C_1\int_{p_1-\Delta p_1}^{p_1} dp\, p^b$$
$$+ C_2\int_{p_1}^{p_1+\Delta p_1} dp\, p^{-a} + C_2\int_{p_1+\Delta p_1}^{\infty} dp\, p^{-a}\Bigg\}, \qquad (3.16)$$

where the terms proportional to C_1 and C_2 are separated into contributions from below ($p_\phi < p_1$) and above ($p_\phi > p_1$) the peak in $f(p)$ at p_1. The five terms in Eq (3.16) are denoted respectively

$$\gamma_1(k) = \frac{2\pi^2 e^2 p_\phi}{\epsilon_0 k}\left\{-\gamma_{\rm iso} + \gamma_{a1} + \gamma_{a2} + \gamma_{a3} + \gamma_{a4}\right\}. \qquad (3.17)$$

The relative contributions of each range of the electron distribution to the overall growth rate γ_1 define the corresponding terms γ_{iso} and $\gamma_{a1} - \gamma_{a4}$: γ_{a1} is the component due to electrons with $p_\phi < p < p_1 - \Delta p_1$ (red in Figure 3.3), γ_{a2} the electrons near the low-velocity side of the peak (green), γ_{a3} the high-velocity side (black), and γ_{a4} the high velocity tail of the electron distribution (yellow).

A 1D consideration of this problem would predict that the terms γ_{a2}, γ_{a3} and γ_{a4} would all only damp the waves at $p_\phi < p_1$. However, we clearly show in Figure 3.3b and 3.3c that they contribute to wave growth and that, depending on the power-law indices a and b, the high velocity tail of the electron distribution where $\partial f/\partial v < 0$ can even dominate the growth term. We next quantify the relative contributions of each of these regions to growth.

One finds analytically that $\gamma_{a2} > \gamma_{a1}$ for all p_ϕ when

$$a > \frac{\ln\frac{1}{2}}{\ln\left(1 - \Delta p_1/p_1\right)} - 1. \qquad (3.18)$$

That is, electrons with $v > v_\phi$ near the peak contribute more towards wave growth than electrons with v closer to the 1D resonance, v_ϕ. To make this discussion more concrete, we consider $\Delta p_1/p_1 = 0.1$. Then (3.18) gives $a > 5.58$.

Similarly, $\gamma_{a3} > \gamma_{a4}$ for all p_ϕ when

$$b > 1 - \frac{\ln\frac{1}{2}}{\ln\left(1 + \Delta p_1/p_1\right)} \qquad (3.19)$$

This implies that high velocity electrons near the peak contribute to the growth of the waves more than those with higher speeds. For $\Delta p_1/p_1 = 0.1$, Eq (3.19) becomes $b > 8.27$. We need $b > 3$ in order for the distribution function to be integrable.

In Figure 3.3 we see that for an intermediate high-velocity power law slope, i.e. $3 < b < 8.27$, the contribution to a positive γ_1 from the high-velocity electrons actually dominates. That is, in the region $p_\phi < p_1$ (below the peak), γ_{a4} is the dominant contributor to γ_1. Below, we present an even more dramatic example of this region being important to wave growth, contrary to previous thinking based on the 1D model.

Figure 3.4 shows γ_1 and its components for a similar case to Figure 3.3 but with dominant contributions to the wave growth from the electrons near the peak of the distribution, both on the lower and higher speed sides. The growth occurs at $p_\phi < p_\parallel$ but is not primarily due to the locally resonant electrons, instead having significant contributions from the γ_{a2}, γ_{a3}, and γ_{a4} terms. Indeed, where $\gamma_L > 0$ the γ_{a1} term for electrons with $p_\parallel < p_1 - \Delta p_1$ is always smaller than the γ_{a3} amd γ_{a4} terms for higher $p_\parallel$ electrons. Further, the primary reason the instability turns off is that $\gamma_{\rm iso}$ increases rapidly for $p_\phi > p_1 - \Delta p_1$, i.e. near the peak. It is not, as previously thought, just due to $\partial f/\partial v$ decreasing.

A 1D quasilinear-like model was used in *Voshchepynets et al.* [2015], where random density fluctuations in the background plasma induced a resonant broadening effect. This effect is interesting and no doubt enhances the effect found here, which occurred with for a homogeneous 3Dplasma with a P_1 distribution rather than in a 1D inhomogeneous plasma

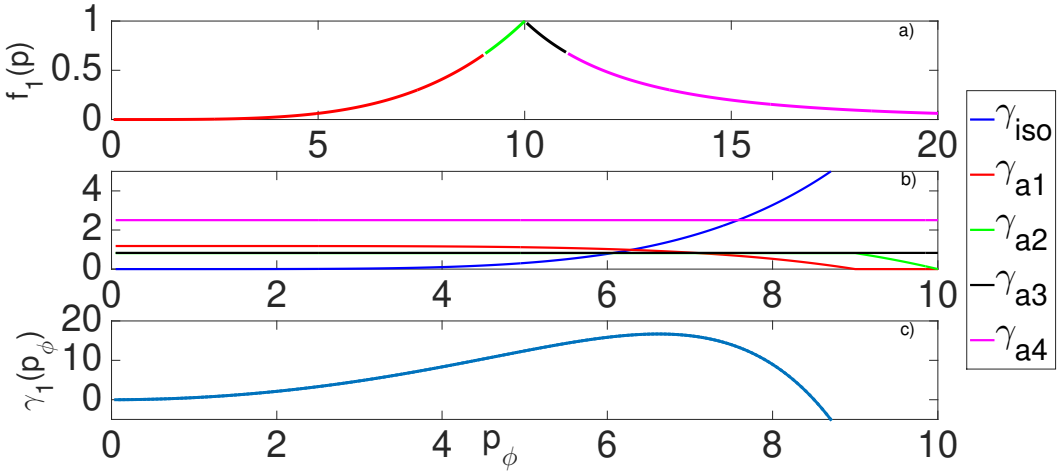

Figure 3.3: (a) Double power law $f_1(p)$, (b) the contributions $\gamma_{\rm iso}$ and $\gamma_{a1} - \gamma_{a4}$ to γ_1, and (c) $\gamma_1(p_\phi)$ for $a = 4$ and $b = 6$. It is clear that the high speed electrons and terms $\gamma_{a2} - \gamma_{a4}$ contribute most to the wave growth.

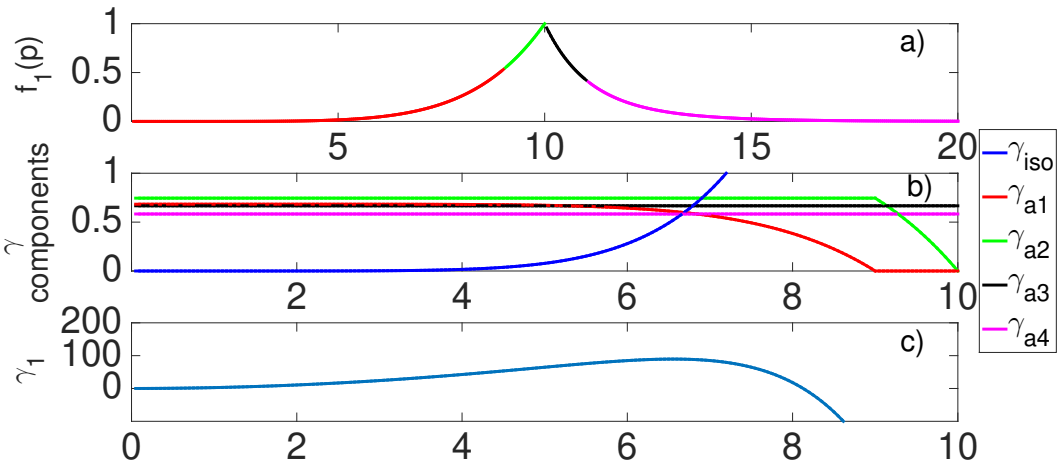

Figure 3.4: As for Figure 3.3 but with $a = 9$ and $b = 6$. Now the electrons near the peak on both the low and high velocity sides contribute significantly to the wave growth.

Shifted Maxwellian

In order to clearly establish that the results in the previous section are a result of the many-to-one resonance of the 3D axisymmetric system, and to exclude the

influence of the sharp non-differentiable point at p_1 and the artificial double power law distribution, we now consider a shifted Maxwellian for $f_1(p)$. If $f_0 = f_1$ is Maxwellian peaked at $p = p_b$, i.e. $f_0 = f_1 \propto \exp\left[-(p-p_b)^2/p_e^2\right]$ as in Figure 3.5, then the factor $\gamma_1(k)$ is given by

$$\gamma_1(k) \propto \frac{p_\phi}{k}\left\{ -p_\phi \exp\left[-\frac{(p_\phi - p_b)^2}{p_e^2}\right] + \frac{\sqrt{\pi}}{2}\left[1 + \mathrm{erf}\left(\frac{p_b - p}{p_e}\right)\right]\right\} \tag{3.20}$$

The resulting growth rate shows similar features to the previous example. Electrons on both sides of the peak contribute significantly to the positive wave growth, as demonstrated by the large and equal contributions from γ_{a2} and γ_{a3}. The high velocity electrons which contribute to both γ_{a3} and γ_{a4} are important in the growth of waves. The wave growth term becomes negative closer to the peak (in this case around $p_\phi = 8.8 m_e V_e$).

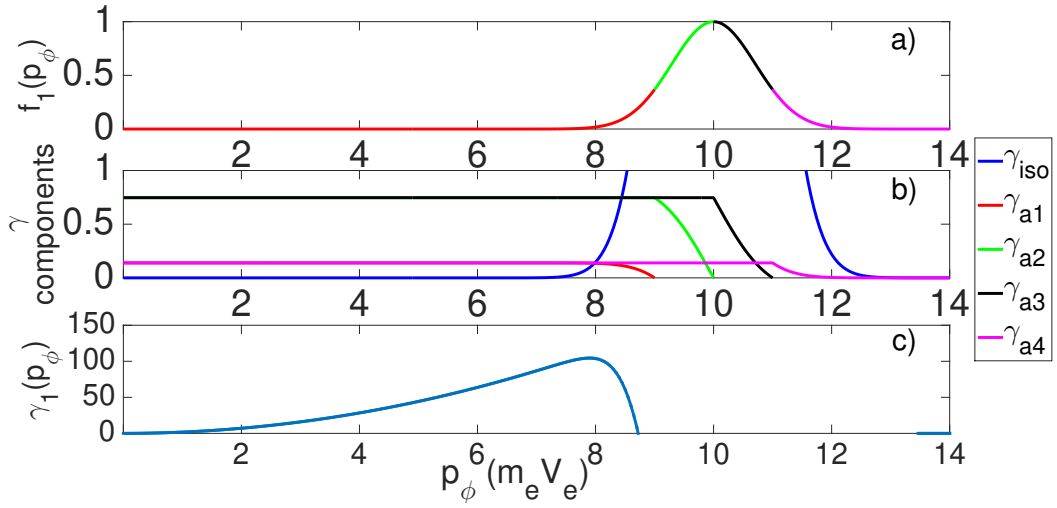

Figure 3.5: The growth rate and its components for a Maxwellian distribution centred at $p_b = 10 m_e V_e$, with $\Delta p_1 = 0.1 p_b$ as for Figure 3.

More general choices of distribution function

The specific choice of a P_1 distribution with $f_1(p) = f_0(p)$ corresponds to a broad angular distribution $\propto (1 + \cos\alpha)$ that is the same for all p. Actual distributions observed in the IPM are more beamed, and this can be modeled by replacing $\cos\alpha$ by $\cos\alpha^{2N+1}$, with $N = 2$ for example. It is straightforward

to repeat the foregoing analysis, which corresponds to $N = 0$, to show that the qualitative features identified for the P_1-case also apply for $N > 0$. One may include the p-dependence of the beaming in a P_1 distribution by assuming that $r(p) = f_1(p)/f_0(p) \leq 1$ is an increasing function of p. These generalizations of the model leads to a form $\propto f_0(p)[1 + r(p)\cos\alpha^{2N+1}\alpha]$. In principle, choosing best fits of $f_0(p)$, $r(p)$ and N to observed distributions will allow discussion of wave growth for more realistic distributions. However, we do not discuss this further in the present paper.

3.3.3 Growth in a region of negative slope

So far we have demonstrated that in 3D high velocity electrons in regions of phase space where $\partial f/\partial v_\parallel < 0$ can contribute to the growth of waves. However, wave growth still occurs at lower speeds where $\partial f/\partial p_\parallel > 0$. Even this long-held result from the 1D consideration of the plasma emission problem does not hold in 3D. To demonstrate this, consider a different P_1 model that allows for a flatter power law in a finite region, before tailing off in accordance with normalisability conditions. Specifically, consider

$$f_1(p) = \begin{cases} Ap^a & p < p_1 \\ Bp^{-b} & p_1 < p < p_2 \\ Cp^{-c} & p > p_2 \end{cases} \tag{3.21}$$

with $a > 1$, $c > 3$ and continuity at p_1 and p_2.

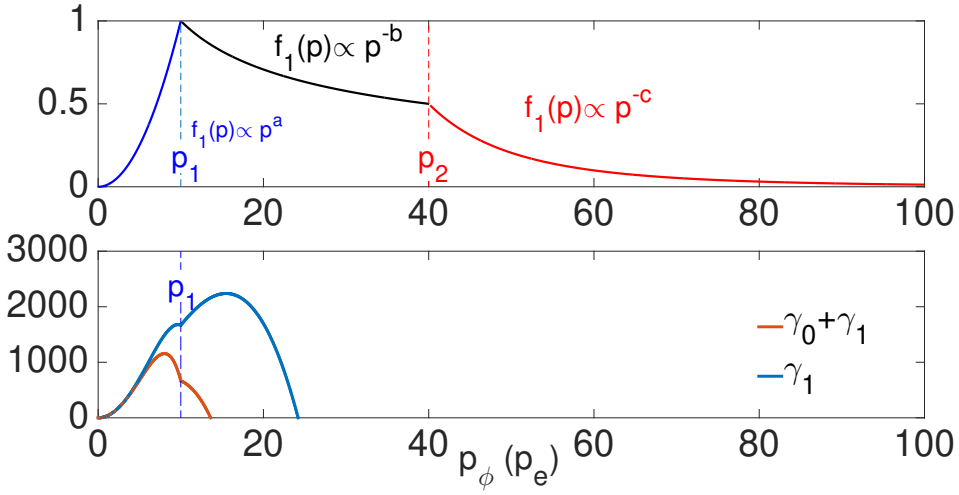

Figure 3.6: Triple power law with a flatter section in the central region $10 = p_1 < p < p_2 = 40$, compared with γ_1 for the triple power law given by Eq (3.21), with $a = 2$, $b = 0.5$ and $c = 4$ and $\gamma_0 + \gamma_1$.

In this case, $\gamma_0 + \gamma_1$ is positive in the region $p_1 < p_\phi < p_2$ when

$$p_\phi < p_2 \left(\frac{c-b}{(3-2b)(c-1)} \right)^{\frac{1}{1-b}} . \tag{3.22}$$

If we choose $b = 1/2$ and $c = 4$, then (3.22) becomes $p_\phi < 0.34 p_2$. Figure 3.6 confirms this for $p_2 = 40$, showing positive γ_1 in the region with negative slope $\partial f/\partial v_\parallel$, where $p_1 = 10 \leq p_\phi \leq 13.61$. Figure 3.6 shows that γ_1 is sufficiently positive to give positive γ_L, at least for angles where $\cos\theta \approx 1$.

The modest but real region in this example, where $\gamma_L > 0$ but $\partial f/\partial v < 0$, further shows that the conventions of Langmuir wave growth based on the 1D model must be re-evaluated.

3.4 Discussion and Summary

The one-dimensional (1D) model of the kinetic beam instability driving Langmuir waves and radio emission, particularly in Type III radio bursts, is still commonly used and relied upon for numerical and theoretical development of the plasma emission problem [*Li et al.*, 2008; *Li and Cairns*, 2014; *Ratcliffe et al.*, 2014]. Figures 3.3-3.6 and the associated theory show that the growth of Langmuir waves in three dimensions from an unstable electron distribution

occurs in a substantially different way than in the 1D model. The resonance between the velocity of the electrons and the wavenumber of the waves is no longer one-to-one, and the simple consideration of the gradient of the distribution is no longer enough to determine whether the waves will grow or be damped. The cases we describe here require a re-think of the electron-Langmuir wave resonance in 3D. The effects we demonstrate for a P_1 case are expected to apply to more anisotropic particle distributions, such as the electron beams responsible for Type III radio bursts [*Lin et al.*, 1981] with additional higher order variations of γ_L in p_ϕ and $\cos\theta$.

We have shown that resonant interactions of waves at v_ϕ can be dominated by particles with $v \gg v_\phi$, and it can be shown due to the symmetry of the electron-Langmuir wave interaction in the resonance condition that the same result applies to the diffusion of particles due to the waves. That is, a particle with speed v interacts with and diffuses due to waves with $v_\phi \gg v$ over a wide range of wavevector directions. One interpretation of this is that this interaction occurs at large Ψ (recall the resonance condition $v_\phi = v\cos\Psi$). This would imply that diffusion at $v \gg v_\phi$ primarily changes the pitch angle α rather than the momentum p. That is, we should see electrons significantly diffusing in angle near and above the peak of the unstable distribution, rather than the plateau formation implied by the 1D picture. A preliminary look at two-dimensional electron distributions in the IPM, e.g. from *Ergun et al.* [1998], shows distributions broad in angle. Future work will explore these and more general "beam" distributions in terms of their instability to Langmuir wave growth and their evolution and relaxation due to the wave growth.

Chapter 4

A numerical method for modelling the 3D axisymmetric Electron - Langmuir wave interactions

4.1 Abstract

The kinetic beam instability that drives plasma emission is modelled in a 3D, relativistically correct, axisymmetric way using Legendre polynomials and calculated numerically, using implicit finite difference schemes and a block-tridiagonal solving algorithm for higher order Legendre expansions. We describe the numerical model and the initial tests in detail, and apply the model to distributions discussed in the previous chapter. The numerical model reproduces known analytic results such as the stability of the thermal level of waves for a Maxwellian electron distribution and shows new results such as the evolution in time of waves for an isotropic gap distribution. This chapter's new numerical model is then used to probe the electron-Langmuir wave interaction and quasilinear relaxation in a new light. We consider electron distributions that were discussed analytically in Chapter 3 here, modelling electron diffusion in the presence of a fixed Langmuir wave population and demonstrating electron diffusion in both angle and speed for the first time. As an extension to the work done in Chapter 3, we also consider electron distributions of the form $f(p,\alpha) = f_0(p)\left[1 + r(p)\cos^{2N+1}\alpha\right]$, in terms of the relative contributions of electrons in different parts of the distribution, to show that the 3D resonance effects persist to higher-order and more realistic particle distributions.

4.2 Introduction

Electron beams coming from the Sun often produce radio emission, most notably Type III solar radio bursts. The underlying instability involves energy transfer from the electron beam to Langmuir waves in the background plasma, which can be converted to radio waves via nonlinear processes. This process has long been modelled, both analytically and numerically, in a 1D or pseudo-1D way [*Melrose*, 1986; *Grognard*, 1982, 1984; *Li et al.*, 2002, 2008; *Mel'Nik et al.*, 1999; *Ratcliffe et al.*, 2014]. While the electron beam is directed along open magnetic field lines from the photosphere, beams which have been measured to date [*Lin et al.*, 1982; *Ergun et al.*, 1998] have a significant angular breadth about the magnetic field direction. 3D effects from oblique waves should therefore be expected, and analytically it can be shown that several of the foundational conditions for Langmuir wave growth found in the 1D formalisms do not strictly hold in three dimensions, as in Chapter 3 and *Harding et al.* [2020].

Using the axisymmetry of the system of the electron beam travelling along a magnetic field line, the quasilinear equations can be expanded in Legendre polynomials [*Hoyng and Melrose*, 1977; *Melrose and Stenhouse*, 1977], as shown in Chapter 1. This technique leads to a new consideration of the resonance between the fast electrons and Langmuir waves, such as that conducted in Chapter 3. For a full exploration of the 3D implications of the electron-Langmuir wave interaction a numerical scheme must be developed. This chapter presents a numerical scheme for solving these quasilinear equations, with tests of this scheme against known analytical results and some early results exploring the uniquely 3D effects we expect from the theory. Extensions and further development of the analytical analysis in Chapter 3 are also presented, supplemented with numerical calculations using the new code.

4.3 Numerical scheme and code

4.3.1 Dimensionless scheme

To efficiently describe the quasilinear system, the following dimensionless system is used. This is a three-dimensional extension of that used in, for example, *Grognard* [1982] and *Li et al.* [2002]. The 0 subscript below indicates the value of the variable at the first grid-point in phase space - i.e. at $(\mathbf{r}_0, \mathbf{v}_0)$.

$$
\begin{aligned}
p &= m_e\gamma(v)v & V_e^2 &= \frac{k_B T_e}{m_e} \\
p_\phi &= m_e\gamma(v_\phi)v_\phi & v_\phi &= \frac{\omega_p}{k} \\
k_D &= \frac{\omega_p}{V_e} & \omega_p^2 &= \frac{ne^2}{\epsilon_0 m_e} \\
p' &= \frac{p}{p_{D0}} & p_D &= m_e V_e \\
t' &= \frac{t}{t_{D0}} & t_D &= \frac{n_e}{\pi\omega_p k_D^3} \\
z' &= \frac{z}{z_{D0}} & z_D &= \frac{n_e}{\pi k_D^4} \\
N_l' &= \frac{N_l}{N_{D0}} & N_D &= \frac{k_B T_e}{\hbar\omega_p} \\
f' &= \frac{f}{f_{D0}} & f_D &= \frac{1}{2\pi m_e^3\omega_p^3} k_D^6 \\
T_e' &= \frac{T_e}{T_{e0}} & n_e' &= \frac{n_e}{n_{e0}} \\
\omega_L' &= \frac{\omega_L}{\omega_{p0}} & p' &= \gamma v.
\end{aligned} \tag{4.1}
$$

Hereafter, the primes are dropped in dimensionless equations.

The dimensionless scheme (4.1) is used to express the Legendre expansion of the two coupled quasilinear equations first introduced in Chapter 1 as (1.26 - 1.30) and (1.32 - 1.41). The dimensionless equations are written below in matrix form, recalling the notation used in (1.25).

The Langmuir wave equation in dimensionless form was given in Chapter 1 in Equation 1.26. This assumed $\omega_L = \omega_p$. Including the full number density and electron temperature dependence of ω_L, the dimensionless Langmuir wave equation is

$$
\begin{aligned}
&\left\{\frac{\partial}{\partial t} + \frac{1}{\omega_L(k)}\boldsymbol{H}\left[3v_e^2\frac{\partial}{\partial z} - \left(\frac{1}{2}\frac{\partial n_0}{\partial z} + \frac{3}{2}\frac{\partial T_e}{\partial z}\right)\frac{\partial}{\partial k}\right]\right. \\
&\left. + \frac{1}{k\omega_L(k)}\left(\frac{1}{2}\frac{\partial n_0}{\partial z} + \frac{3}{2}\frac{\partial T_e}{\partial z}\right)\boldsymbol{J}\right\}\boldsymbol{N} = \boldsymbol{\sigma} - \boldsymbol{\Gamma}\boldsymbol{N},
\end{aligned} \tag{4.2}
$$

where

$$\boldsymbol{\sigma}_n = \frac{1}{n_e}\frac{\omega_L(k)^3}{k^3}\int_{p_\phi(k)}^{\infty} dp \frac{p^2}{v} P_n\left(\frac{\omega_L(k)}{kv}\right) f_n(p), \tag{4.3}$$

$$\begin{aligned}\boldsymbol{\Gamma}_{nl} = \frac{1}{n_e}\frac{\omega_L(k)^4}{k^3} &\sum_{s=|n-l|}^{\min\{|n-l|,M\}} \frac{2n+1}{2} A_{nsl}\left\{\frac{p_\phi(k)^2}{v_\phi(k)^2} f_s(p_\phi)\right. \\ &+ \int_{p_\phi}^{\infty} dp \frac{2p}{c^2} P_s\left(\frac{\omega_L(k)}{kv}\right) f_s(p) \\ &\left. + \left[\left(\frac{\omega_L(k)}{kc}\right)^2 - 1\right]\int_{p_\phi(k)}^{\infty} dp \frac{p}{vv_\phi} P_s\left(\frac{\omega_p}{kv}\right) f_s(p)\right\}.\end{aligned} \tag{4.4}$$

The term $\partial \boldsymbol{N}/\partial z$ is the advection term, and the term $\partial \boldsymbol{N}/\partial k$ is the refraction term. The terms $\boldsymbol{H}$ and $\boldsymbol{J}$ come from the orthogonality relation of Legendre polynomials and are given by

$$H_{nl} = \frac{n}{2n-1}\delta_{n,l+1} + \frac{n+1}{2n+3}\delta_{n,l-1} \tag{4.5}$$

$$J_{nl} = \frac{l(l+1)}{2l+1}\left(\delta_{n,l+1} - \delta_{n,l-1}\right) \tag{4.6}$$

The particle equation (Equation 1.32) in dimensionless form is

$$\left(\frac{\partial}{\partial t} + v\boldsymbol{H}\frac{\partial}{\partial z}\right)\boldsymbol{f} = \frac{1}{4\pi^2 p^2}\left\{\frac{\partial}{\partial p}\boldsymbol{P}\frac{\partial}{\partial p} + \frac{\partial}{\partial p}\boldsymbol{Q} + \boldsymbol{R}\frac{\partial}{\partial p} + \boldsymbol{S}\right\}\boldsymbol{f}, \tag{4.7}$$

where

$$P_{nl} = \frac{1}{n_e}\frac{p^2}{v^3}\sum_{s=|n-l|}^{\min\{M,n+l\}} \frac{2n+1}{2} A_{nsl}\int_{\omega_L/v}^{\infty} \frac{dk}{k}\omega_L(k)^5 N_s(k) P_s(\omega_L/kv), \tag{4.8}$$

$$\begin{aligned}Q_{nl} = {} & p^2 A_p \delta_{nl} \\ & - \frac{1}{n_e'}\frac{p}{v^3}\sum_{s=|n-l|}^{n+1}\frac{2n+1}{2s(s+1)}\lambda_{nsl}^{(1)}\int_{\omega_L(k)/v}^{\infty}\omega_L(k)^5\frac{dk}{k}\left[\left(\frac{kv}{\omega_L(k)}\right)^2 - 1\right]^{1/2} \\ & \times N_s(k) P_s^1\left(\frac{\omega_L(k)}{kv}\right),\end{aligned} \tag{4.9}$$

$$\begin{aligned}R_{nl} = \frac{1}{n_e}\frac{p}{v^3}&\sum_{s=|n-l|}^{\min\{M,n+l\}}\frac{2n+1}{2s(s+1)}\lambda_{lsn}^{(1)} A_{nsl}\int_{\omega_L(k)/v}^{\infty}\omega_L(k)^5\frac{dk}{k}\left[\left(\frac{kv}{\omega_L(k)}\right)^2 - 1\right]^{1/2} \\ & \times N_s(k) P_s^1\left(\frac{\omega_L(k)}{kv}\right),\end{aligned} \tag{4.10}$$

$$S_{nl} = -\frac{1}{n_e} \sum_{s=|n-l|}^{\min\{M,n+l\}} \frac{2n+1}{2} A_{nsl} \int_{\omega_L(k)/v}^{\infty} \frac{dk}{k} \frac{1}{2} \omega_L(k)^5 \left[\left(\frac{kv}{\omega_L(k)} \right)^2 - 1 \right] \times N_s(k) \left[\lambda_{snl}^{(1)} P_s \left(\frac{\omega_L(k)}{kv} \right) + \frac{(s-2)!}{(s+2)!} \lambda_{snl}^{(2)} P_s^2 \left(\frac{\omega_L(k)}{kv} \right) \right], \tag{4.11}$$

$$A_p = \frac{n_e}{v^2} \ln \left(\frac{v}{\omega_L(\mathbf{v})} \right) + \frac{3n_e(\mathbf{r})}{v^2} \left[1 - \left(\frac{\omega_L(\mathbf{v})}{v} \right)^2 \right] + \frac{9n_e(\mathbf{r})}{4v^2} \left[1 - \left(\frac{\omega_L(\mathbf{v})}{v} \right)^4 \right]. \tag{4.12}$$

In Equation 4.7, the term $\partial/\partial z$ determines advection of particles, $\boldsymbol{P}$ is a classic diffusion term in momentum, and A_p is the result of the backreaction on the particles from spontaneously emitted Langmuir waves.

These dimensionless quasilinear equations use the full expression for the Langmuir wave frequency, $\omega_L(k)$, which is a generalisation. Most often, the approximation $\omega_L \approx \omega_p$ is used; however this approximation simplifies the expression for A_p (Equation 4.12) and does not include the derivative of the temperature profile, $\partial T_e/\partial z$, in the wave equation, simplifying the refraction term to just $\propto (\partial n_0/\partial z)(\partial/\partial k)$. Furthermore, factors of $\omega_L^5(k)$ in the integrands in several places in Equations (4.8-4.12) could well be significantly different from ω_p^5 unless k is very small.

4.3.2 Finite differences

To numerically approximate Equations (4.2) and (4.7) the following finite differencing scheme is employed. The system uses explicit first order forward finite difference in time, backwards explicit discretization is implemented for the v-advection term and an implicit second-order central finite difference scheme is used for the diffusion. We take discrete values of time (t), position (z), momentum (p), and wavenumber (k) with time index n, position index i and a joint momentum and wavenumber index j. The grids in these dimensions are $t = [1, t_{max}], i = [1, i_{max}], j = [1, j_{max}]$, with constant grid spacing Δt, Δz, Δp and Δk. The boundary conditions are implemented according to the numerical scheme used. Neumann boundary conditions are imposed for waves and particles such that electrons and waves do not leak out of the simulation domain.

In writing down the finite difference relations we use the following notation

$$f_\ell(z_i, p_j, t_n) = f_{\ell,ij}^n, \qquad N_\ell(z_i, k_j, t_n) = N_{\ell,ij}^n, \tag{4.13}$$

where ℓ is the Legendre index.

The wave equation is discretized in the numerical code using a monotonic scheme [*Kontar*, 2001] for the z advection, which is written below in Equation (4.28). However, an earlier version of the code used, as in *Li et al.* [2002], an explicit backwards difference operator for the $z-$ advection. This is included in this chapter in order to see more clearly how the wave equation is solved numerically, as the monotonic scheme is very complicated when compiled into a single equation. The code uses this scheme for its stability advantages on the advice of Dr. Bo Li.

The particle and wave equations are first written down in explicit form, rather than in matrix notation. This is due to the fact that the explicit form is useful and convenient for a small number of Legendre polynomials, and problems are easier to diagnose that way. Matrix notation is shown later for the particle equation, as its implicit tridiagonal structure lends itself for implementation when $\ell_{max} > 1$.

4.3.3 Wave equation

The discrete finite differenced form of the wave equation, using the numerical schemes named above, is

$$\begin{aligned}
&\frac{1}{\Delta t}(N^{n+1}_{\ell,ij} - N^{n}_{\ell,ij}) \\
&+ \frac{1}{\omega_L(k_j)}\left[\frac{3k_j(v_e)^2_j}{\Delta z}\left(\frac{\ell}{2\ell-1}(N^n_{\ell-1,ij} - N^n_{\ell-1,i-1,j}) + \frac{\ell+1}{2\ell+3}\left(N_{\ell+1,ij} - N_{\ell+1,i-1,j}\right)\right)\right. \\
&\left. - \frac{D_i}{\Delta k}\left(\frac{\ell}{2\ell-1}(N^n_{\ell-1,i,j+1} - N^n_{\ell-1,i,j+1}) + \frac{\ell+1}{2\ell+3}(N^n_{\ell,i,j+1} - N^n_{\ell,i,j-1})\right)\right] \\
&+ \frac{D_i}{k_j\omega_L(k_j)}\frac{\ell(\ell+1)}{(2\ell+1)}\left(N^n_{\ell+1,ij} - N^n_{\ell-1,ij}\right) = \sigma^n_{\ell,ij} + \sum_{m=0}^{\ell_{\max}} \Gamma^n_{\ell m,ij} N^n_{m,ij}, \qquad (4.14)
\end{aligned}$$

where

$$D_i = \frac{1}{2}\left(\frac{\partial n_0}{\partial z}\right)_i + \frac{3}{2}\left(\frac{\partial T_e}{\partial z}\right)_i \tag{4.15}$$

$$\sigma^n_{\ell,ij} = \left(\frac{1}{n_e}\right)_i \frac{\omega_L(k_j)^3}{k_j^3} \int_{p_\phi(k_j)}^{p_{\max}} dp\, \frac{p^2}{v^2} P_n\left(\frac{\omega_L(k_j)}{k_j v}\right) f_n(p) \tag{4.16}$$

$$\begin{aligned}\Gamma^n_{\ell m,ij} = \left(\frac{1}{n_e}\right)_i \frac{\omega_L(k_j)^4}{k_j^3} \sum_{s=|n-\ell|}^{\min\{|n-\ell|,m\}} \frac{2n+1}{2} A_{nsl} \Bigg\{ & \frac{p_\phi(k_j)^2}{v_\phi(k_j)^2} f_s(p_\phi) \\ & + \int_{p_\phi(k_j)}^{p_{\max}} dp \frac{2p}{c^2} P_s\left(\frac{\omega_L(k_j)}{k_j v}\right) f_s(p) \\ & + \left[\left(\frac{\omega_L(k_j)}{k_j c}\right)^2 - 1\right] \int_{p_\phi(k_j)}^{p_{\max}} dp \frac{p}{v v_\phi} P_s\left(\frac{\omega_L(k_j)}{k_j v}\right) f_s(p) \Bigg\}\end{aligned} \tag{4.17}$$

4.3.4 Particle equation

The discrete form of the dimensionless particle equation is

$$\begin{aligned}&\frac{1}{\Delta t}\left(f^{n+1}_{l,ij} - f^n_{l,ij}\right) + \frac{v}{\Delta z}\left\{\frac{l}{2l-1}\left(f^n_{l-1,ij} - f^n_{l-1,i-1,j}\right) + \frac{l+1}{2l+3}\left(f^n_{l+1,ij} - f^n_{l+1,i-1,j}\right)\right\} \\ &= \frac{1}{p_j^2}\sum_{m=0}^{\ell_{max}} \Bigg\{ \frac{1}{\Delta p^2}\Big[P^n_{lm,ij+1}(f^{n+1}_{m,ij+1} - f^{n+1}_{m,ij}) - P_{lm,ij-1}(f^{n+1}_{m,ij} - f^{n+1}_{m,ij-1}) \\ &\quad + P^n_{lm,ij}(f^{n+1}_{m,ij+1} - 2f^{n+1}_{m,ij} + f^{n+1}_{m,ij-1})\Big] + \frac{1}{2\Delta p}\left(Q^n_{lm,ij} + Q^n_{lm,ij+1}\right)\left(f^n_{m,ij+1} - f^n_{m,ij}\right) \\ &\qquad + \frac{1}{\Delta p} R^n_{lm,ij}\left(f^n_{m,ij+1} - f^n_{m,ij}\right) + S^n_{lm,ij} f^n_{m,ij}\Bigg\}.\end{aligned} \tag{4.18}$$

Or, using the notation,

$$\boldsymbol{f}^n_{ij} = \begin{pmatrix} f^n_{0,ij} \\ \vdots \\ f^n_{\ell,ij} \\ \vdots \\ f^n_{\ell_{max},ij} \end{pmatrix}, \qquad \boldsymbol{Q}^n_{ij} = \begin{pmatrix} Q^n_{00,ij} & Q^n_{01,ij} & \cdots \\ Q^n_{10,ij} & \ddots & \\ \vdots & \vdots & \ddots \\ Q^n_{\ell_{max}0,ij} & \cdots & Q^n_{\ell_{max}\ell_{max},ij}, \end{pmatrix} \tag{4.19}$$

the matrix form of the finite difference equation for the particle equation (4.18) is

$$\frac{1}{\Delta t}\left(\boldsymbol{f}_{ij}^{n+1}-\boldsymbol{f}_{ij}^{n}\right)+\frac{1}{\Delta z}v_j\mathbf{H}(\boldsymbol{f}_{ij}^{n}-\boldsymbol{f}_{i-1,j}^{n})=\frac{1}{p_j^2}\Bigg\{\frac{1}{\Delta p^2}\Big[\mathbf{P}_{i,j+1}^{n}(\boldsymbol{f}_{i,j+1}^{n+1}-\boldsymbol{f}_{ij}^{n+1}) - \mathbf{P}_{ij-1}^{n}(\boldsymbol{f}_{ij}^{n+1}-\boldsymbol{f}_{i,j-1}^{n+1})+\mathbf{P}_{ij}^{n}(\boldsymbol{f}_{ij+1}^{n+1}-2\boldsymbol{f}_{ij}^{n+1}+\boldsymbol{f}_{ij-1}^{n+1})\Big] + \frac{1}{2\Delta p}(\mathbf{Q}_{ij}^{n}+\mathbf{Q}_{ij+1}^{n})(\boldsymbol{f}_{ij+1}^{n}-\boldsymbol{f}_{ij}^{n})+\frac{1}{\Delta p}\mathbf{R}_{ij}^{n}(\boldsymbol{f}_{ij+1}^{n}-\boldsymbol{f}_{ij-1}^{n})+\mathbf{S}_{ij}^{n}\boldsymbol{f}_{ij}^{n}\Bigg\}. \tag{4.20}$$

Here the matrix elements of $\mathbf{P}$, $\mathbf{Q}$, $\mathbf{R}$, and $\mathbf{S}$, which are used in both Equation (4.20) and (4.18) are

$$P_{\ell m,ij}^{n}=\frac{\omega_L(k_j)^5}{n_e}\frac{p_j^2}{v_j^3}\sum_{s=|\ell-m|}^{\min\{\ell_{max},\ell+m\}}\frac{2\ell+1}{2}A_{\ell sm}\int_{\omega_L(k_j)/v_j}^{k_D}\frac{dk}{k}N_{s,ij}^{n}(k)P_s\left(\frac{\omega_L(k)}{kv_j}\right), \tag{4.21}$$

$$Q_{\ell m,ij}^{n}=p_j^2A_{p,ij}\delta_{\ell l}-\frac{\omega_L(k_j)^5}{n_e}\frac{p_j}{v_j^3}\sum_{s=|\ell-m|}^{\ell+1}\frac{2\ell+1}{2s(s+1)}\lambda_{\ell sm}^{(1)}\int_{\omega_L(k_j)/v_j}^{k_D}\frac{dk}{k} \times\left[\left(\frac{kv_j}{\omega_L(k)}\right)^2-1\right]^{1/2}N_{s,ij^*}^{n}(k)P_s^1\left(\frac{\omega_L(k)}{kv_j}\right), \tag{4.22}$$

$$R_{\ell m}=\frac{\omega_L(k_j)^5}{n_e}\frac{p_j}{v_j^3}\sum_{s=|\ell-m|}^{\min\{\ell_{max},\ell+m\}}\frac{2\ell+1}{2s(s+1)}\lambda_{ms\ell}^{(1)}A_{\ell sm}\int_{\omega_L(k_j)/v_j}^{k_D}\frac{dk}{k} \times\left[\left(\frac{\omega_L(k)}{kv_j}\right)^2-1\right]^{1/2}N_{s,ij^*}(k)^nP_s^1\left(\frac{\omega_L(k)}{kv_j}\right) \tag{4.23}$$

$$S_{\ell m}=-\frac{\omega_L(k_j)^5}{n_e}\frac{1}{v_j^3}\sum_{s=|\ell-m|}^{\min\{\ell_{max},\ell+m\}}\frac{2\ell+1}{2}A_{\ell sm} \int_{\omega_L(k_j)/v_j}^{k_D}\frac{dk}{k}\frac{1}{2}\left[\left(\frac{kv_j}{\omega_L(k)}\right)^2-1\right]N_{s,ij^*}^{n}(k)\left[\lambda_{s\ell m}^{(1)}P_s\left(\frac{\omega_L(k)}{kv_j}\right]+\frac{(s-2)!}{(s+2)!}\lambda_{s\ell m}^{(2)}P_s^2\left(\frac{\omega_L(k)}{kv_j}\right)\right]. \tag{4.24}$$

Absorbing the constants Δp, Δt, Δz and the factor p_j^{-2} so that

$$
\begin{aligned}
\mathbf{\Lambda}_{ij}^{N} &= \Delta t(4\pi\Delta p p_j^2)^{-1}\mathbf{P}_{ij}^{n}, & \mathbf{\Omega} &= \Delta t(4\pi\Delta p p_j^2)^{-1}\mathbf{Q}, \\
\mathbf{\Pi} &= \Delta t(4\pi\Delta p p_j^2)^{-1}\mathbf{R} & \mathbf{\Theta} &= \Delta t(4\pi p_j^2)^{-1}\mathbf{S}, \\
\nu_j &= v_j/\Delta z, & & \qquad (4.25)
\end{aligned}
$$

(4.20) becomes

$$
\begin{aligned}
&[1+\mathbf{\Lambda}_{ij-1}^{n}+2\mathbf{\Lambda}_{ij}^{n}+\mathbf{\Lambda}_{ij+1}^{n}]\boldsymbol{f}_{ij}^{n+1}-[\mathbf{\Lambda}_{ij-1}^{n}+\mathbf{\Lambda}_{ij}^{n}]\boldsymbol{f}_{ij-1}^{n+1}-[\mathbf{\Lambda}_{ij+1}^{n}+\mathbf{\Lambda}_{ij}^{n}]\boldsymbol{f}_{ij+1}^{n+1} \\
&= -\nu_j\mathbf{H}(\boldsymbol{f}_{ij}^{n}-\boldsymbol{f}_{i-1,j}^{n})+\frac{1}{2}(\mathbf{\Omega}_{ij}^{n}+\mathbf{\Omega}_{ij+1}^{n})(\boldsymbol{f}_{ij+1}^{n}-\boldsymbol{f}_{ij}^{n})+\mathbf{\Pi}_{ij}^{n}(\boldsymbol{f}_{ij+1}^{n}-\boldsymbol{f}_{ij-1}^{n})+\mathbf{\Theta}_{ij}^{n}\boldsymbol{f}_{ij}^{n}. \qquad (4.26)
\end{aligned}
$$

4.3.5 Wave equation with the monotonic scheme

Having written down the wave and particle equation with an explicit backward difference operator for advection in space, the monotonic scheme described by *Kontar* [2001] is now shown using the wave equation.

Let

$$
\begin{aligned}
\beta_j &= \frac{3v_e^2}{\omega_L(k)}\frac{\Delta t}{\Delta z}, \\
D_{1,j} &= D\frac{\Delta t}{\Delta k}, \qquad (4.27)
\end{aligned}
$$

then

$$
\begin{aligned}
N^{n+1}_{\ell ij} &= N^n_{\ell ij} \\
&+ \frac{\ell}{2\ell-1}\begin{Bmatrix} -\beta_j(N^n_{\ell-1,ij} - N^n_{\ell-1,i-1,j}) - \beta_j(1-\beta_j)(\Delta N^n_{\ell-1,ij} - \Delta N^n_{\ell-1,i-1,j}), & \beta_j > 0 \\ -\beta_j(N^n_{\ell-1,i+1,j} - N^n_{\ell-1,ij}) + \beta_j(1+\beta_j)(\Delta N^n_{\ell-1,i+1,j} - \Delta N^n_{\ell-1,ij}), & \beta_j < 0 \end{Bmatrix} \\
&- \frac{\ell+1}{2\ell+3}\times \\
&\begin{Bmatrix} -\beta_j(N^n_{\ell+1,ij} - N^n_{\ell+1,i-1,j}) - \beta_j(1-\beta_j)(\Delta N^n_{\ell+1,ij} - \Delta N^n_{\ell+1,i-1,j}), & \beta_j > 0 \\ -\beta_j(N^n_{\ell+1,i+1,j} - N^n_{\ell+1,ij}) + \beta_j(1+\beta_j)(\Delta N^n_{\ell+1,i+1,j} - \Delta N^n_{\ell+1,ij}), & \beta_j < 0 \end{Bmatrix} \\
&+ \frac{\ell}{2\ell-1}\times \\
&\begin{Bmatrix} -D_{1,j}(N^n_{\ell-1,ij} - N^n_{\ell-1,i,j-1}) - D_{1,j}(1-D_{1,j})(\Delta N^n_{\ell-1,ij} - \Delta N^n_{\ell-1,i,j-1}), & D_{1,j} > 0 \\ -D_{1,j}(N^n_{\ell-1,i,j+1} - N^n_{\ell-1,ij}) + D_{1,j}(1+D_{1,j})(\Delta N^n_{\ell-1,i,j+1} - \Delta N^n_{\ell-1,ij}), & D_{1,j} < 0 \end{Bmatrix} \\
&- \frac{\ell+1}{2\ell+3}\times \\
&\begin{Bmatrix} -D_{1,j}(N^n_{\ell+1,ij} - N^n_{\ell+1,i,j-1}) - D_{1,j}(1-D_{1,j})(\Delta N^n_{\ell+1,ij} - \Delta N^n_{\ell+1,i,j-1}), & D_{1,j} > 0 \\ -D_{1,j}(N^n_{\ell+1,i,j+1} - N^n_{\ell+1,ij}) + D_{1,j}(1+D_{1,j})(\Delta N^n_{\ell+1,i,j+1} - \Delta N^n_{\ell+1,ij}), & D_{1,j} < 0 \end{Bmatrix} \\
&- \frac{\Delta t D_j}{k_j \omega_L(k_j)} \frac{\ell(\ell+1)}{2\ell+1}(N^n_{\ell+1,ij} - N^n_{\ell-1,ij}) + \sigma^n_{\ell,ij} + \sum_{m=0}^{\ell_{\max}} \Gamma^n_{\ell m,ij} N^n_{m,ij}, \qquad (4.28)
\end{aligned}
$$

$$
(4.29)
$$

where

$$
\Delta N^n_i = \begin{cases} \frac{(N^n_i - N^n_{i-1})(N^n_{i+1} - N^n_i)}{(N^n_{i+1} - N^n_{i-1})}, & (N^n_i - N^n_{i-1})(N^n_{i+1} - N^n_i) > 0, \\ 0, & \text{otherwise.} \end{cases} \qquad (4.30)
$$

The code is relativistically correct, so the relationship between the momentum p and the resonant wavenumber k is obtained by the following argument. First, from the definition, momentum and speed are related by

$$
p = \frac{v}{\sqrt{1 - \frac{v^2}{c^2}}}. \qquad (4.31)
$$

The Landau resonance condition is $v = \omega_L(k)/k$, which combined with the Langmur wave dispersion relation gives the following expression for the Landau (or 1D) resonant wavenumber at the spatial coordinate z:

$$
k_\phi(z) = \omega_p(z) \sqrt{\frac{1 + \frac{p^2}{c^2}}{p^2\left(1 - \frac{3v_e^2(z)}{c^2}\right) - 3v_e^2(z)}}. \qquad (4.32)
$$

From Equations (4.31) and (4.32), the relationship between respective grid spacings are

$$\begin{aligned}
\Delta p &= -1/2(v^{-2}-c^{-2})^{-3/2}(-2v^{-3}\Delta v) = p^3(p^{-2}+c^{-2})^{3/2}\Delta v, \\
\Delta v &= p^{-3}(p^{-2}+c^{-2})^{-3/2}\Delta p, \\
\Delta k &= -\omega_p^{-2}k^3p^{-3}(p^{-2}+c^{-2})^{-2}\Delta p.
\end{aligned} \tag{4.33}$$

If a regular grid spacing in p is used and these resonance conditions used directly between the wave and particle equations, an irregular k-grid would need to be employed. This would further complicate the numerical scheme required to solve the Langmuir wave equation, so in this thesis a regular grid in k is defined, with the resonance given in Equation 4.32 imposed in each of the resonant terms in the wave and particle equations by interpolating to the resonant gridpoint. If one wishes to plot wave distributions on the same axes as the waves, i.e. as functions of p_ϕ, it is straightforward to transform the output data, and the cost of this extra step is outweighed by the numerical benefits of a regular k grid.

4.3.6 Block tridiagonal implicit scheme for the particles

The structure of the matrix form of the particle equation 4.26 is block-tridiagonal. That is, the only nonzero elements of the matrix are in "blocks" along the main diagonal and on the upper and lower diagonals, as can be seen in the leftmost matrix in Equation (4.35). The block tridiagonal structure of the particle equation can be seen by using the the vector $\boldsymbol{\eta}^n_{i,j}$ to represent the right hand side of the equation, i.e.

$$\begin{aligned}
\boldsymbol{\eta}^n_{ij} = &-\nu_j \boldsymbol{H}(\boldsymbol{f}^n_{ij} - \boldsymbol{f}^n_{i-1,j}) + \frac{1}{2}(\boldsymbol{\Omega}^n_{ij} + \boldsymbol{\Omega}^n_{ij+1})(\boldsymbol{f}^n_{ij+1} - \boldsymbol{f}^n_{ij}) \\
&+ \boldsymbol{\Pi}^n_{ij}(\boldsymbol{f}^n_{ij+1} - \boldsymbol{f}^n_{ij-1}) + \boldsymbol{\Theta}^n_{ij}\boldsymbol{f}^n_{ij}.
\end{aligned} \tag{4.34}$$

Thus $\boldsymbol{\eta}^n_{ij}$ collects all the terms dependent on the particle distribution at the $n-$th timestep. Using this, and noting the Neumann boundary condition for diffusion requires $\boldsymbol{f}^n_{ij}$ to be determined separately for $j = 1, 2, 3$ and $j = j_{max}, j_{max}-1, j_{max}-2$, the particle equation becomes

$$\begin{pmatrix} \mathbf{A}^n_{i4} & \mathbf{C}^n_{i4} & & & & \\ \mathbf{B}^n_{i5} & \mathbf{A}^n_{i5} & \mathbf{C}^n_{i5} & & & \\ & \mathbf{B}^n_{i6} & \mathbf{A}^n_{i6} & \mathbf{C}^n_{i6} & & \\ & & \ddots & \ddots & \ddots & \\ & & & \mathbf{B}^n_{ij_{max}-3} & \mathbf{A}^n_{ij_{max}-3} \end{pmatrix} \begin{pmatrix} \boldsymbol{f}^{n+1}_{i4} \\ \boldsymbol{f}^{n+1}_{i5} \\ \boldsymbol{f}^{n+1}_{i6} \\ \vdots \\ \boldsymbol{f}^{n+1}_{ij_{max}-3} \end{pmatrix} = \begin{pmatrix} \boldsymbol{\eta}^n_{i4} \\ \boldsymbol{\eta}^n_{i5} \\ \boldsymbol{\eta}^n_{i6} \\ \vdots \\ \boldsymbol{\eta}^n_{ij_{max}-3} \end{pmatrix}, \tag{4.35}$$

where

$$\begin{aligned} \mathbf{A}^n_{ij} &= 1 + \mathbf{\Lambda}^n_{ij-1} + 2\mathbf{\Lambda}^n_{ij} + \mathbf{\Lambda}^n_{ij+1}, \\ \mathbf{B}^n_{ij} &= -[\mathbf{\Lambda}^n_{ij-1} + \mathbf{\Lambda}^n_{ij}], \\ \mathbf{C}^n_{ij} &= -[\mathbf{\Lambda}^n_{ij} + \mathbf{\Lambda}^n_{ij+1}]. \end{aligned} \tag{4.36}$$

The matrices $\mathbf{A}^n_{ij}$, $\mathbf{B}^n_{ij}$ and $\mathbf{C}^n_{ij}$ are square matrices of size ℓ_{max}, the maximum Legendre expansion index, and as seen in (4.19) the vectors $\mathbf{f}^n_{ij}$ are of size ℓ_{max}. Later, simulation runs are conducted with $j_{max} = 400$ and $\ell_{max} = 40$, which would produce a matrix on the left hand size of Equation (4.35) of size 16000×16000. However, this matrix is quite sparse and has a block tridiagonal form. Following the method outlined in *Varah* [1972], the code uses an LU decomposition technique to solve the particle equation. Further details on the application of this technique can be found in Appendix A.

4.3.7 Code structure

The code written to implement the numerical scheme was written in Fortran 90, and its structure is outlined in Figure 4.1. The most important subroutines are 'fe_solver' and 'NL_solver', which solve for the electron and wave distributions respectively.

4.4 Test cases

4.4.1 Thermal level

A thermal plasma can be described by an isotropic Maxwellian distribution, so that

$$f(p) = \left(\frac{n_e^2}{2\pi m p_e^3}\right)^{\frac{1}{2}} \exp -\frac{p^2}{2p_e^2}. \tag{4.37}$$

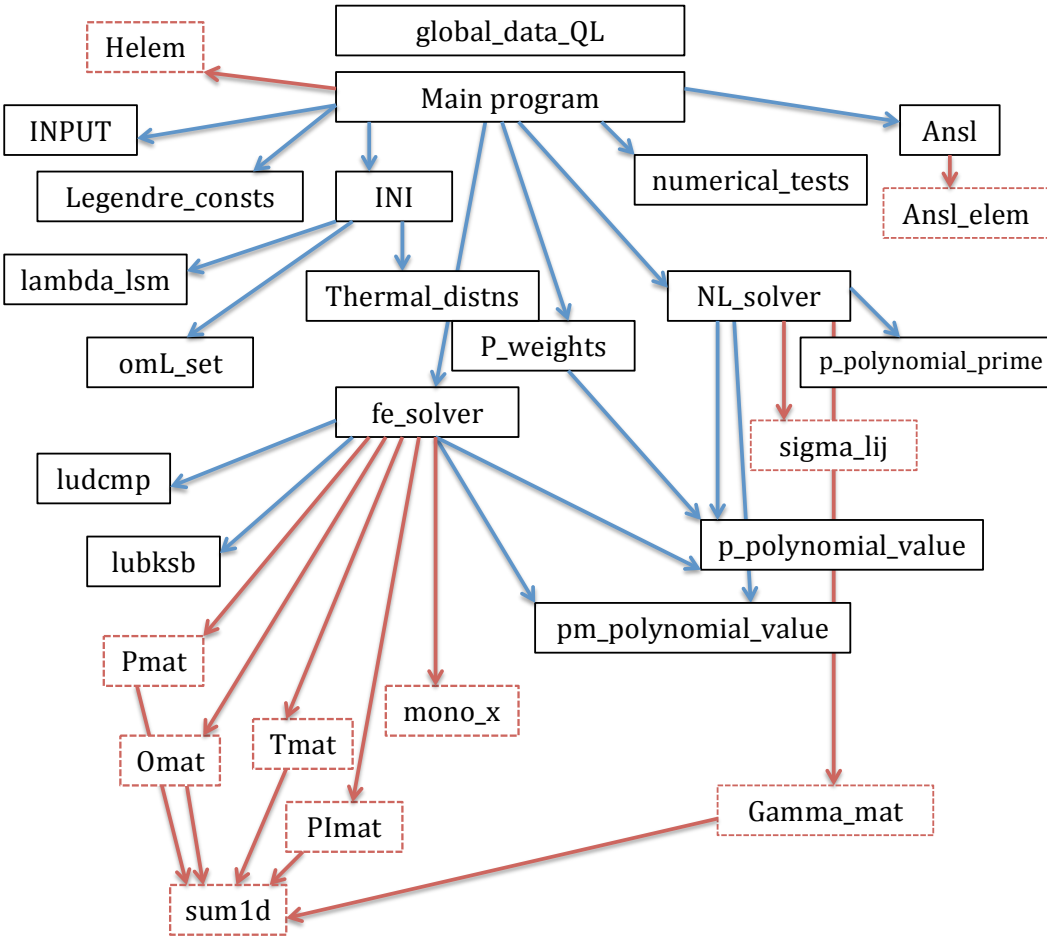

Figure 4.1: Schematic of the modular elements of the simulation code. Black boxed items indicate a subroutine, red boxed items are functions. Blue arrows from box A to box B indicates that box A calls the subroutine in box B, and red arrows indicate calling the function. global_data_QL sets the global variables used in all parts of the code.

This distribution has $\partial f/\partial p < 0$ everywhere, so under the 1D picture of electron-Langmuir wave resonance does not drive wave growth via an instability. Since it is isotropic, $f(p,\alpha) = f_0(p)$, so the 3D resonance condition discussed in Chapter 3 agrees with the 1D case. However, there is a stable, thermal population of Langmuir waves, which is insufficient to explain the brightness temperatures in Type III radio bursts [*Melrose*, 1970]. It is reached by the wave occupation number $N_L(k)$ evolving to a state where the spontaneous emission rate balances the growth rate (which, for a thermal Maxwellian, is negative for all p). The thermal level of waves is an important feature and initial test of the plasma physics and numerical code, as it serves as a reasonable initial condition and it should be stable in any numerical model. In the full 3D demonstration of the problem, the thermal level of waves for a Maxwellian population of electrons is given by the Rayleigh-Jeans distribution,

$$N_{th}(k) = \frac{k_B T_e}{\hbar\omega_L(k)} = -\frac{\alpha_L}{\gamma_L} \tag{4.38}$$

In the dimensionless scheme (4.1), $N_{th}(k) = 1/\omega_L(k)$. Note that N_{th} is dimensionless, as any occupation number should be. A particular problem with taking a 1D approximation is that, depending on the approach taken in moving to a 1D system, the thermal level of waves acquires an inconsistent dimension. For example, in taking a '1D Universe approach', a thermal level with inconsistent units is derived. A motivation to conduct a full 3D simulation of the electron beam-Langmuir wave interaction was initially to investigate the thermal level of waves in light of these theoretical inconsistencies, so a code in which specific thermal populations of electrons can be assumed and the thermal level of waves numerically calculated is especially necessary.

A thermal level of waves is indeed stable in the numerical scheme described in Section 4.3, demonstrated by considering the spontaneous emission term $\sigma_L(k)$ and the growth rate $\Gamma_L(k)$ and by allowing a thermal level of waves to evolve for a long timescale. Note that quasilinear effects are expected to develop on the order of ω_p^{-1} and the timestep must be less than Γ_L^{-1}[*Li et al.*, 2002] in order to resolve the growth of waves. This test demonstrates that the spontaneous emission and growth rates are calculated correctly in this case and the system is well-resolved numerically in phase space.

An additional test of the code using the thermal level uses the fact that a suprathermal distribution of waves should evolve towards a thermal level,

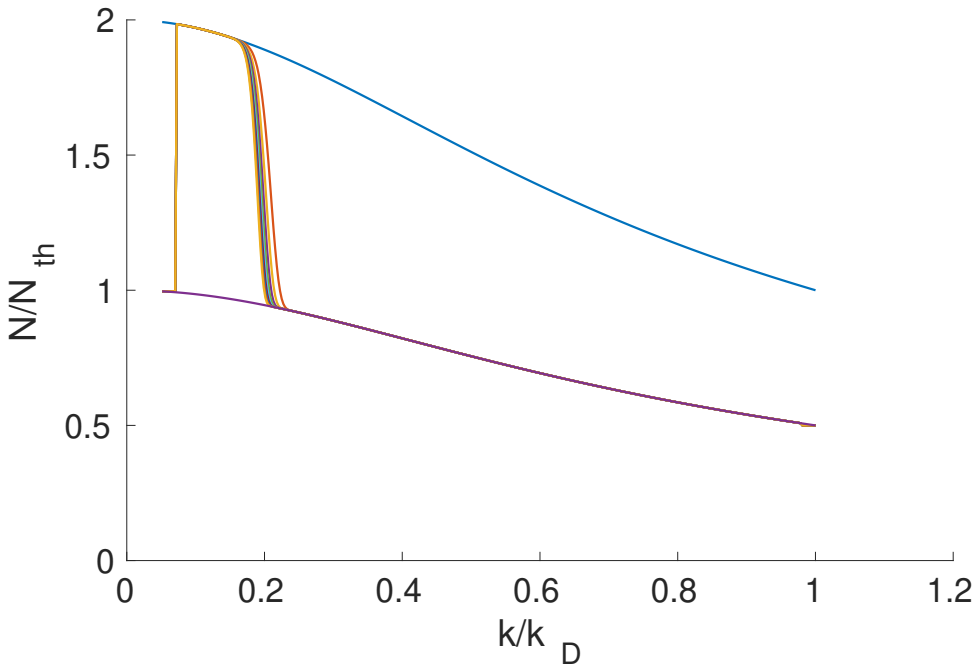

Figure 4.2: Evolution of suprathermal wave population down to the thermal level. As theoretically predicted, the asymptotic state for the wave distribution is the thermal level N_{th}, but the growth rate γ_L is extremely small for $k < 0.2$, so the evolution there proceeds slowly. The timesteps increase in increments of $10^3\omega_p^{-1}$, such that the leftmost curve is at $t = 10^4\omega_p^{-1}$.

given a thermal distribution of particles. If the initial level of waves is small, then it is expected that the wave distribution evolves to the thermal level with minimal impact on the electrons. This was tested by beginning with a wave distribution $N(k) = 2N_{th}$. The waves evolved quickly towards the thermal level for $k > 0.2$, as shown in Figure 4.2.

The behaviour of the waves for $k < 0.2$ is consistent with theoretical predictions for the thermal level of an isotropic Maxwellian distribution. Considering an initial level of waves that does not significantly change the particles, the quasilinear wave equation for isotropic waves ($N_L(k,\theta) = N_0(k)$) can be easily solved,

$$\begin{aligned} N_0(k,t) &= -\frac{\alpha_L(k)}{\gamma_L(k)} + \left(N_0(t=0) - \frac{\alpha_L(k)}{\gamma_L(k)}\right) e^{\gamma_L(k)t} \\ &= N_{th}(k) + [N_0(t=0) - N_{th}(k)]e^{\gamma_L(k)t}, \end{aligned} \tag{4.39}$$

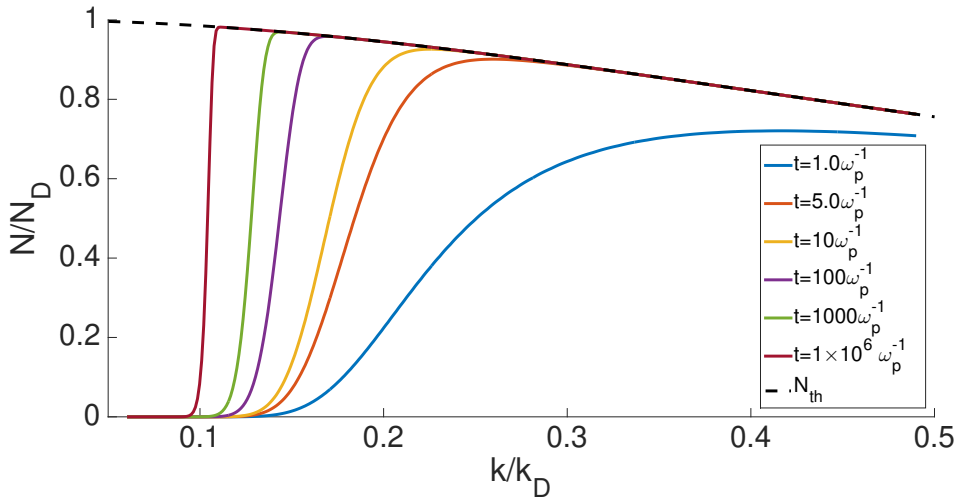

Figure 4.3: Evolution of waves from an initially empty distribution in the presence of a thermal Maxwellian population of electrons. Langmuir waves develop towards the expected thermal level of waves, but this evolution is prohibitively slow for small k.

using the thermal level $N_{th} = -\alpha_L/\gamma_L$. Now, the thermal Maxwellian has $f_0(p) \approx 0$ for $p \gg p_e$, and the isotropic growth rate has $\gamma_L(k) \propto k^{-3} f_0(p_\phi)$. So $\gamma_L(k) \approx 0$ for $p_\phi \gg p_e$, which means that $N_0(k,t)$ will evolve very slowly where p_ϕ is large, i.e. small k. This implies that if there is a Langmuir wave population at small k, a thermal Maxwellian population of electrons will not rapidly damp it away. It also implies that a subthermal population of Langmuir waves will grow to a thermal population, but extremely slowly when p_ϕ is large. This behaviour is simulated with an initial wave distribution of $N_L = 0$, as shown in Figure 4.3. At very large timescales ($10^6 \omega_p^{-1}$) there are still no waves at $k < 0.1 k_D$.

In summary, the simulation code is behaving correctly with respect to the thermal level of waves and has demonstrated an effect that has been neglected in previous investigations but is consistent with the theory. It is therefore appropriate to move to a higher-order case to further test and develop the code.

4.4.2 Isotropic gap

Thus far in this thesis we have focussed on applications of the bump-on-tail kinetic instability when discussing plasma emission, as Type III radio bursts are generated via this process. It is possible however to have measurable metre-wave emission via certain electron distributions that are not unstable to the growth of Langmuir waves. Isotropic distributions always have a negative growth rate γ_L, but have a stable thermal population of Langmuir waves [*Melrose*, 1975]. This latter effect is possible because a wave distribution evolves such that the spontaneous emission rate is balanced by the damping, i.e.

$$\gamma_L = \alpha_L N_L, \tag{4.40}$$

so if γ_L is smaller than the thermal Maxwellian damping

The questions, then, become a) is an electron distribution can produce a stable Langmuir wave population N_L large enough to lead to measurable radio emission? and b) can such an electron distribution form in the solar corona and IPM?

Melrose [1975] and *Robinson* [1975] suggest that some isotropic distributions, specifically "isotropic gap distributions", can indeed produce sufficient Langmuir turbulence for observable radio emission, and that such distributions could form naturally. Some mechanisms for gap formation are faster particles filling a flux loop before slower particles are able to, resonant scattering by Whistler waves (a process which has a cutoff speed and thereby can only affect fast particles) and collisional efects. Due to the strict limits on levels of waves induced by isotropic electron distributions, *Melrose* [1975] argued that it is not possible for them to be involved in Type III burst production, but they may play a role in Types I, II, stationary Type IV, and V bursts.

An isotropic gap distribution is defined by three properties. First, it is an isotropic distribution of particles, i.e. $f(p, \alpha) = f_0(p)$. Second, it contains a region of phase space $0 < |p - \Delta p| < p_0$ where there are effectively no particles, that is, $f_0(p)$ is less than 1 particle/Debye volume. And finally at some $p > p_0$ there exists some electron population, most often modelled as an offset Maxwellian centred at p_b. This combination can be modelled by

$$f = f_{th}(p) + n_b \exp(-(p - p_b)^2/2p_e^2), \tag{4.41}$$

with the thermal distribution such that $f_{th}(p) \approx 0$ well before $p \to p_b - 2p_e$. Such a model is shown in Figure 4.4.

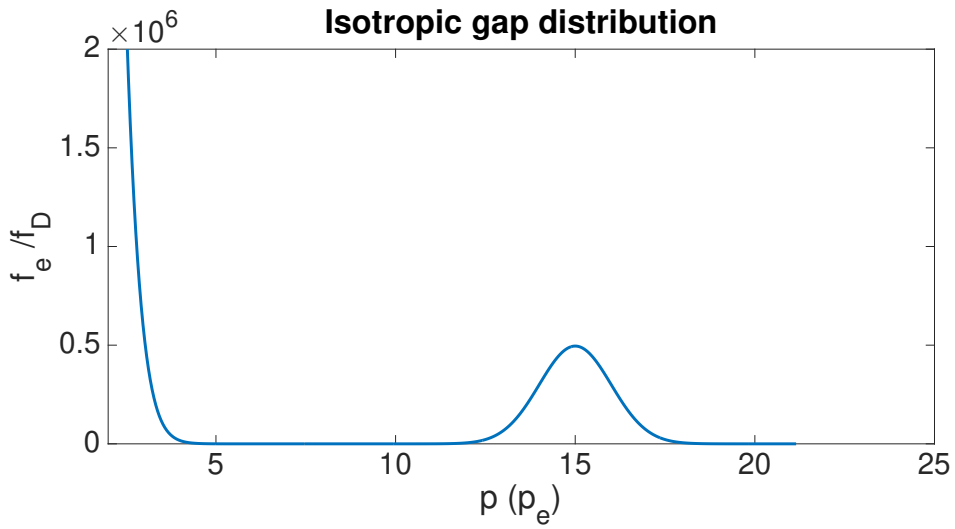

Figure 4.4: Initial isotropic gap distribution, with a thermal population centred at $p = 0$ and a gap in the region $5 \lesssim p/p_e \lesssim 11$. The peak is centred at $p = 15p_e$ and has the same spread in velocity as the thermal population, p_e.

Despite the fact isotropic distributions cannot produce brightness temperatures sufficient to explain most Type III bursts, they are nevertheless interesting plasma physics phenomena, and they are useful in testing the numerical method and simulation code. This is because the associated Langmuir wave distributions are stable and well-defined, and because the assumption of isotropy in the particles greatly reduces the complexity of the equations and the resulting numerical scheme. Also, despite the fact the asymptotic state of isotropic gap distributions has been studied [*Robinson*, 1975; *Melrose*, 1975; *Robinson*, 1978] the intermediate evolution has mostly been passed over. Therefore, isotropic gap distributions provide a good opportunity to both test the numerical code and to examine the time-dependent development of the wave distribution.

Below, we consider the isotropic gap distribution (4.41) with $p_b = 15p_e$. This satisfies the conditions for the gap distribution, which can be seen by inspection in Figure 4.4.

Figure 4.5 shows the spontaneous emission rate $\alpha_L(k)$ and the growth rate $\gamma_L(k)$. We can see that α_L peaks in the gap, whereas the growth rate peaks in magnitude at a higher p_ϕ, closer to the peak of the particle distribution. This allows for growth of waves initially at the high p_ϕ side of the gap. The shapes of α_L and γ_L indicate where in phase space the waves will grow fastest. As

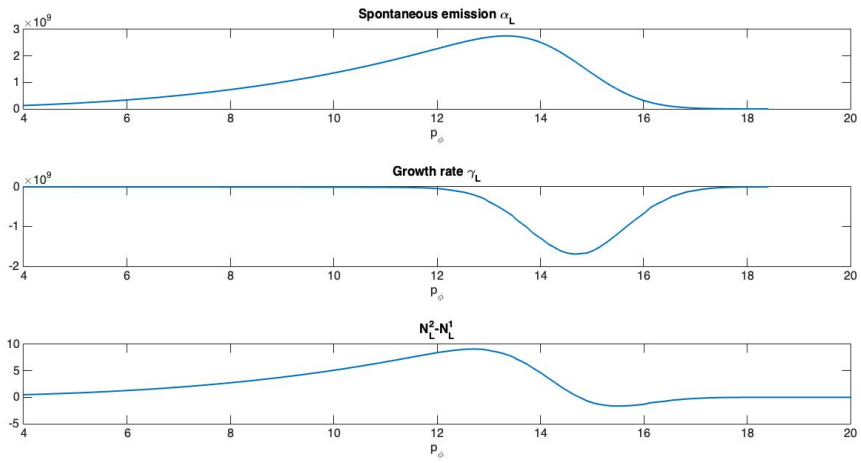

Figure 4.5: Emission and growth terms, with the initial development of waves shown by the difference between timesteps 1 and 2, where $\Delta t = 0.005\omega_p^{-1}$. The positive spontaneous emission peaks at a lower p_ϕ than the negative growth rate, this causing the waves to evolve to a stable level at a range of p_ϕ in the gap.

Figure 4.5 and 4.7 show, the waves reach their asymptotic level at higher p_ϕ first, due to α_L being larger there. This is demonstrated by the waves at an early timestep in the simulation, shown in Figure 4.6.

Figure 4.7 shows the time evolution of the waves associated with the isotropic gap distribution. Waves approach the asymptotic predicted level α_L/γ_L with very good agreement. The timescale over which this happens is quite fast, on the order of $200\omega_p^{-1}$. The rapid development of the saturated level of waves provides support for the approximation that isotropic gap distributions are accompanied by the asymptotic wave distribution.

It is important to note that waves growing in the gap as shown in Figure 4.7 are not a direct example of the resonance effects described in the examples in Chapter 3. Instead their growth is due to in part to the spontaneous emission term, but also to the relativistic part of the growth rate (described in greater detail in *Melrose and Stenhouse* [1977] and for the isotropic gap in particular by *Robinson* [1975] and *Cairns and Melrose* [1985]). Specifically, in the gap $\gamma_L = \gamma_{iso} + \gamma_R + \gamma_{aniso} \approx \gamma_R$ to a very good approximation, since $\gamma_{aniso} = 0$ by construction and $\gamma_{iso} \propto k^{-3} f(p_\phi)$, so in the gap $\gamma_{iso} \ll \gamma_R$. The highly nonthermal wave level in the gap is due to intrinsically relativistic effects. Thus, the

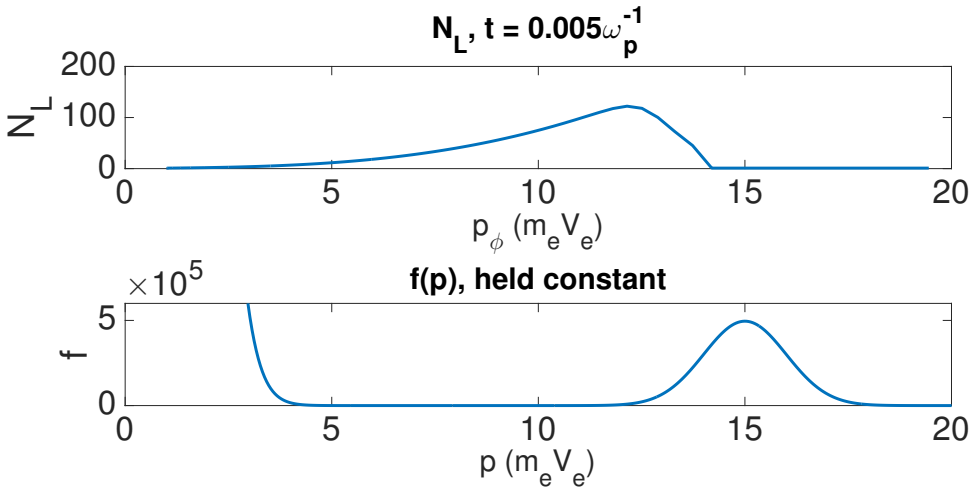

Figure 4.6: A comparison between the growing waves at an early timestep and the isotropic gap.

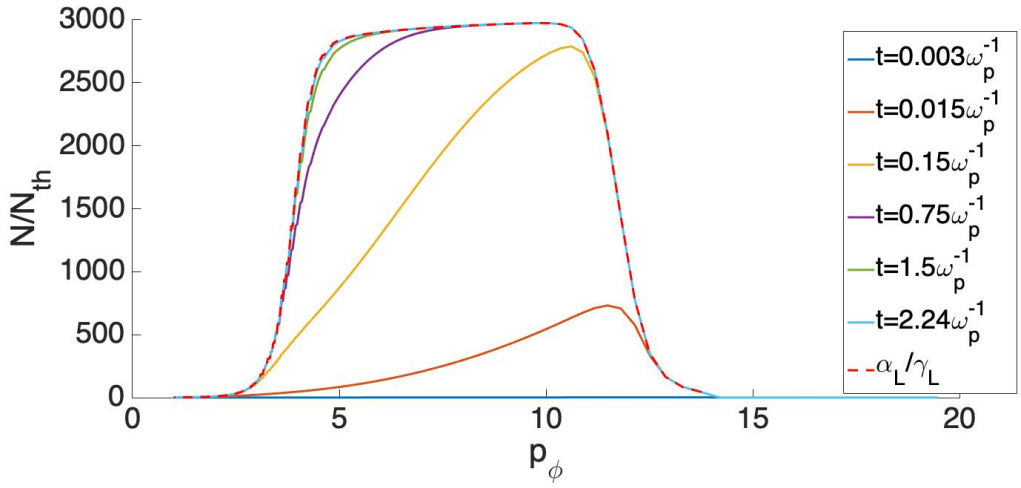

Figure 4.7: N_L evolving with time, up to the asymptotic level where $dN/dt = 0$. The asymptotic level is $-\alpha_L/\gamma_L$ which is shown in the figure as the red dashed line. In terms of phase space, the stable asymptotic wave distribution sits in the gap between the thermal population and the nonthermal peak at $p = 15p_e$. It is interesting that a) the wave distribution evolves quite rapidly in time and b) evolves faster at larger p_ϕ in the higher speed part of the gap than the lower.

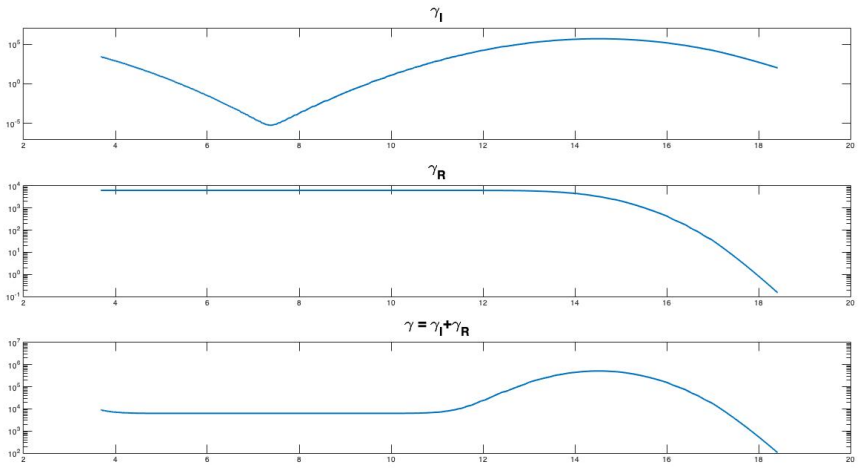

Figure 4.8: The growth rate γ_L can be expressed as $\gamma = \gamma_I + \gamma_R$ for the isotropic gap case. γ_I corresponds to the isotropic component and γ_R is a relativistic contribution.

isotropic gap distribution is clear evidence that, even for semirelativistic speeds where the Lorentz factor is ≈ 1, the full relativistic version of the quasilinear equations should be employed and Figure 4.7 shows that the code is working correctly, and verifying that the asymptotic state predicted analytically is dynamically achievable.

4.5 P_1 simulation: set up and wave growth

Supported by the theoretical considerations in Chapter 3, the simulation code is now applied to P_1 distributions of electrons. The code is initialised with a P_1 electron distribution identical to that in Equation (3.9). The electron distribution is then expected to diffuse in momentum and angle, and the wave distribution should undergo an initial exponential growth phase, before this growth is modulated down by the waves' back reaction on the particles. The initial conditions for the coupled particle/wave distributions are shown in Figure 4.9.

During a period of wave growth, which we call here the nominal wave growth phase, the distributions appear to be behaving in a manner consistent with theory. The wave and particle distributions at the latest timestep ($t = 1200\omega_p^{-1}$) are shown in Figure 4.10.

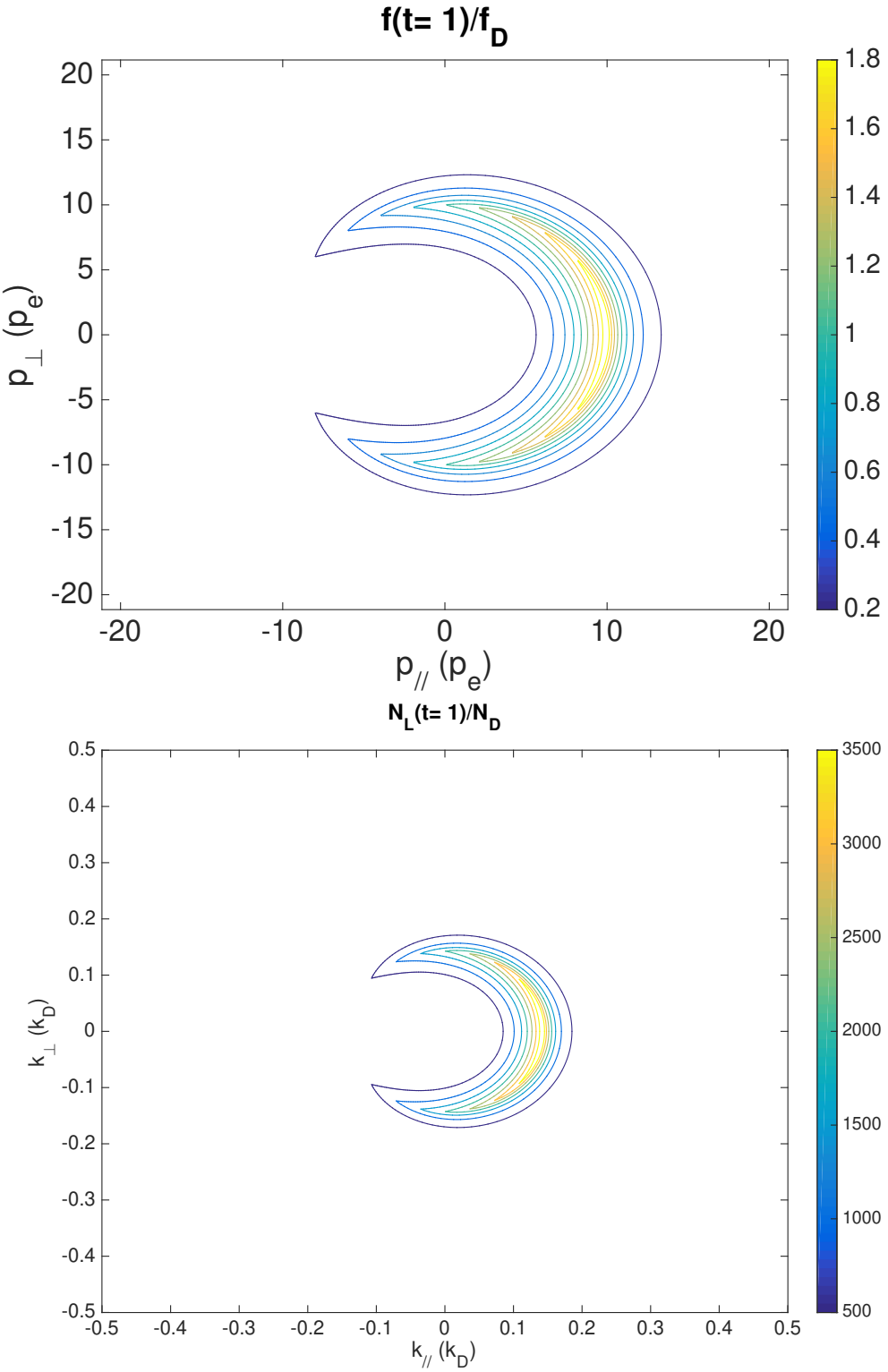

Figure 4.9: The initial conditions for the (a) electrons and (b) waves. Both distributions are initially P_1, with $f_0(p) = f_1(p)$, $N_0(p) = N_1(p)$, and $f_0(p)$ and $N_1(p)$ both double power law distributions.

Taking the maximum of the growing wave distribution to be at $\boldsymbol{k} = \boldsymbol{k}_{peak}$, i.e. $N_L(\boldsymbol{k}_{peak}, t) = maxN_L(\boldsymbol{k}, t)$, one would expect to see this evolve like

$$N_L(k_{peak}, t) = N_L(k_{peak}, t = 0)e^{\gamma_{peak}t}, \tag{4.42}$$

during the exponential growth phase.

Indeed, such exponential behaviour is seen in Figure 4.11. Furthermore, Figure 4.12 shows that, at later times, the rate of growth of the waves (blue) starts to decrease slightly. This is expected, as the electron population loses energy to the waves and becomes less unstable to wave growth.

Also, the expected coupling between Legendre modes of the wave distribution is working. The growth rate for a particular Legendre mode N_ℓ expressed in Equation (4.17) indicates that a given N_ℓ is coupled to neighbouring ℓ values. Accordingly, given time and an initial P_1 distribution higher order ℓ terms than $\ell = 0$ and $\ell = 1$ should become populated, which is consistent with the idea that a wave distribution that is driven by particles becomes more anisotropic with time. This behaviour is seen in the plots of selected Legendre weights shown in Figure 4.13. It is possible that a subsequent late phase of evolution would smooth out the wave and particle distributions, but this has not yet been found in the simulations.

In an attempt to quantify the amount of diffusion in angle compared to diffusion in parallel momentum for these results, the following value is defined

$$n(\alpha, t) = \int dp\, p^2 f(p, \alpha), \tag{4.43}$$

which corresponds to the number of particles along a particular angle. Figure 4.14 shows this quantity for several different angles. Importantly, as t increases $n(\alpha, t)$ increases at small α but increases at $\alpha > 90°$. This behaviour demonstrates angular diffusion of electrons.

The total electron number and momentum is conserved and the wave energy grows as expected. The initial wave energy is very small compared to the particle energy (on the order of 10^{-6} times) and even at the final timestep before the singularity emerges the $E_L \approx 10^{-4}E_f$, so that the increase in wave energy is too small to noticeably change the total energy of the particles yet. These quantities are plotted in Figure 4.15.

However, once the waves have grown substantially, the code runs into a problem as yet unresolved. Figure 4.16 shows when this happens for the P_1

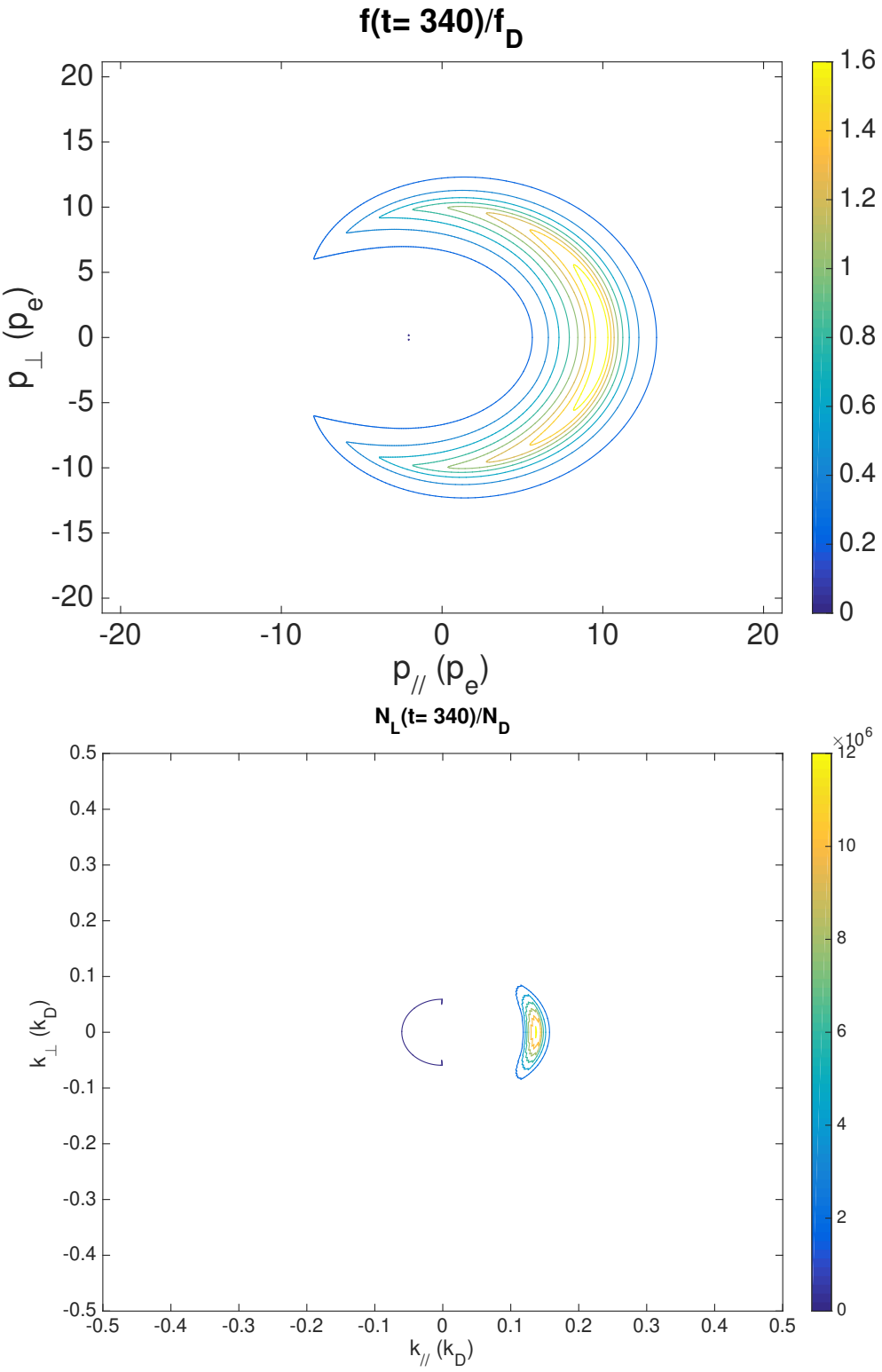

Figure 4.10: Electron and wave distributions at timestep 340, at the end of the nominal wave growth phase of this simulation run. The particles have diffused appreciably and the waves have narrowed significantly.

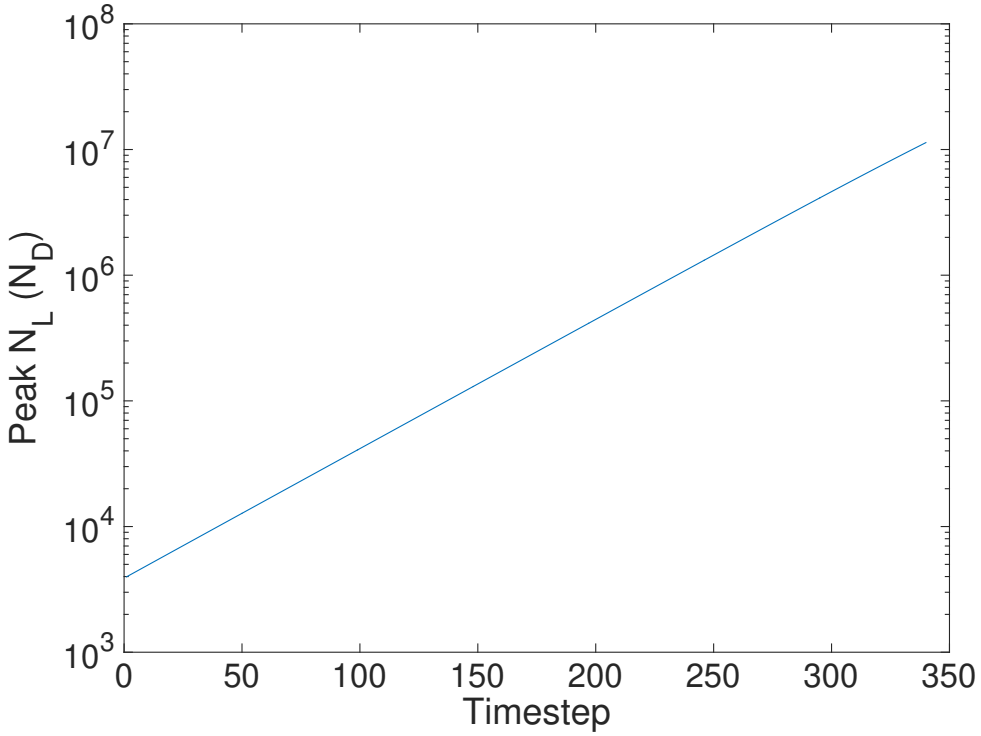

Figure 4.11: Growth of the peak of the wave distribution during the nominal wave growth phase of the simulation. Each timestep corresponds to 2.3×10^{-8} s $= 3.5\omega_p^{-1}$. The evolution is consistent with the expected exponential growth, demonstrated by $N_L(t)$ being very close to a straight line in $logN$ - linear t space.

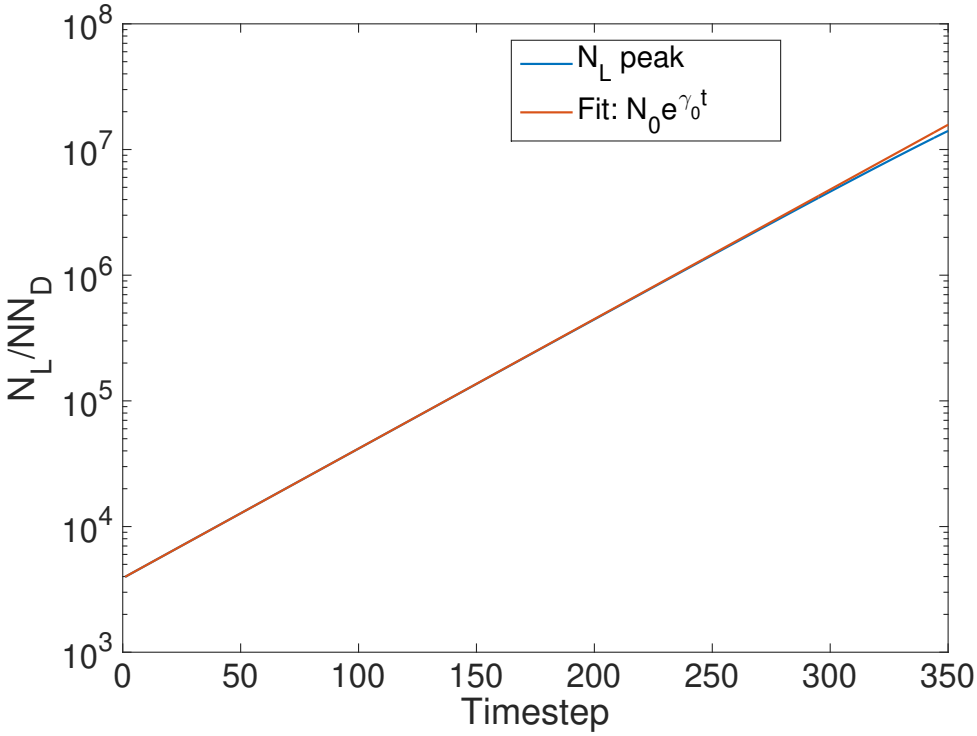

Figure 4.12: Growth of the peak of the wave distribution fitted with an exponential growth model. The peak is well-fitted by exponential growth but begins to deviate at the end of the simulation run. This is consistent with the beginning of the second phase of wave evolution where diffusion of the particles modulates the wave growth.

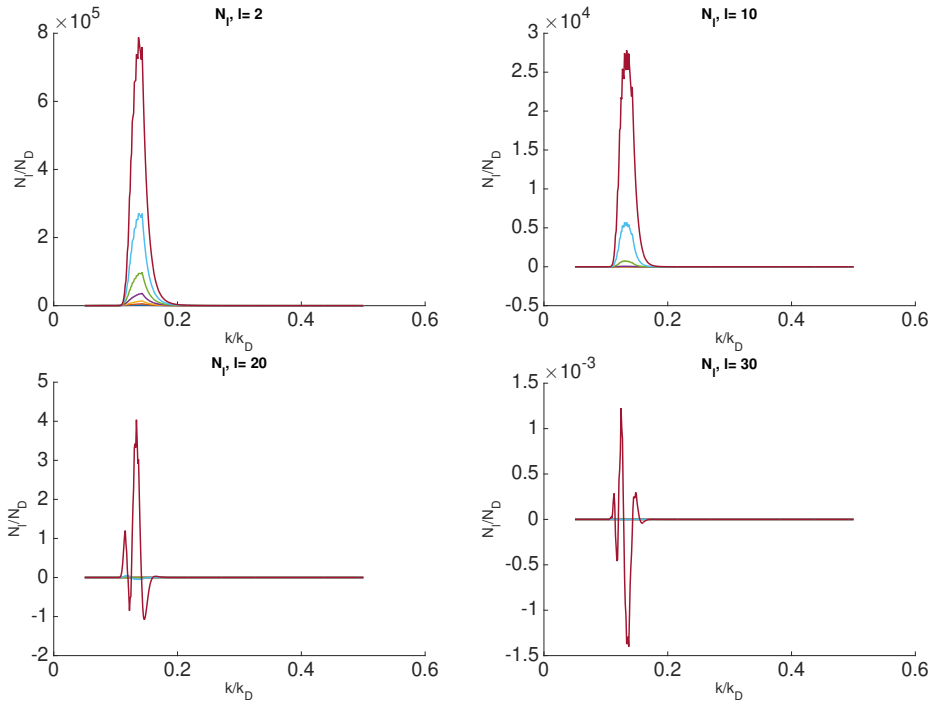

Figure 4.13: Examples of the development of $N_\ell(t)$ for 4 values of ℓ. The colours correspond to increasing timesteps, changing from yellow to brown, green, blue, and red with increasing time: $N_\ell = 0$ for $\ell > 1$ initially, but higher order ℓ terms are populated as expected as the wave distribution evolves, with the magnitude of N_ℓ nevertheless decreasing as ℓ increases.

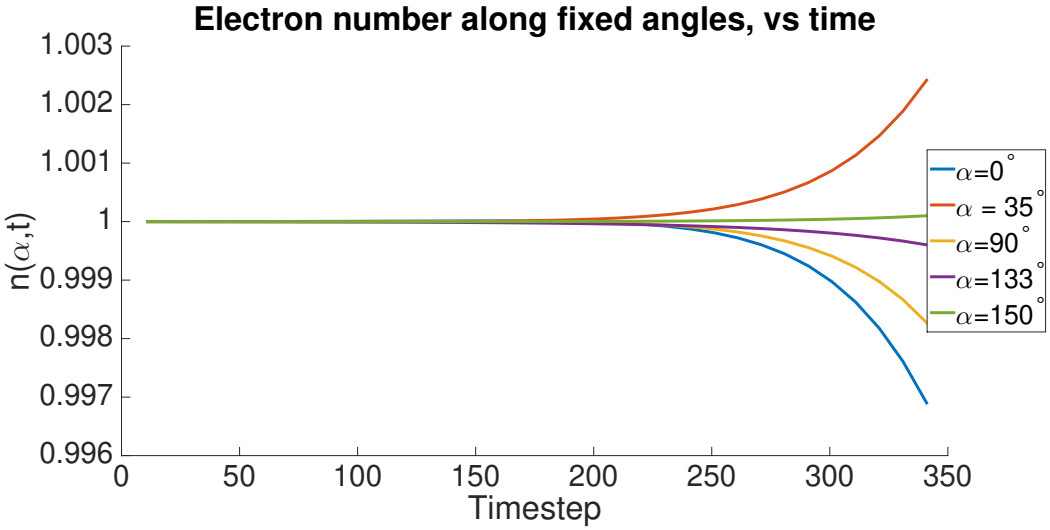

Figure 4.14: $n(\alpha, t)$ for different angles. $n(\alpha, t)$ decreases for larger angles. This is evidence of particles diffusing around in angle.

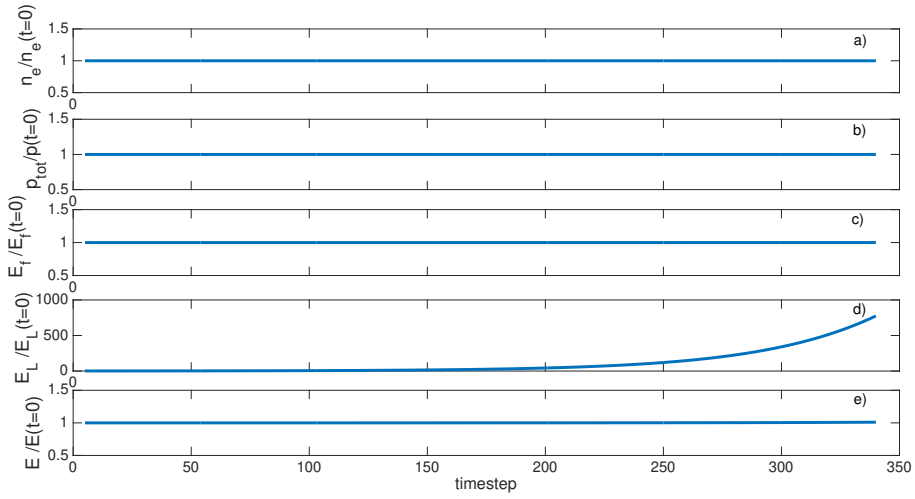

Figure 4.15: Electron number (a), momentum (b), particle energy (c), Langmuir wave energy (d) and total energy (e), each divided by the initial value, for the P_1 growth phase. Electron number, momentum and total energy are conserved with Langmuir wave energy increasing as the waves grow.

distribution run. The maximum wave level shoots up rapidly after timestep 340.

Figure 4.17 shows the full picture of sudden onset instability problem. The problem begins in the particles; the electron distribution develops a positive and negative spike, with very steep gradients. This then propagates to the waves, and the following interaction is unstable and blows up. The numerical method conserves electron number, so a positive spike in the particle distribution (i.e. a positive change in the particle energy and a positive addition to the total electron number) is compensated by a decrease in particles elsewhere (a negative spike) and the conservation of energy means flow on effects to the waves such that the total energy is constant. It is, of course, unphysical for either the wave distribution $f(p, \alpha)$ or the particle distribution $N_L(p, \alpha)$ to be negative anywhere (although particular Legendre components may be). The spikes in the wave distribution cause similar effects to appear at the resonant momenta. This issue is currently in the process of being diagnosed and resolved.

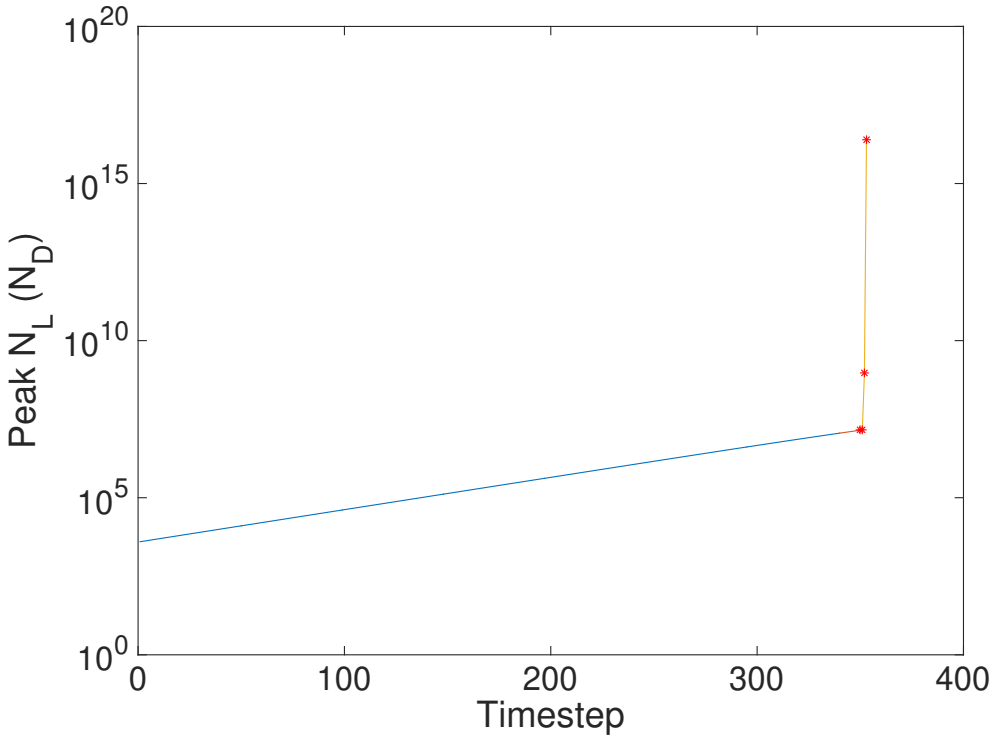

Figure 4.16: The sudden unstable behaviour in the development of the wave distribution, evidenced by the peak of the waves in the last few timesteps

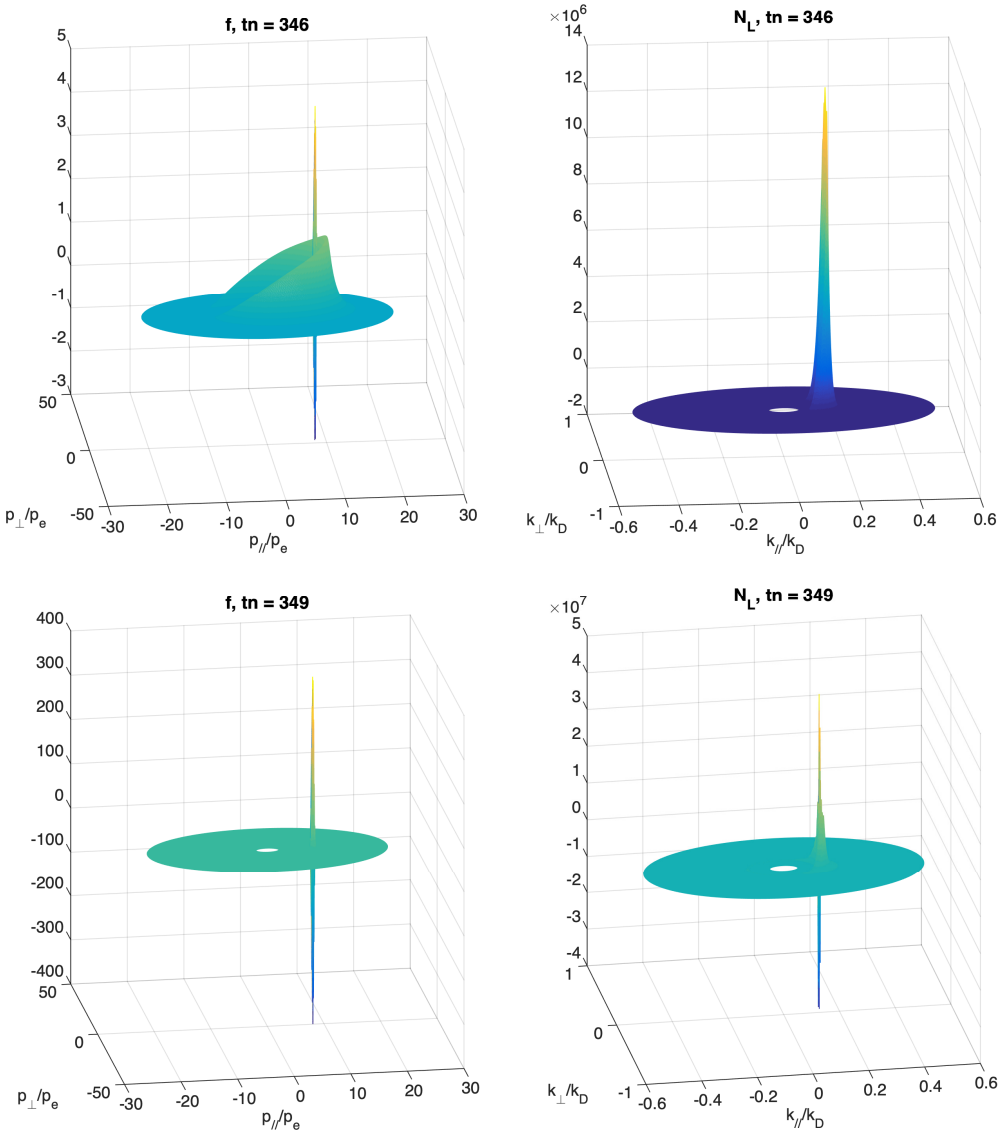

Figure 4.17: Electron and Langmuir wave distributions as the instability problem first emerges. Large paired positive and negative peaks develop which are unphysical and unstable. This singularity has not yet been resolved.

4.6 Diffusion of electron distributions in the presence of fixed Langmuir wave populations

Chapters 3 and *Harding et al.* [2020] demonstrate that the uniquely 3D resonance properties of the electron-Langmuir wave interaction should result in significantly different evolution of the particle distribution than the widely used 1D picture. Specifically, rather than a plateau distribution forming in the $p_\parallel$ direction, the 3D many-to-one resonance suggests electrons also diffuse in pitch angle, broadening any beam structure. We now use the numerical scheme discussed above to test this analytical prediction and explore quasilinear relaxation in 3D. We will consider different forms of the initial electron distribution, as well as isotropic and anisotropic wave distributions. This is done in order to test and develop the numerical code, so as to increase the complexity and the order of Legendre expansion needed for subsequent cases. However, due to the numerical singularity described in Section 4.5 the wave distribution was fixed in time, both in order to diagnose the development of the singularity shown in 4.17 and to look closer at the particle diffusion on its own.

4.6.1 P_1 particle distributions

Here the initial condition of the electrons is a P_1 distribution with double power law form, as in Eq. (3.14), and the waves are fixed at an isotropic, flat distribution $N_L(k,\theta) = N_0$. This is designed as a test, since a flat distribution will point towards problematic regions of $k-p$ space, as well as to check the coupling between Legendre modes. It is found that diffusion proceeds in a reliable way, and shows interesting physical results which support the predictions in Chapter 3, as descrbed in detail next.

Figure 4.18 shows the particle distribution at the first and final timestep in the simulation run, on the same colour bar. Clearly, the distribution has diffused significantly in the $p_\parallel$ direction and in angle. This is demonstrated more clearly in Figure 4.19, which shows slices along 4 different angles at multiple times: as time advances $f(p, 180°)$ increases monotonically with time for all p, while at $\alpha = 0$ and $90°$ $f(p,\alpha)$ decreases monotonically near the peak but increases monotonically at suitably smaller and larger p. At $\alpha = 135°$, $f(p,\alpha)$

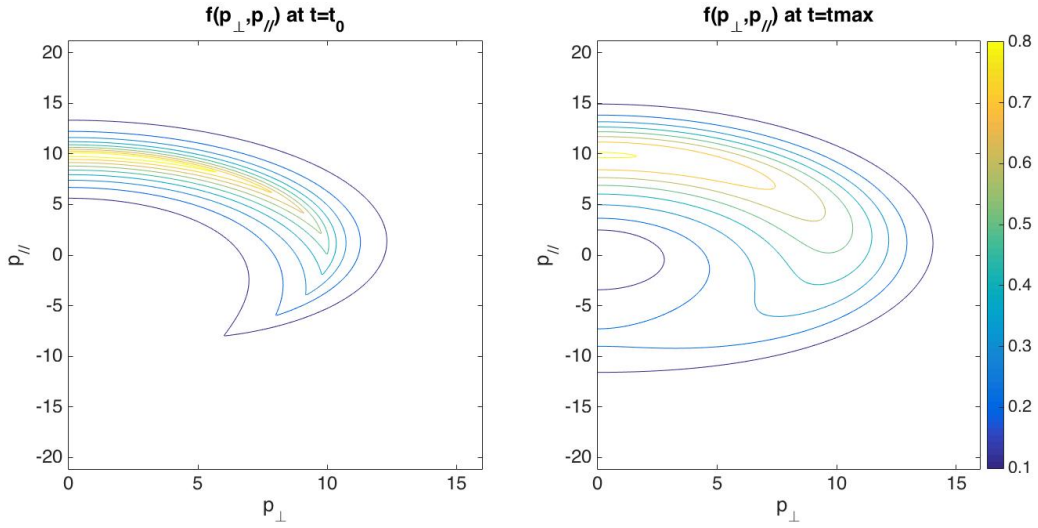

Figure 4.18: Diffusion of the P_1 double power law distribution in the presence of fixed, flat distribution of Langmuir waves. The contours show that the distribution has diffused significantly in parallel momentum but most importantly particles have moved to larger angle.

increases on both sides of the initial peak, with the peak in timeshifting to lower p. In general, the trends are diffusion in angle and to both smaller and larger p than the peak. It is clear that the strict analogue of 1D quasilinear relaxation, which is monotonic diffusion to smaller p (and not in angle), is not occuring. Instead diffusion in angle is strong, accompanied by some diffusion to smaller and larger p, demonstrating the importance of 3D diffusion.

4.6.2 Diffusion terms

In order to test and quantify the diffusion quantitatively, it is useful to consider the equation determining the evolution of the particle equation in spherical polar coordinates, described by

$$\frac{df(p,\alpha)}{dt} = \frac{1}{p^2}\frac{\partial}{\partial p}\left[p^2\left(D_{pp}\frac{\partial}{\partial p} + D_{p\alpha}\frac{\partial}{\partial \alpha} + A_p\right)f(p,\alpha)\right] + \frac{1}{\sin\alpha}\frac{\partial}{\partial \alpha}\left[\sin\alpha\left(D_{\alpha p}\frac{\partial}{\partial p} + D_{\alpha\alpha}\frac{\partial}{\partial \alpha}\right)f(p,\alpha)\right], \tag{4.44}$$

with the coefficients implicit functions of p, α:

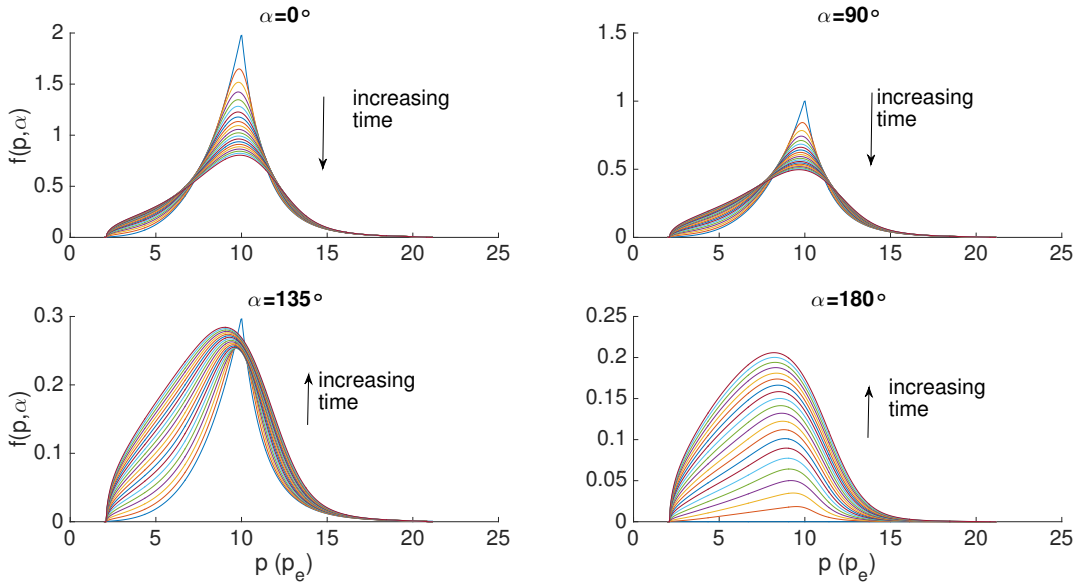

Figure 4.19: Evolution of the P_1 distribution with fixed isotropic waves.

$$
\begin{aligned}
D_{pp}(p,\alpha) &= \frac{e^2\omega_p^2}{\pi\varepsilon_0 v^3}\sum_{m=0}^{\infty}\int_{\omega_p/v}^{k_D}\frac{dk}{k}\,N_m(k)\,P_m(\cos\chi_0)P_m(\cos\alpha),\\
D_{\alpha p}(p,\alpha) &= \frac{e^2\omega_p^2}{\pi\varepsilon_0 v^3 p\sin\alpha}\sum_{m=0}^{\infty}\int_{\omega_p/v}^{k_D}\frac{dk}{k}\,\tan\chi_0\,N_l(k)\frac{P_m^1(\cos\chi_0)P_m^1(\cos\alpha)}{m(m+1)},\\
D_{\alpha\alpha}(p,\alpha) &= \frac{e^2\omega_p^2}{4\pi\varepsilon_0 v^3 p^2\sin^2\alpha}\sum_{m=0}^{\infty}\int_{\omega_p/v}^{k_D}\frac{dk}{k}\,\frac{1}{2}\tan^2\chi_0\,N_m(k)\Bigg[P_m(\cos\chi_0)P_m(\cos\alpha)\\
&\qquad + \frac{(m-2)!}{(m+2)!}P_m^2(\cos\chi_0)P_m^2(\cos\alpha)\Bigg],
\end{aligned}
\tag{4.45}
$$

and $D_{p\alpha}(p,\alpha) = D_{\alpha p}(p,\alpha)$.

The coefficient D_{pp} determines the rate of diffusion in momentum p, and the factor $D_{\alpha\alpha}$ determines the diffusing in pitch angle α. By comparing the ratio $D_{pp}/p^2\sin^2 D_{\alpha\alpha}$, we can see the relative influence of these effects.

For flat waves, with $N_L(k,\theta) = N_0$, the integrands in Equation (4.45) can be integrated analytically to show that

$$
\frac{D_{pp}}{p^2\sin^2\alpha D_{\alpha\alpha}} = \frac{2\ln\left(\frac{k_D}{k_\phi}\right)}{\frac{1}{2}\left(\frac{k_D^2}{k_\phi^2}\right) - \ln\left(\frac{k_D}{k_\phi}\right) - 1}. \tag{4.46}
$$

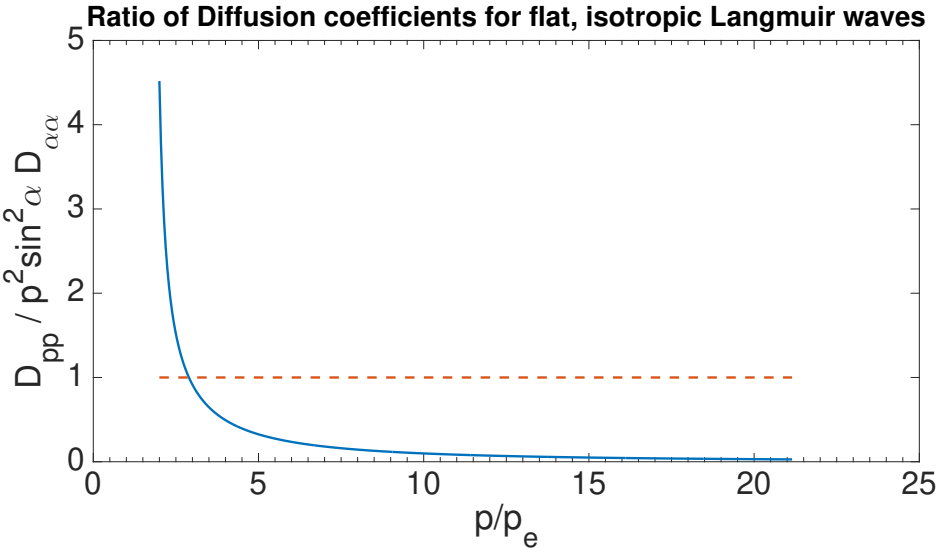

Figure 4.20: Ratio of the diffusion coefficients D_{pp} and $p^2 \sin^2 \alpha D_{\alpha\alpha}$.

The ratio is is plotted in Figure 4.20. The ratio is < 1 for $p > 2.98 p_e$, a result which holds for any p_e and particle distribution. This implies that diffusion in pitch angle is more important over that range, at least when considering isotropic wave distributions.

Writing $D_{pp} \approx (\Delta p)^2/\Delta t$ and $D_{\alpha\alpha} \approx (\Delta\alpha)^2/\Delta t$, the ratio

$$\frac{D_{pp}}{p^2 \sin^2 \alpha D_{\alpha\alpha}} \approx \left(\frac{\Delta p}{p_\perp \Delta \alpha} \right)^2, \tag{4.47}$$

with $p_\perp = p \sin \alpha$. Then, for isotropic flat waves (4.47) implies

$$\Delta p \leq p_\perp \Delta \alpha, \tag{4.48}$$

for $p > 2.98 p_e$, based on Figure 4.20.

For constant $\Delta\alpha$, (4.48) implies that Δp is smaller when $p_\perp$ is smaller. Thus, for p such that $D_{pp}/\sin^2 \alpha D_{\alpha\alpha} < 1$, the particle diffusion behaves less like 1D quasilinear relaxation near $\alpha = 0$ than at larger angles near 90°. This runs counter to the standard 1D picture and strongly suggests that quasilinear relaxation behaves fundamentally differently in three dimensions. Put another way, for $p > 2.98 p_e$ and constant Δp, $\Delta\alpha$ is larger with respect to Δp as $p_\perp$ decreases.

4.6.3 Maxwellian beam distributions

A conventional model for a type III beam is a shifted Maxwellian distribution $f(\mathbf{p}) \propto \exp[-(\mathbf{v}-\mathbf{v_b})^2/2V_b^2]$, or specificially

$$f_\mathrm{b}(p,\alpha) = \frac{n_\mathrm{b}}{[(2\pi)^{1/2}mV_\mathrm{b}]^3}\exp\left[-\frac{v^2+v_\mathrm{b}^2-2vv_\mathrm{b}\cos\alpha}{2V_\mathrm{b}^2}\right], \tag{4.49}$$

where n_b is the number density, v_b is the streaming speed, V_b describes the spread in the beam's "thermal" speed and $\boldsymbol{v_b}$ is assumed to be parallel to $\mathbf{B}$. Usually, one also assumes a thermal Maxwellian centred at $\mathbf{v}=0$ with a density $n_0 \gg n_b$, such that near v_b the dominant influence is the electrons described by (4.49). The total distribution is the sum of these two distributions.

A necessary condition for wave growth to be possible is that the 1D distribution, $F(v_\parallel)$, obtained by integrating the total distribution over the components of velocity perpendicular to the beam ($\cos\alpha = 1$), have a minimum, with $dF(v_\parallel)/dv_\parallel > 0$ between this minimum and a maximum at $v_\parallel \approx v_\mathrm{b}$, as assumed in early numerical models (e.g., *Grognard* [1982]; *Grognard* [1984]).

It is straightforward to expand (4.49) in Legendre polynomials, as in (3.3), with the coefficient of the lth term given by

$$\begin{aligned} f_l(p) &= \frac{n_\mathrm{b}}{[(2\pi)^{1/2}mV_\mathrm{b}]^3}\exp\left(-\frac{v^2+v_\mathrm{b}^2}{2V_\mathrm{b}^2}\right) g_l(p), \\ g_l(p) &= \frac{2l+1}{2}\int_{-1}^{1} d\cos\alpha\, P_l(\cos\alpha)\exp\left(\frac{vv_\mathrm{b}}{V_\mathrm{b}^2}\cos\alpha\right). \end{aligned} \tag{4.50}$$

The first two terms are

$$g_0(p) = \frac{\sinh(vv_\mathrm{b}/V_\mathrm{b}^2)}{vv_\mathrm{b}/V_\mathrm{b}^2}, \qquad g_1(p) = \frac{\sinh(vv_\mathrm{b}/V_\mathrm{b}^2)}{(vv_\mathrm{b}/V_\mathrm{b}^2)^2} - \frac{\cosh(vv_\mathrm{b}/V_\mathrm{b}^2)}{vv_\mathrm{b}/V_\mathrm{b}^2}. \tag{4.51}$$

The expansion in Legendre polynomials is most useful when it converges rapidly, which is only for $vv_\mathrm{b}/V_\mathrm{b}^2 \ll 1$ based on (4.50). Then the two terms (4.51) may be approximated by $g_0(p) = 1$ and $g_1(p) = 3vv_\mathrm{b}/V_\mathrm{b}^2$. However, this approximation requires $v_\mathrm{b}^2 \ll V_\mathrm{b}^2$, and such a distribution has no range where the gradient in p is positive. It follows that the distribution (4.49) is not a useful starting point when discussing the use of the Legendre expansion.

However, it is important for a numerical code to be able to describe an offset Maxwellian well. In Figure 4.21, we show that for a Maxwellian with $v_b = 20V_e$

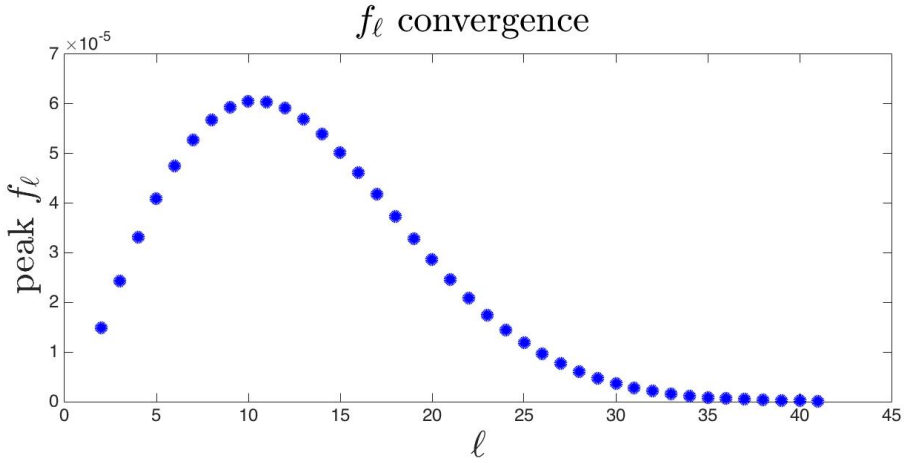

Figure 4.21: Demonstration that for $v_b = 10v_e$, a Legendre expansion with $\ell_{max} \approx 40$ is required to describe an offset Maxwellian of the form 4.49

and $V_b = V_e$ one requires $l_{\max} \approx 40$ in order to sufficiently approximate the distribution. This suggests that most numerical calculations probably only need to calculate up to $\ell_{max} \approx 100$. Further work is required to test this suggestion.

4.7 $\cos^{2N+1}\alpha$ distributions

Available data [*Lin et al.*, 1981; *Ergun et al.*, 1998] suggest electrons beams in the IPM are broad in angle and weakly anisotropic. In order to approximate conditions in the IPM better, we consider distributions of the form

$$f(p,\alpha) = f_0(p)\left[1 + r(p)\cos^{2N+1}\alpha\right], \tag{4.52}$$

Data from *Ergun et al.* [1998], reproduced in Chapter 1 (Figure 1.10) indicates an interplanetary electron beam approximately 60° across. Such a beam is fitted appropriately by a distribution $\propto \cos^5\alpha$, motivating a choice of $N = 2$ in (4.52) for investigation of these distributions. Figure 4.22 shows two examples of such distributions, one with f_0 a double power law and the other an offset Maxwellian.Narrower beams can be modelled with higher values of N.

An advantage of particle distributions of the form in (4.52) is that they have well-known and relatively simple expansions in Legendre polynomials. For $N = 2$, it may be shown that

$$
\begin{aligned}
f(p,\alpha) &= f_0(p)\left[1 + r(p)\cos^5\alpha\right] \\
&= f_0(p)\left[1 + \frac{3}{7}r(p)P_1(\cos\alpha) + \frac{4}{9}r(p)P_3(\cos\alpha) + \frac{8}{63}r(p)P_5(\cos\alpha)\right],
\end{aligned}
\tag{4.53}
$$

with

$$
f_1(p) = \frac{3}{7}r(p)f_0(p), \tag{4.54}
$$

$$
f_3(p) = \frac{4}{9}r(p)f_0(p), \tag{4.55}
$$

$$
f_5(p) = \frac{8}{63}r(p)f_0(p). \tag{4.56}
$$

The 3D resonance of such a $\cos^5\alpha$ distribution is now investigated using the technique of separating the relative contributions of electrons introduced in Chapter 3. Beginning with the expressions for γ_ℓ from Equation (3.7),

$$
\begin{aligned}
\gamma_1(k) &= \frac{2\pi^2 e^2 \omega_p^2 m^2}{k^3}\left\{f_1(p_\phi) - \frac{1}{p_\phi}\int_{p_\phi}^{\infty} dp\; f_1(p)\right\}, \\
\gamma_3(k) &= \frac{2\pi e^2 \omega_p^2 m^2}{k^3}\left\{f_3(p_\phi) + \frac{3}{p_\phi}\int_{p_\phi}^{\infty} dp\; f_3(p) - \frac{15p_\phi}{2}\int_{p_\phi}^{\infty} dp\; \frac{f_3(p)}{p^2}\right\}, \\
\gamma_5(k) &= \frac{2\pi e^2 \omega_p^2 m^2}{k^3}\left\{f_5(p_\phi) + \frac{105p_\phi}{4}\int_{p_\phi}^{\infty} dp\; \frac{f_5(p)}{p^2} - \frac{315p_\phi^3}{8}\int_{p_\phi}^{\infty} dp\; \frac{f_5(p)}{p^4}\right. \\
&\qquad \left. - \frac{15}{8p_\phi}\int_{p_\phi}^{\infty} dp\; f_5(p)\right\}.
\end{aligned}
\tag{4.57}
$$

If f_0 is a double power law of the form (3.14), viz

$$
f_0(p) = \begin{cases} Ap^a & p < p_b \\ Bp^{-b} & p > p_b \end{cases} \tag{4.58}
$$

with $Ap_b^a = Bp_b^{-b}$, then for $p < p_b$ the factors in (4.57) become

$$\gamma_1(k) \propto \frac{A}{k^3}\frac{3}{7}\left\{ -p_\phi^a + \frac{1}{a+1}\frac{1}{p_\phi}\left(p_b^{a+1} - p_\phi^{a+1}\right) + \frac{1}{b-1}\frac{1}{p_\phi}p_b^{a+1} \right\} \tag{4.59}$$

$$\begin{aligned}\gamma_3(k) \propto \frac{A}{k^3}\frac{4}{9}\Bigg\{ & -p_\phi^a - \frac{3}{a+1}\frac{1}{p_\phi}\left(p_b^{a+1} - p_\phi^{a+1}\right) - \frac{3}{b-1}\frac{1}{p_\phi}p_b^{a+1} \\ & + \frac{15p_\phi}{2}\left[\frac{1}{a-1}\left(p_b^{a-1} + p_\phi^{a-1}\right) - \frac{1}{b+1}p_b^{a-1}\right]\Bigg\}\end{aligned} \tag{4.60}$$

$$\begin{aligned}\gamma_5(k) \propto \frac{A}{k^3}\frac{8}{63}\Bigg\{ & -p_\phi^a - \frac{105p_\phi}{4}\left[\frac{1}{a-1}\left(p_b^{a-1} - p_\phi^{a-1}\right) - \frac{1}{b+1}p_b^{a-1}\right] \\ & + \frac{315}{8}p_\phi^3\left[\frac{1}{a-3}\left(p_b^{a-3} - p_\phi^{a-3}\right) - \frac{1}{b+3}p_b^{a-3}\right] \\ & + \frac{15}{8p_\phi}\left[\frac{1}{a+1}\left(p_b^{a+1} - p_\phi^{a+1}\right) - \frac{1}{b-1}p_b^{a+1}\right]\Bigg\}.\end{aligned} \tag{4.61}$$

Then, in a similar manner to the P_1 analysis in Chapter 3, (4.59-4.61) can be written as

$$\gamma_1(k) \propto \frac{1}{k^3}\Big(-\gamma_{1,iso} + \gamma_{1,a1} + \gamma_{1,a2} + \gamma_{1,a3} + \gamma_{1,a4}\Big) \tag{4.62}$$

$$\gamma_3(k) \propto \frac{1}{k^3}\Big(-\gamma_{3,iso} - \gamma_{3,pos} + \gamma_{3,a1} + \gamma_{3,a2} + \gamma_{3,a3} + \gamma_{3,a4}\Big) \tag{4.63}$$

$$\gamma_5(k) \propto \frac{1}{k^3}\Big(-\gamma_{5,iso} - \gamma_{3,pos} + \gamma_{5,a1} + \gamma_{5,a2} + \gamma_{5,a3} + \gamma_{5,a4}\Big) \tag{4.64}$$

$$\tag{4.65}$$

where $\gamma_{\ell,iso}$ and $\gamma_{\ell,pos}$ contribute to damping and $\gamma_{\ell a1-a4}$ are defined in the same way as in Chapter 3, and have the interpretation given in Table 4.1

For $f_0(p)$ a double power law distribution centred at $p_b = 10p_e$, the relative contributions to γ_ℓ are plotted in Figure 4.23. Again, one can see that electrons from the higher speed tail of the electron distribution contribute significantly to Langmuir wave growth; in particular $\gamma_{n,a3}$ is relatively large for $p < p_b$. Figure 4.24 shows the sum of the positive and negative factors of each γ_ℓ separately. The regions of p where the positive (red) factors are larger than the negative (blue) factors are markedly different than would be expected in a 1D consideration of wave growth; interestingly, the 3D resonance effect here means that some parts of γ_3 and γ_5 are negative.

The sum $\gamma_1 + \gamma_3 + \gamma_5$ is shown in Figure 4.25. It is bounded from above and below in p_ϕ, which is different behaviour than the 1D resonance condition

Component	Represents contribution to wave growth from electrons in the region:
$\gamma_{\ell,a1}$	from p_ϕ to $p_b - \Delta p_b$, i.e. particles on the lower speed side of the beam, away from the peak
$\gamma_{\ell,a2}$	from $p_b - \Delta p_b$ to p_b, i.e. close to the peak on the lower speed side
$\gamma_{\ell,a3}$	from p_b to $p_b + \Delta p_b$, i.e. particles close to the peak on the higher speed side
$\gamma_{\ell,a4}$	from $p_b + \Delta p_b$ to ∞, i.e. particles in the high speed tail of the distribution

Table 4.1: Definitions and interpretation of the $\gamma_{\ell a1-a4}$ factors

would suggest. The distribution has a 1D derivative $\partial f/\partial v > 0$ and so $\gamma > 0$ for $p < 10p_e$, but the growth rate is negative for $p < 6.7p_e$ in this case. for the fully 3D calculation.

The $cos^5\alpha$ distribution is also investigated using the numerical code for a Langmuir wave distribution that is flat and fixed in time. Again, significant diffusion in angle occurs with comparably little diffusion in $p_\parallel$, which can be seen in Figure 4.26. This demonstrates that an electron beam distribution that is a realistic approximation of data taken in the interplanetary medium should undergo the 3D resonance and diffusion effects that are described in Chapter 3 and this chapter.

4.8 Discussion and conclusions

The numerical method and code described in this chapter have great potential to understand electron-Langmuir wave interactions, especially to explore fully 3D aspects numerically and demonstrate the importance of 3D effects. A major step towards such a treatment was demonstrated in this chapter, with significant progress in testing isotropic cases and some higher order distributions. The numerical results available demonstrate that the relaxation of a fast electron stream is qualitatively and quantitatively different to the 1D picture of plateau formation. Instead, major broadening in pitch angle occurs, in addition to diffusion in speed $\parallel$ to $\mathbf{B}$, with some particles diffused to the opposite direction. Furthermore, the diffusion in $p_{\parallel}$ occurs, to a smaller degree, on the higher velocity side of the peak as well as on the lower.

The 3D resonance results explored in this chapter may contribute to the theoretical resolution of Sturrock's Dilemma discussed in Chapter 1. Diffusion to higher speeds as well as lower will contribute to the time-of-flight advection effect, where faster particles outrun slower particles so that as the beam reforms as it moves through the corona. When this advection effect is considered in addition to stochastic growth effects, a qualitative argument can be made that the beam should survive out to interplanetary distances. Furthermore, the diffusion in pitch angle may help explain the broad features seen in Type III bursts. The pitch angle broadening will be balanced by magnetic focusing, which has been invoked to justify a 1D approximation for the electron beam. Also, more diffusion in angle means that the 1D quasilinear relaxation asymptotic state, which is the plateau distribution that is stable to the growth of Langmuir waves, does not form in the same way.

Comparison between these results and those of *Lee et al.* [2019] is instructive. Those authors conducted a Particle in Cell simulation using 2 spatial dimensions and a 3D velocity space and compared to a 2D weak turbulence simulation (Figure 4.27). Whereas the 2D quasilinear results showed a narrow plateau forming, the PiC 3D electron velocity distribution function evolves in a similar way to that described in this chapter - pitch angle diffusion appears to occur and broaden the beam perpendicular to the magnetic field with increasing time. These results are not directly comparable, since they use a PiC method and 2D wavenumber space, versus a homogeneous 3D quasilinear theory. However, the existence of pitch angle diffusion-like evolution in 3D velocity

space of the electron distribution supports the results of Chapters 3 and 4 of this thesis.

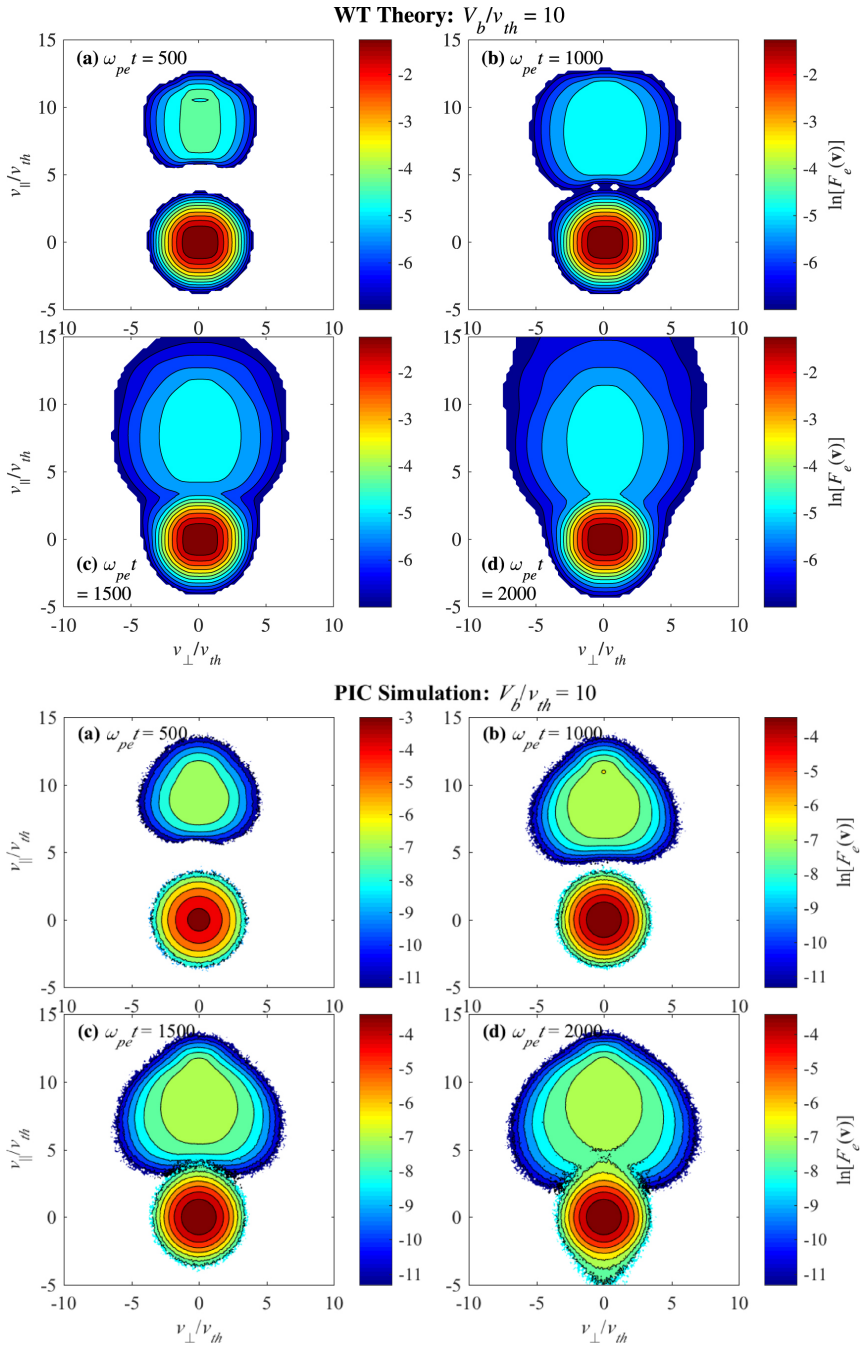

Figure 4.27: Results from [*Lee et al.*, 2019] - 2D quasilinear theory simulation above, with 2.5D PiC below. Both figures depict the electron velocity distribution function (VDF) $F_e(v)$ vs. $v_{\perp}/v_e$ and $v_{//}/v_e$, for four different time steps corresponding to $\omega_p t = 500$, 1000, 1500, and 2000.

Further development of the code and application to a moving electron

stream will determine whether 3D effects and pitch angle diffusion play a major role in the real corona, as we expect they will. With the monotonic advection scheme [*Kontar*, 2001; *Li et al.*, 2002] combined with the solid physical foundation of the OPL electron density model described in Chapter 2 it should be possible to quantitatively consider the time of flight effects. A fully developed code should be able to handle arbitrary initial electron distributions close to the solar corona, decompose them into their Legendre components, and follow their evolution with their excited Langmuir wave populations. Such results will be very timely given the opportunity to compare them against newly released and future data from the Parker Solar Probe and Solar Orbiter.

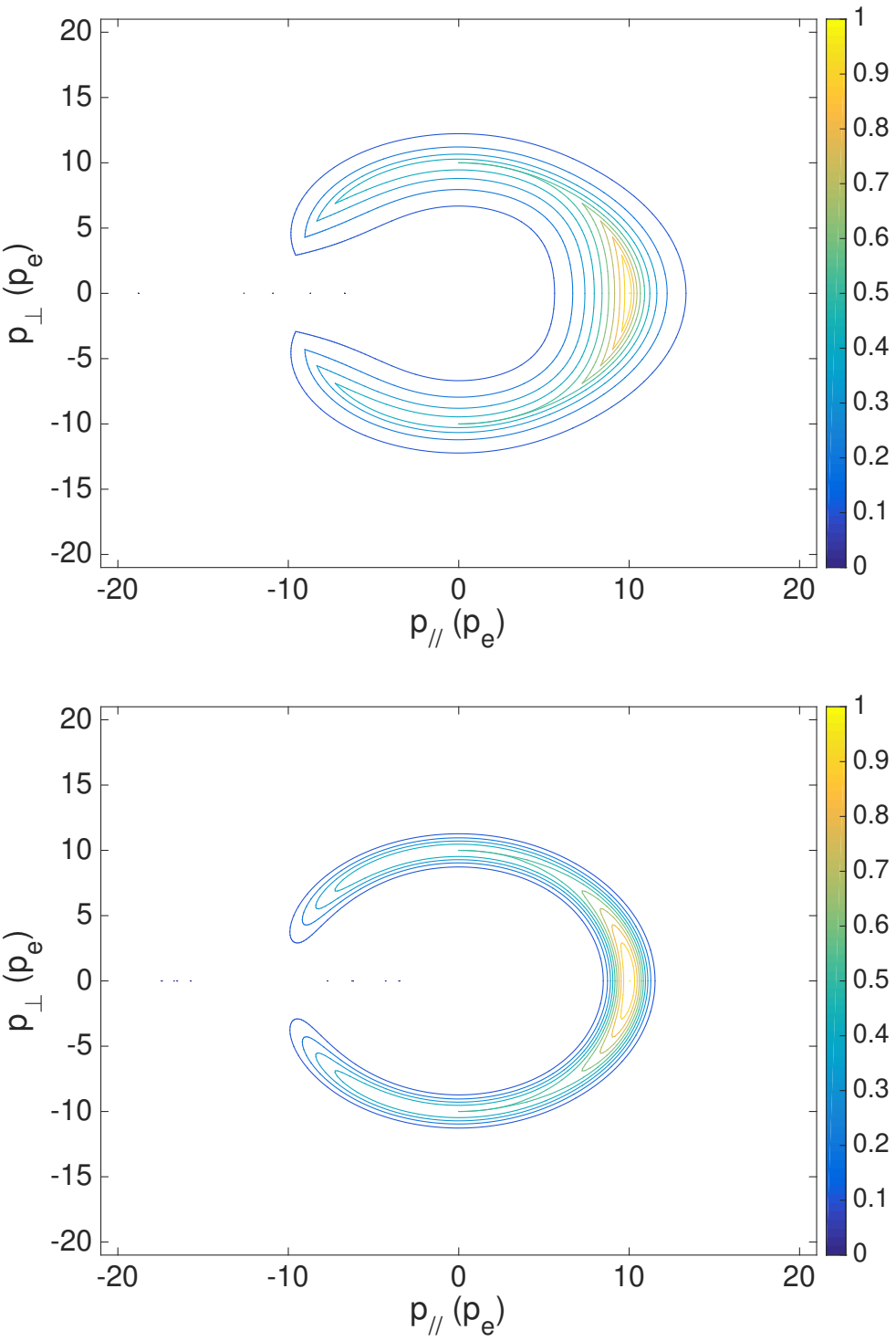

Figure 4.22: An electron distribution (4.52), a) with f_0 in the form of a peaked double power law and $N = 2$, and b) with f_0 as an offset Maxwellian centred at $p = 10p_e$. The contour levels are evenly spaced at $0.1f_D$ apart.

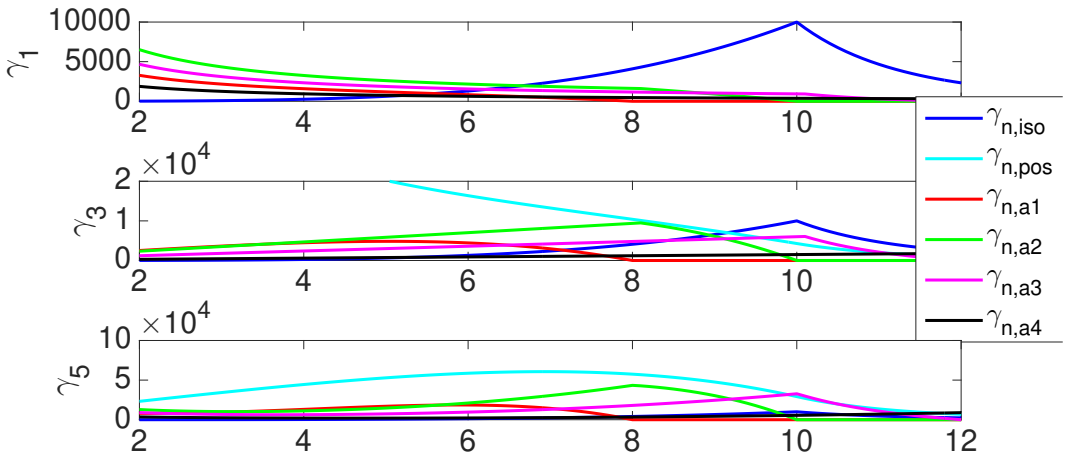

Figure 4.23: The relative contributions to γ_1, γ_3 and γ_5, showing the 3D resonance condition is again different to 1D. Here $p_0 = 10$, $a = 4$ and $b = 8$.

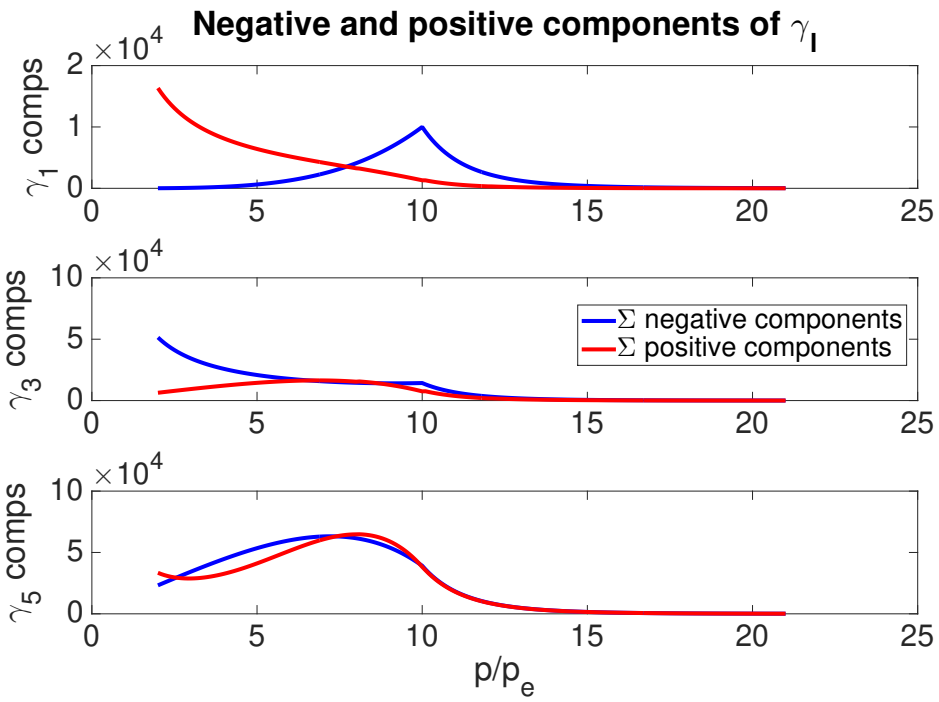

Figure 4.24: Negative (blue) and positive parts (red) of the γ_ℓ factors in the case of $f(p, \alpha) = f_0(p)(1 + \cos^5 \alpha)$, with $f_0(p)$ a double power law of the form (3.14), with $p_0 = 10$, $a = 4$ and $b = 8$. γ_ℓ contributes to positive growth in the $p_\parallel$ direction when the positive parts are greater than the negative.

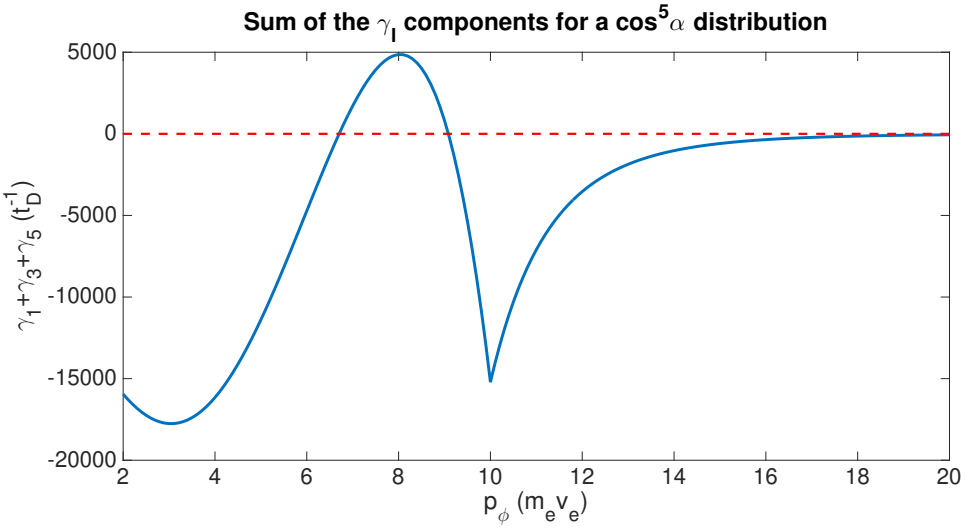

Figure 4.25: The sum $\gamma_L(\alpha = 0) = \gamma_1 + \gamma_3 + \gamma_5$, for the same $f(p, \alpha)$ and growth rate in Figure 4.24. The growth rate in the $p_\parallel$ direction is positive for a region $6.7 \leq p_\phi/p_e \leq 9.1$ for this distribution, suggesting a narrower region of growth for the waves.

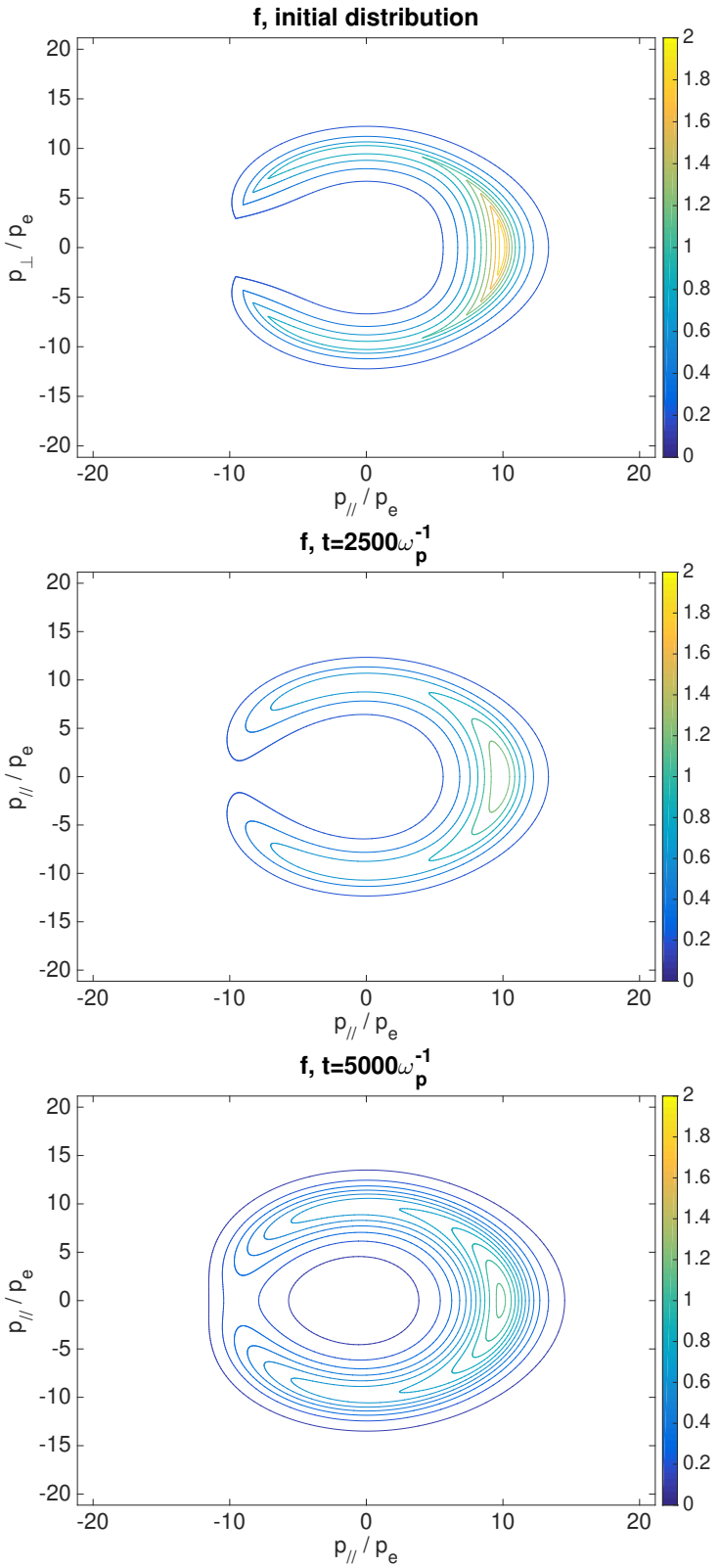

Figure 4.26: Evolution of the $\cos^5 \alpha$ distribution as described in Equation 4.52 with $N = 2$ with $r(p) = 1$ and $f_0(p)$ a double power law with $a = 4$ and $b = 8$. The particles diffuse most significantly in angle, with some broadening in $p_\parallel$.

Chapter 5

Conclusions and future work

This thesis put forward new foundations for modelling the 3D interactions of electrons and Langmuir waves, both in general and in Type III solar radio bursts, and for reconsidering the spatial evolution and origin of the solar corona in general. A physically significant and empirically well-supported model for the electron density profile was described in Chapter 2, and in Chapters 3 and 4 the need for a fully 3D consideration of the electron beam-Langmuir wave interaction (the basis for the kinetic beam instability and the underlying mechanism for plasma emission) is demonstrated.

In Chapter 2 the advantages of the offset power law model for the electron density profile of the solar corona were explained. It was found by fitting published data sets that this model works remarkably well, despite its simplicity, and the fits can be interpreted in the following way. Overwhelmingly, the radial offset r_0 was found to be very close to $1.0R_S$, which implies that the bulk outflow of plasma in the solar corona originates close to the photosphere. Furthermore, the result that the average power law index $\langle\alpha\rangle = 2.4$ implies acceleration of the solar wind. Using conservation of total electron number, this model fit implies a velocity profile like $v \propto (r - r_0)^{0.4}$, which is consistent with several sets of observational data as well as existing models, including the widely used Parker model.

Chapter 3 is a detailed study of the quasilinear wave equation expanded in Legendre polynomials, demonstrating that resonance between electrons and Langmuir waves is fundamentally different in the 3D picture compared to the 1D picture. Whereas in 1D the resonance is one-to-one between particles with velocity v_ϕ and waves with wavenumber k, in 3D waves with wavenumber k may be resonant with electrons moving with $v > v_\phi$. One of the implications of this is that the commonly used, straightforward, consideration of the sign of

gradient of the 1D electron distribution, $\partial f(v)/\partial v$, cannot be relied upon to determine stability of electron distributions. In fact, distributions may be unstable in 3D that would be considered stable in 1D, and conventional unstable distributions induce Langmuir wave growth in different regions of phase space than the 1D picture predicts.

Chapter 4 developed a numerical scheme for solving the 3D axisymmetric equations and in so doing further explored the problem of the electron beam-Langmuir wave interaction. The numerical scheme was tested first using an isotropic thermal Maxwellian electron distribution and testing the development of waves. The waves, as expected, evolved from a suprathermal to a thermal level, with the thermal level being very stable. An isotropic gap distribution for the particles was then introduced, and waves evolved towards the long-predicted theoretical asymptotic state. This case proved useful both as a test of the code and to observe the evolution of the waves in time, and it was seen that the waves grew very quickly, achieving the asymptoptic level at around $225\omega_p^{-1}$. A P_1 particle distribution was then allowed to evolve along with the wave distribution. Diffusion of the particles and growth of the waves was seen, with diffusion in pitch angle supporting results from Chapter 3. However, just as the backreaction on the particles begins to modulate the wave growth, a numerical instability is encountered in the code which is yet unresolved. In attempts to resolve this problem, further runs were made that fix the level of waves in time. These provide further support for the idea put forward in Chapter 3 that 3D resonance should imply more diffusion in putch angle than previously expected.

5.1 Future work

5.1.1 Electron density profiles

In Chapter 2 it was found that some data sets were best fit with two power laws in different regions. This was interpreted as the line of sight measurement projecting through two different plasma environments. Further data, especially in-situ data, could be used to test this interpretation.

The analysis in Chapter 2 showed that fits to the OPL density model to white light and spectroscopic data yielded higher values of the power law index α (i.e. steeper density profiles) than those data derived from radio burst obser-

vations. This was explained as pre-flare activity enhancing the plasma ahead of the radio burst exciter beam, which has strong implications for determining properties of the burst. Further work can be done using density profiles derived from Type III bursts, for example using the technique described by *McCauley et al.* [2018] with data from the Murchison Widefield Array. If the interpretation that pre-flare activity increases the electron density ahead of Type III bursts holds true, calculations should be carried out in order to estimate the error in previous calculations of Type III source heights, and to what degree this effect may reduce the need to appeal to ducting. A reference is made in Chapter 2 to the possible underestimation of the speed of Type III exciter beams due to such enhancement; a more thorough calculation of this effect is possible using the OPL model and radio burst data. Further electron density data at low helioaltitudes will be in abundance due to the Parker Solar Probe and Solar Orbiter data releases.

5.1.2 Advection and density inhomogeneity

The code developed in Chapter 4 includes a useful and numerically tested scheme known to describe electron transport well [*Kontar*, 2001]. Advection was included in the numerical design (such that it may be included once the quasilinear interaction was working reliably for all cases) but was outside the scope of this thesis. In previous (albeit 1D) numerical explorations of this problem, advection effects are expected to be very important in resolving Sturrock's Dilemma and determining the shape of the electron beam later in its life. Further, since the 3D resonance condition implies more diffusion in pitch angle than previously considered, a reconsideration is needed of the balance between spatial spreading of the beam from this effect and magnetic focusing to smaller α. Pitch angle diffusion due to the 3D wave-particle interactions may potentially explain why, despite the magnetic focusing effect tending to drive electron beams towards a 1D structure, Type III beams often have a wide angular profile in the data.

Density inhomogeneities should also be introduced, as was done in quasi 1D simulations e.g. *Li et al.* [2002, 2008]. The right balance of Stochastic Growth Theory effects from density variations, time of flight restructuring of the beam, and Langmuir waves lost to nonlinear processes can then be tested against in situ electron distribution data.

5.1.3 Numerical code

We have shown promising tests and interesting cases that the numerical code can handle. However in its current form a full, long duration solution of the coupled electron-Langmuir wave situation with time-varying waves is not possible because of a singularity developing, causing the code to crash. Fixing this numerical bug is the immediate next step in this work - to explore the full evolution of waves with 3D and relativistic growth conditions and their back-reaction on the electrons.

In its present form, the numerical model is able to handle the early growth of waves, but more work and attention needs to be paid to the period where the waves begin to significantly back-react on particles. In 3D as in 1D, the growth of waves should start to be modulated by the diffusing electron beam. This part of the simulation is not yet working reliably, but with this element in place, it is expected that novel 3D effects develop.

5.1.4 Extrapolated wave distribution

An investigation into the diffusion of particles could be conducted with the current version of the code by using a more anisotropic (therefore, with a higher order Legendre expansion) Langmuir wave distribution fixed in time. Beginning with an initial particle distribution of the form (3.14), i.e. a P_1 electron distribution with a double power law form, one can calculate the initial growth rate $\gamma_L(k, \alpha)$. By making some simplifying assumptions, namely that the growth rate dominates the spontaneous emission ($\alpha_L \ll \gamma_L$) and that initially the waves grow without effecting the particle distribution significantly, then we arrive at a first order approximation for the initial growth of waves with time,

$$N_L(k, \alpha, t) = N_0(k, \alpha) e^{\gamma(k,\alpha)t}. \tag{5.1}$$

With (5.1) as a basic guide to the early stage of wave growth, we can use the foregoing fixed-wave investigations to estimate a level of growth where particle diffusion will proceed at a significant rate. I.e., for this choice of initial particle distribution and with the plasma parameters used in this chapter, where $N_L \approx 2000 N_D$.
Figure 5.1 is a contour plot of $\gamma(k, \alpha)$ for the DPL distribution. Figure 5.2 shows $N_L(t = 1000\omega_p^{-1})$, such the level of waves reaches $2000 N_D$. The distribution is clearly quite narrow and anisotropic.

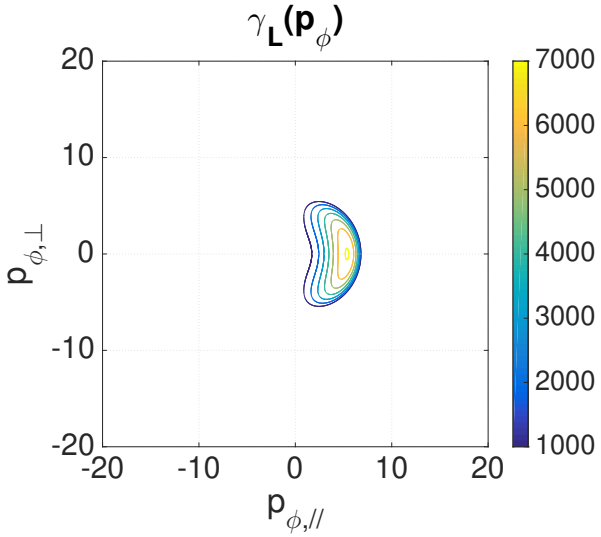

Figure 5.1: Contour plot of $\gamma_L(p_\phi)$.

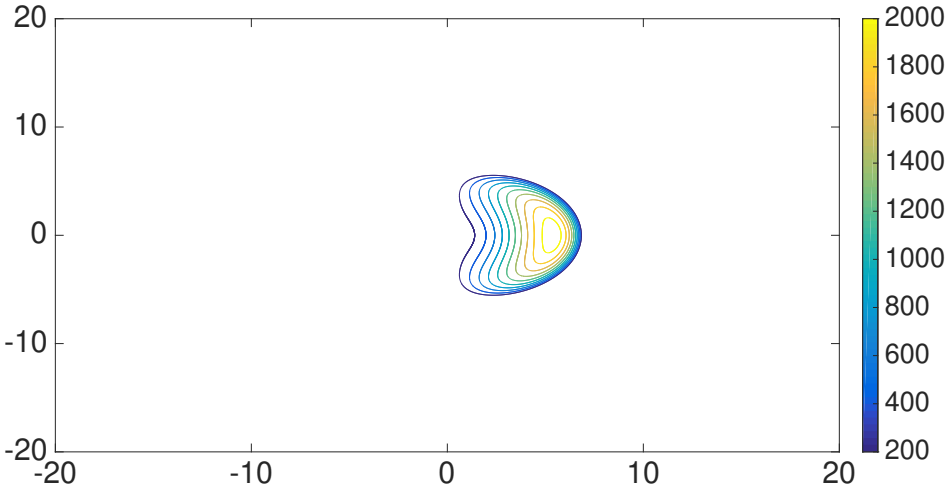

Figure 5.2: Wave distribution extrapolated from the growth rate in Figure (5.1) at time $t = 1000\omega_p^{-1}$.

Now, we could seek to replicate the distribution in Figure 5.2 by eye with a Maxwellian distribution of waves, expand that Maxwellian in Legendre polynomials and fix the Langmuir wave distribution at those values, and evolve $f(\boldsymbol{p}, t)$. This would test whether the numerical problem comes from one of the higher order Langmuir wave components, and if it proceeds without encountering the singularity problem, will be interesting to see the resonance and diffusion effects on the particles.

5.1.5 Radio emission

The next logical step for a numerical simulation code which successfully describes 3D axisymmetric evolution of electrons and Langmuir waves is to include the nonlinear processes that result in radio emission. In 1D, such studies have been carried out successfully, e.g. in *Li and Cairns* [2014] which used a population of hot electrons in the low corona and followed their evolution out to higher heliolatitudes. In addition to predicting Type III burst dynamic spectra, this step would be interesting from an electron beam stability perspective, since radio emission reduces the Langmuir wave population, which must influence the development of the beam-plasma-wave structure.

The ultimate goal for this research, which this thesis has provided a motivation and a major foundation for, is a fully 3D, relativistically correct simulation of the dynamic spectrum of Type III radio bursts and the properties of the associated electron beams and Langmuir waves from the Sun to the Earth's orbit. For the first stage of plasma emission, this would include incorporation of fully 3D electron beam-Langmuir wave physics, stability considerations of beams, time of flight beam reformation effects, density inhomogeneities and stochastic growth theory, and nonlinear effects such as scattering and coalescence. In terms of the radio wave propagation, effects such as refraction in the solar corona and polarisation of the resulting radio emission should be explored further.

Appendix A

Block tridiagonal decomposition

The quasilinear electron equation can be written in the following matrix form, as shown in Chapter 4 Equation 4.35.

$$\begin{pmatrix} \mathbf{A}^n_{i2} & \mathbf{C}^n_{i2} & & & & \\ \mathbf{B}^n_{i3} & \mathbf{A}^n_{i3} & \mathbf{C}^n_{i3} & & & \\ & \mathbf{B}^n_{i4} & \mathbf{A}^n_{i4} & \mathbf{C}^n_{i4} & & \\ & & \ddots & \ddots & \ddots & \\ & & & \mathbf{B}^n_{ij_{max}-1} & \mathbf{A}^n_{ij_{max}-1} \end{pmatrix} \begin{pmatrix} \boldsymbol{f}^{n+1}_{i2} \\ \boldsymbol{f}^{n+1}_{i3} \\ \boldsymbol{f}^{n+1}_{i4} \\ \vdots \\ \boldsymbol{f}^{n+1}_{ij_{max}-1} \end{pmatrix} = \begin{pmatrix} \boldsymbol{\eta}^n_{i2} \\ \boldsymbol{\eta}^n_{i3} \\ \boldsymbol{\eta}^n_{i4} \\ \vdots \\ \boldsymbol{\eta}^n_{ij_{max}-1} \end{pmatrix}, \tag{A.1}$$

where

$$\begin{aligned} \mathbf{A}^n_{ij} &= 1 + \mathbf{\Lambda}^n_{ij-1} + 2\mathbf{\Lambda}^n_{ij} + \mathbf{\Lambda}^n_{ij+1}, \\ \mathbf{B}^n_{ij} &= -[\mathbf{\Lambda}^n_{ij-1} + \mathbf{\Lambda}^n_{ij}], \\ \mathbf{C}^n_{ij} &= -[\mathbf{\Lambda}^n_{ij} + \mathbf{\Lambda}^n_{ij+1}]. \end{aligned} \tag{A.2}$$

The block-tridiagonal inversion procedure for this system, adapted from *Varah* [1972], is an efficient way of solving this system. Instead of naively inverting the large matrix, in (A.1), we use the property that block tridiagonal matrices can be factored into a product of lower $\mathbf{L}$ and upper $\mathbf{U}$ triangular matrices, a process called LU decomposition. The steps in this process are as follows:

Firstly the matrix on the left of (A.1) is LU factorised as follows. This matrix can be written as *Varah* [1972]

$$\begin{pmatrix} \mathbf{A}^n_{i2} & \mathbf{C}^n_{i2} & & \\ \mathbf{B}^n_{i3} & \mathbf{A}^n_{i3} & \mathbf{C}^n_{i3} & \\ & \ddots & \ddots & \ddots \\ & & \mathbf{B}^n_{ij_{max}-1} & \mathbf{A}^n_{ij_{max}-1} \end{pmatrix} = \mathbf{L}^n_i \mathbf{U}^n_i, \tag{A.3}$$

where

$$\mathbf{L}_i^n = \begin{pmatrix} \mathbf{D}_{i2}^n & & & \\ \mathbf{B}_{i3}^n & \mathbf{D}_{i3}^n & & \\ & \ddots & \ddots & \\ & & \mathbf{B}_{ij_{max}-1}^n & \mathbf{D}_{j_{max}-1} \end{pmatrix}, \tag{A.4}$$

$$\mathbf{U}_i^n = \begin{pmatrix} \mathbf{I}_2 & \boldsymbol{\beta}_{i2}^n & & \\ & \mathbf{I}_3 & \boldsymbol{\beta}_{i3}^n & \\ & & \ddots & \ddots \\ & & & \mathbf{I}_{j_{max}-1} \end{pmatrix} \tag{A.5}$$

and

$$\mathbf{D}_{i2}^n = \mathbf{A}_{i2}^n, \qquad \boldsymbol{\beta}_2 = \left(\mathbf{A}_{i2}^n\right)^{-1}\mathbf{C}_i^n 2, \tag{A.6}$$

$$\mathbf{D}_{ik}^n = \mathbf{A}_{ik}^n - \mathbf{B}_{ik}^n\boldsymbol{\beta}_{i-1}, \qquad \text{for } k = 2, ..., j_{max} - 1, \tag{A.7}$$

$$\boldsymbol{\beta}_{ik}^n = \left(\mathbf{A}_{ik}^n\right)^{-1}\mathbf{C}_{ik}^n, \qquad \text{for } k = 2, ..., j_{max} - 2. \tag{A.8}$$

Now introducing the dummy variable $\mathbf{Y}$, and writing the column vector of the $\boldsymbol{f}_{ij}^{n+1}$ components we are solving for as $\mathbf{F}_i^{n+1}$ and the column vector of the $\boldsymbol{\eta}_{ij}^n$ terms representing the right hand side of (4.35) as $\mathbf{Z}_i^n$, so that

$$\boldsymbol{F}_i^{n+1} = \begin{pmatrix} \boldsymbol{f}_{i2}^{n+1} \\ \vdots \\ \boldsymbol{f}_{ij_{max}-1}^{n+1} \end{pmatrix} \qquad \boldsymbol{Z}_i^n = \begin{pmatrix} \boldsymbol{\eta}_{i2}^n \\ \vdots \\ \boldsymbol{\eta}_{ij_{max}-1}^n \end{pmatrix}, \tag{A.9}$$

and the system can now be split into

$$\mathbf{L}_i^n\mathbf{Y}_i^n = \boldsymbol{Z}, \qquad \mathbf{U}_i^n\boldsymbol{F}_i^n = \mathbf{Y}_i^n, \qquad \text{where } \mathbf{Y}_i^n = \begin{pmatrix} \mathbf{y}_{i2}^n \\ \vdots \\ \mathbf{y}_{ij_{max}-1}^n \end{pmatrix} \tag{A.10}$$

The first step here is to invert the $\mathbf{L}_i^n$ matrix to solve for $\mathbf{Y}_i^n$. As $\mathbf{L}_i^n$ is a lower triangular matrix by construction, there is an efficient algorithm to solve the leftmost equation in (A.10), namely

$$\mathbf{y}_{i2}^n = \left(\mathbf{D}_{i2}^n\right)^{-1}\boldsymbol{\eta}_{i2}^n \tag{A.11}$$

$$\mathbf{y}_{ij}^n = \left(\mathbf{D}_{ij}^n\right)^{-1}(\boldsymbol{\eta}_{ij}^n - \mathbf{B}_{ij}^n\mathbf{y}_{j-1}), \qquad j = 2, ..., j_{max} - 1. \tag{A.12}$$

Since we now have the vector $\mathbf{Y}_i^n$, the upper triangular matrix $\mathbf{U}_i^n$ is inverted to solve the middle equation in (A.10) for the particle distribution $\mathbf{F}_i^n$. In this

project we chose the backwards-inversion algorithm for efficiency, i.e. we first find $\mathbf{f}_{ij_{max}-1}^{n+1}$ and then the terms $\mathbf{f}_{ij}^{n+1}$ for decreasing j. Explicitly, the particle equation terms are given by

$$\boldsymbol{f}_{ij_{max}-1}^{n+1} = \mathbf{y}_{j_{max}-1} \tag{A.13}$$

$$\boldsymbol{f}_{ij}^{n+1} = \mathbf{y}_j - \boldsymbol{\beta}_j \mathbf{y}_{j+1}, \qquad j = j_{max}-2,\ j_{max}-3, ..., 2. \tag{A.14}$$

Bibliography

Abbo, L., L. Ofman, S. K. Antiochos, V. H. Hansteen, L. Harra, Y. K. Ko, G. Lapenta, B. Li, P. Riley, L. Strachan, R. von Steiger, and Y. M. Wang (2016), Slow Solar Wind: Observations and Modeling, *Space Sci. Rev.*, *201*(1-4), 55–108, doi:10.1007/s11214-016-0264-1. 34, 45

Alfvén, H. (1939), On the Motion of Cosmic Rays in Interstellar Space, *Physical Review*, *55*(5), 425–429, doi:10.1103/PhysRev.55.425. 15

Allen, C. W. (1947), Interpretation of Electron Densities from Corona Brightness, *Mon. Not. Roy. Astron. Soc.*, *107*, 426, doi:10.1093/mnras/107.5-6.426. 37, 41

Appert, K., T. M. Tran, and J. Vaclavik (1976), Two-dimensional quasi-linear evolution of the electron-beam-plasma instability, *Physical Review Letters*, *37*, 502–504, doi:10.1103/PhysRevLett.37.502. 29, 55

Appleton, E. V. (1945), Departure of Long-Wave Solar Radiation from Black-Body Intensity, *Nature*, *156*(3966), 534–535, doi:10.1038/156534b0. 1

Appleton, E. V., and J. S. Hey (1946), Circular Polarization of Solar Radio Noise, *Nature*, *158*(4010), 339, doi:10.1038/158339a0. 1

Aschwanden, M. J. (2004), *Physics of the Solar Corona. An Introduction*, Springer Berlin Heidelberg. 3

Avrett, E. H., and R. Loeser (2008), Models of the Solar Chromosphere and Transition Region from SUMER and HRTS Observations: Formation of the Extreme-Ultraviolet Spectrum of Hydrogen, Carbon, and Oxygen, *The Astrophysical Journal Supplement Series*, *175*(1), 229–276, doi:10.1086/523671. 38, 39, 41, 42, 47

Bai, T., H. S. Hudson, R. M. Pelling, R. P. Lin, R. A. Schwartz, and T. T. von Rosenvinge (1983), First-order Fermi acceleration in solar flares as a mechanism for the second-step acceleration of prompt protons and relativistic electrons, *Astrophys. J.*, *267*, 433–441, doi:10.1086/160881. 15

Battaglia, M., and Benz, A. O. (2008), Observational evidence for return currents in solar flare loops, *A&A*, *487*(1), 337–344, doi:10.1051/0004-6361:200809418. 15

Baumbach, S. (1937), Strahlung, ergiebigkeit und elektronendichte der sonnenkorona, *Astronomische Nachrichten*, *263*(6), 121–134, doi:10.1002/asna.19372630602. 37, 41

Benz, A. O. (1993), *Plasma astrophysics: Kinetic processes in solar and stellar coronae*, vol. 184, Springer Netherlands, Dordrech, doi:10.1007/978-94-011-2064-7. 1, 15

Billings, D. E. (1966), *A guide to the solar corona*, New York: Academic Press. 35

Cairns, I. H. (1984), Arguments for fundamental emission by the parametric process L $\rightarrow$ T + S in interplanetary type III bursts., in *Achievements of the International Magnetospheric Study (IMS)*, *ESA Special Publication*, vol. 217, edited by B. Battrick, E. Rolfe, and J. G. Roederer, pp. 281–284. 54

Cairns, I. H. (1989), Electrostatic wave generation above and below the plasma frequency by electron beams, *Physics of Fluids B*, *1*, 204–213, doi:10.1063/1.859088. 54

Cairns, I. H., and S. F. Fung (1988), Growth of electron plasma waves above and below f_p in the electron foreshock, *Journal of Geophysical Research*, *93*(A7), 7307–7317, doi:10.1029/JA093iA07p07307. 54

Cairns, I. H., and D. B. Melrose (1985), A theory for the $2f_p$ radiation upstream of the earth's bow shock, *J. Geophys. Res.*, *90*(A7), 6637–6640, doi:10.1029/JA090iA07p06637. 87

Cairns, I. H., and P. A. Robinson (1995), Ion Acoustic Wave Frequencies and Onset Times during Type III Solar Radio Bursts, *Astrophys. J.*, *453*, 959, doi:10.1086/176456. 9

Cairns, I. H., and P. A. Robinson (1998), Constraints on nonlinear and stochastic growth theories for type III solar radio bursts from the corona to 1 AU, *The Astrophysical Journal*, *509*(1), 471–481, doi:10.1086/306486. 21, 24, 25, 54, 56

Cairns, I. H., V. V. Lobzin, A. Warmuth, B. Li, P. A. Robinson, and G. Mann (2009), Direct Radio Probing and Interpretation of the Sun's Plasma Density Profile, *Astrophys. J. Lett.*, *706*(2), L265–L269, doi:10.1088/0004-637X/706/2/L265. 36, 37, 38, 44, 47, 48

Cairns, I. H., B. Li, and J. Schmidt (2017), Importance of kappa distributions to solar radio bursts, in *Kappa Distributions: Theory and Applications in Plasmas*, edited by G. Livadiotis, chap. 14, pp. 549–567, Elsevier, Amsterdam. 54

Carmichael, H. (1964), A Process for Flares, in *NASA Special Publication*, vol. 50, p. 451. 15

Cranmer, S. R. (2009), Coronal Holes, *Living Reviews in Solar Physics*, *6*(1), 3, doi:10.12942/lrsp-2009-3. 3, 5, 34

De Moortel, I., and P. Browning (2015), Recent advances in coronal heating, *Philosophical Transactions of the Royal Society of London Series A*, *373*(2042), 20140,269–20140,269, doi:10.1098/rsta.2014.0269. 4

DeForest, C. E., T. A. Howard, and D. J. McComas (2013), Tracking Coronal Features from the Low Corona to Earth: A Quantitative Analysis of the 2008 December 12 Coronal Mass Ejection, *Astrophys. J.*, *769*(1), 43, doi:10.1088/0004-637X/769/1/43. 44

Drummond, W. E., and D. Pines (1962), Nonlinear stability of plasma oscillations, *Nuclear Fusion Suppl.*, *Part 3*, 1049–1055. 54

Dulk, G. A. (1985), Radio emission from the sun and stars., *Ann. Rev. Astron. Astrophys.*, *23*, 169–224, doi:10.1146/annurev.aa.23.090185.001125. 3, 10, 12

Duncan, R. A. (1979), Wave ducting of solar metre-wave radio emission as an explanation of fundamental/harmonic source coincidence and other anomalies., *Solar Phys.*, *63*(2), 389–398, doi:10.1007/BF00174543. 36

Ergun, R. E., D. Larson, R. P. Lin, J. P. McFadden, C. W. Carlson, K. A. Anderson, L. Muschietti, M. McCarthy, G. K. Parks, H. Reme, J. M. Bosqued, C. D'Uston, T. R. Sanderson, K. P. Wenzel, M. Kaiser, R. P. Lepping, S. D. Bale, P. Kellogg, and J.-L. Bougeret (1998), Wind Spacecraft Observations of Solar Impulsive Electron Events Associated with Solar Type III Radio Bursts, *Astrophys. J.*, *503*, 435–445, doi:10.1086/305954. 17, 18, 55, 58, 67, 70, 104

Esser, R., S. Fineschi, D. Dobrzycka, S. R. Habbal, R. J. Edgar, J. C. Raymond, J. L. Kohl, and M. Guhathakurta (1999), Plasma Properties in Coronal Holes Derived from Measurements of Minor Ion Spectral Lines and Polarized White Light Intensity, *Astrophys. J. Lett.*, *510*(1), L63–L67, doi:10.1086/311786. 35, 39, 41

Fox, N. J., M. C. Velli, S. D. Bale, R. Decker, A. Driesman, R. A. Howard, J. C. Kasper, J. Kinnison, M. Kusterer, D. Lario, M. K. Lockwood, D. J. McComas, N. E. Raouafi, and A. Szabo (2016), The Solar Probe Plus Mission: Humanity's First Visit to Our Star, *Space Sci. Rev.*, *204*(1-4), 7–48, doi:10.1007/s11214-015-0211-6. 5, 34

Ginzburg, V. L., and V. V. Zheleznyakov (1958), On the possible mechanisms of sporadic solar radio emission (radiation in an isotropic plasma), *Soviet Astronomy*, *2*, 653. 2, 36, 54

Goldman, M. V. (1983), Progress and problems in the theory of type III solar radio emission, *Solar Physics*, *89*, 403–442, doi:10.1007/BF00217259. 12, 54

Gopalswamy, N., S. Yashiro, N. Reginald, N. Thakur, B. J. Thompson, and Q. Gong (2018), Physical Conditions in the Solar Corona Derived from the Total Solar Eclipse Observations obtained on 2017 August 21 Using a Polarization Camera, in *American Astronomical Society Meeting Abstracts #231*, *American Astronomical Society Meeting Abstracts*, vol. 231, p. 220.08. 35

Graham, D., I. Cairns, O. Skjaeraasen, and P. Robinson (2012a), Three-dimensional electromagnetic strong turbulence: Dependence of the statistics and dynamics of strong turbulence on the electron to ion temperature ratio, *Physics of Plasmas*, *19*, doi:10.1063/1.3684672. 25

Graham, D., I. Cairns, and D. Malaspina (2012b), Evidence against the oscillating two-stream instability and spatial collapse of langmuir waves in solar type iii radio bursts, *The Astrophysical Journal Letters*, *753*, L18, doi:10.1088/2041-8205/753/1/L18. 25

Graham, D. B., and I. H. Cairns (2013), "electrostatic decay of langmuir/z-mode waves in type iii solar radio bursts", *Journal of Geophysical Research: Space Physics*, *118*(7), 3968–3984, doi:10.1002/jgra.50402. 54, 56

Grognard, R. J. M. (1975), Deficiencies of the asymptotic solutions commonly found in the quasilinear relaxation theory, *Australian Journal of Physics*, *28*, 731, doi:10.1071/PH750731. 21, 22, 29

Grognard, R. J.-M. (1982), Numerical simulation of the weak turbulence excited by a beam of electrons in the interplanetary plasma, *Solar Physics*, *81*, 173–180, doi:10.1007/BF00151988. 21, 23, 54, 55, 70, 103

Grognard, R. J.-M. (1984), Partial reconstruction of the initial conditions for streams of energetic electrons associated with a solar type III burst, *Solar Physics*, *94*, 165–170, doi:10.1007/BF00154818. 23, 24, 54, 55, 70, 103

Grognard, R. J. M. (1985), *Propagation of electron streams.*, pp. 253–286, in *McLean and Labrum* [1985]. 22, 29

Guhathakurta, M., A. Fludra, S. E. Gibson, D. Biesecker, and R. Fisher (1999), Physical properties of a coronal hole from a coronal diagnostic spectrometer, Mauna Loa Coronagraph, and LASCO observations during the Whole Sun Month, *J. Geophys. Res.*, *104*(A5), 9801–9808, doi:10.1029/1998JA900082. 35, 39, 42

Gurnett, D. A. (1978), Plasma waves near the sun: Advances possible with a solar probe, in *A Close-up of the Sun*, edited by M. Neugebauer and R. W. Davies, pp. 281–317. 23

Gurnett, D. A., and R. R. Anderson (1976), Electron Plasma Oscillations Associated with Type III Radio Bursts, *Science*, *194*(4270), 1159–1162, doi:10.1126/science.194.4270.1159. 23, 54

Gurnett, D. A., and R. R. Anderson (1977), Plasma wave electric fields in the solar wind: Initial results from Helios 1, *J. Geophys. Res.*, *82*(4), 632, doi:10.1029/JA082i004p00632. 23

Harding, J. C., I. H. Cairns, and D. B. Melrose (2020), Electron-Langmuir wave resonance in three dimensions, *Physics of Plasmas*, *27*(2), 020702, doi:10.1063/1.5139068. 70, 99

Hayes, A. P., A. Vourlidas, and R. A. Howard (2001), Deriving the Electron Density of the Solar Corona from the Inversion of Total Brightness Measurements, *Astrophys. J.*, *548*(2), 1081–1086, doi:10.1086/319029. 35, 39, 41

Hirayama, T. (1974), Theoretical Model of Flares and Prominences. I: Evaporating Flare Model, *Solar Phys.*, *34*(2), 323–338, doi:10.1007/BF00153671. 16

Hoyng, P., and D. B. Melrose (1977), Legendre expansion of the quasi-linear equations for anisotropic particles and Langmuir waves, *Astrophys. J.*, *218*, 866–880, doi:10.1086/155742. 26, 27, 55, 57, 70

Isenberg, P. A. (2001), Heating of Coronal Holes and Generation of the Solar Wind by Ion-Cyclotron Resonance, *Space Sci. Rev.*, *95*, 119–131. 5

Jaeger, J. C., and K. C. Westfold (1949), Transients in an Ionized Medium with Applications to Bursts of Solar Noise, *Australian Journal of Scientific Research A Physical Sciences*, *2*, 322, doi:10.1071/PH490322. 11

Jones, S. I., and J. M. Davila (2009), Localized Plasma Density Enhancements Observed in STEREO COR1, *Astrophys. J.*, *701*(2), 1906–1910, doi:10.1088/0004-637X/701/2/1906. 45, 46

Klimchuk, J. A. (2006), On Solving the Coronal Heating Problem, *Solar Phys.*, *234*(1), 41–77, doi:10.1007/s11207-006-0055-z. 4

Ko, Y.-K., J. C. Raymond, J. Li, A. Ciaravella, J. Michels, S. Fineschi, and R. Wu (2002), Solar and Heliospheric Observatory Ultraviolet Coronagraph Spectrometer and Yohkoh Soft X-Ray Telescope Observations of the High-Temperature Corona above an Active Region Complex, *Astrophys. J.*, *578*(2), 979–995, doi:10.1086/342616. 35, 39

Kohl, J. L., G. Noci, E. Antonucci, G. Tondello, M. C. E. Huber, S. R. Cranmer, L. Strachan, A. V. Panasyuk, L. D. Gardner, M. Romoli, S. Fineschi, D. Dobrzycka, J. C. Raymond, P. Nicolosi, O. H. W. Siegmund, D. Spadaro, C. Benna, A. Ciaravella, S. Giordano, S. R. Habbal, M. Karovska, X. Li, R. Martin, J. G. Michels, A. Modigliani, G. Naletto, R. H. O'Neal, C. Pernechele, G. Poletto, P. L. Smith, and R. M. Suleiman (1998), UVCS/SOHO Empirical Determinations of Anisotropic Velocity Distributions in the Solar Corona, *Astrophys. J. Lett.*, *501*(1), L127–L131, doi:10.1086/311434. 35, 39, 41, 42, 46

Kontar, E. P. (2001), Dynamics of electron beams in the inhomogeneous solar corona plasma, *Solar Phys.*, *202*(1), 131–149, doi:10.1023/A:1011894830942. 74, 77, 111, 119

Kontar, E. P., V. I. Lapshin, and V. N. Mel'nik (1998), Numerical and analytical study of the propagation of a monoenergetic electron beam in a plasma, *Plasma Physics Reports*, *24*(9), 772–776. 23

Kontar, E. P., S. Yu, A. A. Kuznetsov, A. G. Emslie, B. Alcock, N. L. S. Jeffrey, V. N. Melnik, N. H. Bian, and P. Subramanian (2017), Imaging spectroscopy of solar radio burst fine structures, *Nature Communications*, *8*, 1515, doi:10.1038/s41467-017-01307-8. 36

Kopp, R. A., and G. W. Pneuman (1976), Magnetic reconnection in the corona and the loop prominence phenomenon., *Solar Phys.*, *50*(1), 85–98, doi:10.1007/BF00206193. 16

Lang, K. R. (2001), *The Cambridge Encyclopedia of the Sun*, Cambridge University Press. 4

Lang, K. R. (2006), *The Violent Sun, in Sun, Earth and Sky*, pp. 136–163, Springer-Verlag New York, doi:10.1007/978-0-387-33365-6. 16

Leblanc, Y., G. A. Dulk, and J.-L. Bougeret (1998), Tracing the Electron Density from the Corona to 1au, *Solar Phys.*, *183*(1), 165–180, doi:10.1023/A:1005049730506. 37

Lee, S.-Y., L. F. Ziebell, P. H. Yoon, R. Gaelzer, and E. S. Lee (2019), Particle-in-cell and Weak Turbulence Simulations of Plasma Emission, *Astrophys. J.*, *871*(1), 74, doi:10.3847/1538-4357/aaf476. 108, 110

Li, B., and I. Cairns (2014), Fundamental emission of type iii bursts produced in non-maxwellian coronal plasmas with kappa-distributed background particles, *Solar Physics*, *289*, doi:10.1007/s11207-013-0375-8. 12, 66, 122

Li, B., and I. H. Cairns (2013), Type III bursts produced by power law injected electrons in Maxwellian background coronal plasmas, *Journal of Geophysical Research (Space Physics)*, *118*, 4748–4759, doi:10.1002/jgra.50445. 12

Li, B., P. A. Robinson, and I. H. Cairns (2002), Multiple electron beam propagation and Langmuir wave generation in plasmas, *Physics of Plasmas*, *9*(7), 2976–2987, doi:10.1063/1.1485973. 70, 74, 82, 111, 119

Li, B., I. H. Cairns, and P. A. Robinson (2008), Simulations of coronal type iii solar radio bursts: 2. dynamic spectrum for typical parameters, *Journal of Geophysical Research: Space Physics*, *113*(A6), doi:10.1029/2007JA012958. 12, 21, 66

Li, B., I. H. Cairns, and P. A. Robinson (2008), Simulations of coronal type III solar radio bursts: 1. Simulation model, *Journal of Geophysical Research (Space Physics)*, *113*(A6), A06104, doi:10.1029/2007JA012957. 36, 70, 119

Lin, R. P., D. W. Potter, D. A. Gurnett, and F. L. Scarf (1981), Energetic electrons and plasma waves associated with a solar type III radio burst, *Astrophys. J.*, *251*, 364–373, doi:10.1086/159471. 15, 23, 54, 55, 67, 104

Lin, R. P., R. A. Mewaldt, and M. A. I. Van Hollebeke (1982), The energy spectrum of 20 keV - 20 MeV electrons accelerated in large solar flares., *Astrophys. J.*, *253*, 949–962, doi:10.1086/159693. 15, 70

Lin, R. P., B. R. Dennis, G. J. Hurford, D. M. Smith, A. Zehnder, P. R. Harvey, D. W. Curtis, D. Pankow, P. Turin, M. Bester, A. Csillaghy, M. Lewis, N. Madden, H. F. van Beek, M. Appleby, T. Raudorf, J. McTiernan, R. Ramaty, E. Schmahl, R. Schwartz, S. Krucker, R. Abiad, T. Quinn, P. Berg, M. Hashii, R. Sterling, R. Jackson, R. Pratt, R. D. Campbell, D. Malone, D. Landis, C. P. Barrington-Leigh, S. Slassi-Sennou, C. Cork, D. Clark, D. Amato, L. Orwig, R. Boyle, I. S. Banks, K. Shirey, A. K. Tolbert, D. Zarro, F. Snow, K. Thomsen, R. Henneck, A. McHedlishvili, P. Ming, M. Fivian, J. Jordan, R. Wanner, J. Crubb, J. Preble, M. Matranga, A. Benz, H. Hudson, R. C. Canfield, G. D. Holman, C. Crannell, T. Kosugi, A. G. Emslie, N. Vilmer, J. C. Brown, C. Johns-Krull, M. Aschwanden, T. Metcalf, and A. Conway (2002), The Reuven Ramaty High-Energy Solar Spectroscopic Imager (RHESSI), *Solar Phys.*, *210*(1), 3–32, doi:10.1023/A:1022428818870. 16

Lobzin, V. V., I. H. Cairns, and P. A. Robinson (2008), Evidence for Wind-like Regions, Acceleration of Shocks in the Deep Corona, and Relevance of 1/f Dynamic Spectra to Coronal Type II Bursts, *Astrophys. J. Lett.*, *677*(2), L129, doi:10.1086/587980. 36, 38

Lobzin, V. V., I. H. Cairns, P. A. Robinson, A. Warmuth, G. Mann, R. V. Gorgutsa, and V. V. Fomichev (2010), Evidence for Gently Sloping Plasma Density Profiles in the Deep Corona: Type III Observations, *Astrophys. J.*, *724*(2), 1099–1107, doi:10.1088/0004-637X/724/2/1099. 36, 47, 48

Magdalenić, J., C. Marqué, A. N. Zhukov, B. Vršnak, and T. Žic (2010), Origin of Coronal Shock Waves Associated with Slow Coronal Mass Ejections, *Astrophys. J.*, *718*(1), 266–278, doi:10.1088/0004-637X/718/1/266. 39, 41, 42, 47

Magelssen, G. R., and D. F. Smith (1977), Nonrelativistic electron stream propagation in the solar atmosphere and type III radio bursts., *Solar Phys.*, *55*(1), 211–240, doi:10.1007/BF00150886. 23

Maksimovic, M., V. Pierrard, and P. Riley (1997), Ulysses electron distributions fitted with kappa functions, *Geophysical Research Letters*, *24*(9), 1151–1154, doi:10.1029/97GL00992. 54

Malmberg, J. H., and C. B. Wharton (1969), Spatial growth of waves in a beam-plasma System, *Physics of Fluids*, *12*, 2600–2606, doi:10.1063/1.1692402. 54

Manchester, I., Ward B., A. Vourlidas, G. Tóth, N. Lugaz, I. I. Roussev, I. V. Sokolov, T. I. Gombosi, D. L. De Zeeuw, and M. Opher (2008), Three-dimensional MHD Simulation of the 2003 October 28 Coronal Mass Ejection: Comparison with LASCO Coronagraph Observations, *Astrophys. J.*, *684*(2), 1448–1460, doi:10.1086/590231. 35

Mann, G., F. Breitling, C. Vocks, H. Aurass, M. Steinmetz, K. G. Strassmeier, M. M. Bisi, R. A. Fallows, P. Gallagher, A. Kerdraon, A. Mackinnon, J. Magdalenic, H. Rucker, J. Anderson, A. Asgekar, I. M. Avruch, M. E. Bell, M. J. Bentum, G. Bernardi, P. Best, L. Bîrzan, A. Bonafede, J. W. Broderick, M. Brüggen, H. R. Butcher, B. Ciardi, A. Corstanje, F. de Gasperin, E. de Geus, A. Deller, S. Duscha, J. Eislöffel, D. Engels, H. Falcke, R. Fender, C. Ferrari, W. Frieswijk, M. A. Garrett, J. Grießmeier, A. W. Gunst, M. van Haarlem, T. E. Hassall, G. Heald, J. W. T. Hessels, M. Hoeft, J. Hörandel, A. Horneffer, E. Juette, A. Karastergiou, W. F. A. Klijn, V. I. Kondratiev, M. Kramer, M. Kuniyoshi, G. Kuper, P. Maat, S. Markoff, R. McFadden, D. McKay-Bukowski, J. P. McKean, D. D. Mulcahy, H. Munk, A. Nelles, M. J. Norden, E. Orru, H. Paas, M. Pandey-Pommier, V. N. Pandey, R. Pizzo, A. G. Polatidis, D. Rafferty, W. Reich, H. Röttgering, A. M. M. Scaife, D. J. Schwarz, M. Serylak, J. Sluman, O. Smirnov, B. W. Stappers, M. Tagger, Y. Tang, C. Tasse, S. ter Veen, S. Thoudam, M. C. Toribio, R. Vermeulen, R. J. van Weeren, M. W. Wise, O. Wucknitz, S. Yatawatta, P. Zarka, and J. A. Zensus (2018), Tracking of an electron beam through the solar corona with LOFAR, *Astron. Astrophys.*, *611*, A57, doi:10.1051/0004-6361/201629017. 36, 49

McCauley, P. I., I. H. Cairns, J. Morgan, S. E. Gibson, J. C. Harding, C. Lonsdale, and D. Oberoi (2017), Type III Solar Radio Burst Source Region Splitting due to a Quasi-separatrix Layer, *Astrophys. J.*, *851*(2), 151, doi:10.3847/1538-4357/aa9cee. 36, 49

McCauley, P. I., I. H. Cairns, and J. Morgan (2018), Densities Probed by

Coronal Type III Radio Burst Imaging, *Solar Phys.*, *293*(10), 132, doi:10.1007/s11207-018-1353-y. 12, 13, 36, 38, 49, 119

McLean, D. J., and N. R. Labrum (1985), *Solar radiophysics : studies of emission from the sun at metre wavelengths*, Cambridge University Press. 1, 7, 10, 131, 140

Mel'Nik, V. N., V. Lapshin, and E. Kontar (1999), Propagation of a Monoenergetic Electron Beam in the Solar Corona, *Solar Phys.*, *184*(2), 353–362, doi:10.1023/A:1005191910544. 21, 23, 70

Melrose, D. B. (1970), On the theory of type II and type III solar radio bursts. I. The impossibility of nonthermal emission due to combination scattering off thermal fluctuations, *Australian Journal of Physics*, *23*, 871, doi:10.1071/PH700871. 9, 82

Melrose, D. B. (1975), Plasma emission due to isotropic fast electrons, and types I, II, and V solar radio bursts, *Solar Phys.*, *43*(1), 211–236, doi:10.1007/BF00155154. 85, 86

Melrose, D. B. (1982), Fundamental emission for Type-III bursts in the interplanetary medium - the role of ion-sound turbulence, *Solar Physics*, *79*(1), 173–185, doi:10.1007/BF00146981. 54

Melrose, D. B. (1983), Prompt Acceleration of Greater than or Approximately Equal to 30-MEV Per Nucleon Ions in Solar Flares, *Solar Phys.*, *89*(1), 149–162, doi:10.1007/BF00211959. 15

Melrose, D. B. (1986), *Instabilities in Space and Laboratory Plasmas*, 288 pp., Cambridge University Press, doi:10.1017/CBO9780511564123. 20, 24, 35, 54, 70

Melrose, D. B. (1990), Particle acceleration processes in the solar corona, *Australian Journal of Physics*, *43*(6), 703–752, doi:10.1071/PH900703. 12, 15, 23

Melrose, D. B. (2009), Coherent emission, in *Universal Heliophysical Processes*, *IAU Symposium*, vol. 257, edited by N. Gopalswamy and D. F. Webb, pp. 305–315, doi:10.1017/S1743921309029470. 11, 17

Melrose, D. B., and N. F. Cramer (1989), Quasi-linear relaxation of electrons interacting with an inhomogeneous distribution of Langmuir waves, *Solar Phys.*, *123*(2), 343–356, doi:10.1007/BF00149110. 23

Melrose, D. B., and G. A. Dulk (1987), Solar radio bursts with special regard to particle acceleration and mass ejection., *Physica Scripta Volume T*, *18*, 29–38, doi:10.1088/0031-8949/1987/T18/003. 15

Melrose, D. B., and J. E. Stenhouse (1977), Emission and absorption of Langmuir waves by anisotropic unmagnetized particles, *Australian Journal of Physics*, *30*, 481–493, doi:10.1071/PH770481. 26, 27, 55, 57, 70, 87

Müller, D., R. G. Marsden, O. C. St. Cyr, and H. R. Gilbert (2013), Solar Orbiter . Exploring the Sun-Heliosphere Connection, *Solar Phys.*, *285*(1-2), 25–70, doi:10.1007/s11207-012-0085-7. 5, 34

Munro, R. H., and B. V. Jackson (1977), Physical properties of a polar coronal hole from 2 to 5 R sun., *Astrophys. J.*, *213*, 874, doi:10.1086/155220. 35, 39, 41

Muschietti, L. (1990), Electron Beam Formation and Stability, *Solar Phys.*, *130*(1-2), 201–228, doi:10.1007/BF00156790. 17, 24

Newkirk, J., Gordon (1961), The Solar Corona in Active Regions and the Thermal Origin of the Slowly Varying Component of Solar Radio Radiation., *Astrophys. J.*, *133*, 983, doi:10.1086/147104. 5, 37

Nishikawa, K. (1968), Parametric Excitation of Coupled Waves I. General Formulation, *Journal of the Physical Society of Japan*, *24*(4), 916–922, doi:10.1143/JPSJ.24.916. 24

O'Neil, T. M., and J. H. Malmberg (1968), Transition of the dispersion roots from beam type to landau type solutions, *The Physics of Fluids*, *11*(8), 1754–1760, doi:10.1063/1.1692190. 54

Papadopoulos, K., M. L. Goldstein, and R. A. Smith (1974), Stabilization of electron streams in Type III solar radio bursts, *Astrophys. J.*, *190*, 175–186, doi:10.1086/152862. 25, 54, 56

Parker, E. N. (1958), Dynamics of the Interplanetary Gas and Magnetic Fields., *Astrophys. J.*, *128*, 664, doi:10.1086/146579. 4, 37, 45, 46

Parker, E. N. (1963), *Interplanetary dynamical processes.*, New York, : Interscience Publishers. 6

Pelletier, G. (1982), Generation of a high-energy electron tail by strong Langmuir turbulence in a plasma, *Phys. Rev. Lett.*, *49*(11), 782–785, doi: 10.1103/PhysRevLett.49.782. 25

Ramaty, R., C. Paizis, S. A. Colgate, G. A. Dulk, P. Hoyng, J. W. Knight, R. P. Lin, D. B. Melrose, F. Orrall, and P. R. Shapiro (1980), Energetic particles in solar flares, in *Skylab Solar Workshop II*, edited by P. A. Sturrock, pp. 117–185. 15

Ratcliffe, H., E. P. Kontar, and H. A. S. Reid (2014), Large-scale simulations of solar type III radio bursts: flux density, drift rate, duration, and bandwidth, *A&A*, *572*, A111, doi:10.1051/0004-6361/201423731. 66, 70

Reid, H. A. S., and H. Ratcliffe (2014), A review of solar type III radio bursts, *Research in Astronomy and Astrophysics*, *14*, 773–804, doi: 10.1088/1674-4527/14/7/003. 12, 14, 17, 54

Reiner, M. J., M. L. Kaiser, and J. L. Bougeret (2001), Radio signatures of the origin and propagation of coronal mass ejections through the solar corona and interplanetary medium, *J. Geophys. Res.*, *106*(A12), 29,989–30,000, doi:10.1029/2000JA002228. 36

Robinson, P. A. (1993), Stochastic Growth Theory of Langmuir Growth-Rate Fluctuations in Type-Iii Solar Radio Sources, *Solar Phys.*, *146*(2), 357–363, doi:10.1007/BF00662019. 17, 56

Robinson, P. A., and I. H. Cairns (1993), Stochastic Growth Theory of Type III Solar Radio Emission, *Astrophys. J.*, *418*, 506, doi:10.1086/173412. 24

Robinson, P. A., and I. H. Cairns (1998), Fundamental and Harmonic Emission in Type III Solar Radio Bursts - I. Emission at a Single Location or Frequency, *Solar Phys.*, *181*(2), 363–394, doi:10.1023/A:1005018918391. 36, 54

Robinson, P. A., and I. H. Cairns (2000), Theory of Type III And Type II Solar Radio Emissions, *Washington DC American Geophysical Union Geophysical Monograph Series*, *119*, 37, doi:10.1029/GM119p0037. 12, 17

Robinson, P. A., I. H. Cairns, and D. A. Gurnett (1992), Connection between ambient density fluctuations and clumpy Langmuir waves in type III radio sources, *Astrophys. J.*, *387*, L101–L104, doi:10.1086/186315. 8, 24, 56

Robinson, P. A., I. H. Cairns, and D. A. Gurnett (1993a), Clumpy Langmuir Waves in Type III Radio Sources: Comparison of Stochastic-Growth Theory with Observations, *Astrophys. J.*, *407*, 790, doi:10.1086/172560. 21

Robinson, P. A., A. J. Willes, and I. H. Cairns (1993b), Dynamics of Langmuir and Ion-Sound Waves in Type III Solar Radio Sources, *Astrophys. J.*, *408*, 720, doi:10.1086/172632. 24

Robinson, P. A., I. H. Cairns, and A. J. Willes (1994), Dynamics and Efficiency of Type III Solar Radio Emission, *Astrophys. J.*, *422*, 870, doi:10.1086/173779. 24

Robinson, R. D. (1975), A study of meter wavelength continuum radiation from the sun, Ph.D. thesis, University of Colorado. 85, 86, 87

Robinson, R. D. (1978), The emission of Langmuir waves in the solar corona., *Astrophys. J.*, *222*, 696–706, doi:10.1086/156188. 86

Ryutov, D. D., and R. Z. Sagdeev (1970), Quasi-gasdynamical Description of a Hot Electron Cloud in a Cold Plasma, *Soviet Journal of Experimental and Theoretical Physics*, *31*, 396. 21, 23

Saito, K., A. I. Poland, and R. H. Munro (1977), A study of the background corona near solar minimum., *Solar Phys.*, *55*(1), 121–134, doi:10.1007/BF00150879. 35, 37, 41, 49

Schmidt, J. M., and I. H. Cairns (2016), Quantitative prediction of type II solar radio emission from the Sun to 1 AU, *Geophys. Res. Lett.*, *43*(1), 50–57, doi:10.1002/2015GL067271. 35

Schulte in den Bäumen, H., I. H. Cairns, and P. A. Robinson (2012), Nonzero azimuthal magnetic fields at the solar source surface: Extraction, model, and implications, *Journal of Geophysical Research (Space Physics)*, *117*(A10), A10104, doi:10.1029/2012JA017705. 5

Schutz, H., and R. A. Karsten (1973), *Solar Probe Helios, Mission Requirements & Applied Space Simulation Techniques*, vol. 336, p. 671. 5

Sheeley, N. R., Y. M. Wang, S. H. Hawley, G. E. Brueckner, K. P. Dere, R. A. Howard, M. J. Koomen, C. M. Korendyke, D. J. Michels, S. E. Paswaters, D. G. Socker, O. C. St. Cyr, D. Wang, P. L. Lamy, A. Llebaria, R. Schwenn, G. M. Simnett, S. Plunkett, and D. A. Biesecker (1997), Measurements of

Flow Speeds in the Corona Between 2 and 30 $R_\odot$, *Astrophys. J.*, *484*(1), 472–478, doi:10.1086/304338. 45, 46

Smerd, S. F., K. V. Sheridan, and R. T. Stewart (1975), Split-Band Structure in Type II Radio Bursts from the Sun, *Astrophysical Letters*, *16*, 23. 15

Stasiewicz, K. (2006), Heating of the Solar Corona by Dissipative Alfvén Solitons, *Phys. Rev. Lett.*, *96*(17), 175003, doi:10.1103/PhysRevLett.96.175003. 5

Strachan, L., R. Suleiman, A. V. Panasyuk, D. A. Biesecker, and J. L. Kohl (2002), Empirical Densities, Kinetic Temperatures, and Outflow Velocities in the Equatorial Streamer Belt at Solar Minimum, *Astrophys. J.*, *571*(2), 1008–1014, doi:10.1086/339984. 35, 39, 41, 44, 45, 46, 47

Strachan, L., A. V. Panasyuk, J. L. Kohl, and P. Lamy (2012), The Evolution of Plasma Parameters on a Coronal Source Surface at 2.3 $R_\odot$ during Solar Minimum, *Astrophys. J.*, *745*(1), 51, doi:10.1088/0004-637X/745/1/51. 45

Sturrock, P. A. (1964), Type III Solar Radio Bursts, *NASA Special Publication*, *50*, 357. 11, 17, 21, 23, 55

Sturrock, P. A. (1966), Model of the High-Energy Phase of Solar Flares, *Nature*, *211*(5050), 695–697, doi:10.1038/211695a0. 15

Suzuki, S., and G. A. Dulk (1985), *Bursts of type III and type V.*, pp. 289–332, in *McLean and Labrum* [1985]. 36

Takakura, T., and H. Shibahashi (1976), Dynamics of a Cloud of Fast Electrons Travelling Through the Plasma, *Solar Phys.*, *46*(2), 323–346, doi:10.1007/BF00149860. 23

Tasnim, S., and I. H. Cairns (2016), An equatorial solar wind model with angular momentum conservation and nonradial magnetic fields and flow velocities at an inner boundary, *Journal of Geophysical Research (Space Physics)*, *121*(6), 4966–4984, doi:10.1002/2016JA022725. 5, 44

Tasnim, S., I. H. Cairns, and M. S. Wheatland (2018), A Generalized Equatorial Model for the Accelerating Solar Wind, *Journal of Geophysical Research (Space Physics)*, *123*(2), 1061–1085, doi:10.1002/2017JA024532. 5

Thejappa, G., and R. J. MacDowall (2008), Effects of Scattering on Radio Emission from the Quiet Sun at Low Frequencies, *Astrophys. J.*, *676*(2), 1338–1345, doi:10.1086/528835. 36

Thejappa, G., D. Lengyel-Frey, R. G. Stone, and M. L. Goldstein (1993), Evaluation of Emission Mechanisms at omega P E Using ULYSSES Observations of Type III Bursts, *Astrophys. J.*, *416*, 831, doi:10.1086/173281. 25

Thejappa, G., R. J. MacDowall, and M. Bergamo (2013), Observational evidence for the collapsing Langmuir wave packet in a solar type III radio burst, *Journal of Geophysical Research (Space Physics)*, *118*(7), 4039–4052, doi:10.1002/jgra.50441. 25

Tu, C.-Y., C. Zhou, E. Marsch, L.-D. Xia, L. Zhao, J.-X. Wang, and K. Wilhelm (2005), Solar Wind Origin in Coronal Funnels, *Science*, *308*(5721), 519–523, doi:10.1126/science.1109447. 44

Usmanov, A. V., W. H. Matthaeus, B. A. Breech, and M. L. Goldstein (2011), Solar Wind Modeling with Turbulence Transport and Heating, *Astrophys. J.*, *727*(2), 84, doi:10.1088/0004-637X/727/2/84. 5

Varah, J. M. (1972), On the solution of block-tridiagonal systems arising from certain finite-difference equations, *Mathematics of Computation*, *26*(120), 859–868. 80, 123

Vedenov, A. A., E. P. Velikhov, and R. Z. Sagdeev (1961), Nonlinear oscillations of rarified plasma, *Nuclear Fusion*, *1*, 82. 54

Vernazza, J. E., E. H. Avrett, and R. Loeser (1973), Structure of the Solar Chromosphere. Basic Computations and Summary of the Results, *Astrophys. J.*, *184*, 605–632, doi:10.1086/152353. 4

Voshchepynets, A., V. Krasnoselskikh, A. Artemyev, and A. Volokitin (2015), Probabilistic Model of Beam-Plasma Interaction in Randomly Inhomogeneous Plasma, *Astrophys. J.*, *807*(1), 38, doi:10.1088/0004-637X/807/1/38. 62

Wenzel, K. P., G. R. Marsden, E. D. Page, and J. E. Smith (1990), The First High-Latitude Heliospheric Mission: Ulysses, in *International Cosmic Ray Conference*, *International Cosmic Ray Conference*, vol. 7, p. 252. 5

Wild, J. P. (1950), Observations of the Spectrum of High-Intensity Solar Radiation at Metre Wavelengths. II. Outbursts, *Australian Journal of Scientific Research A Physical Sciences*, *3*, 399, doi:10.1071/PH500399. 11

Wild, J. P., and L. L. McCready (1950), Observations of the Spectrum of High-Intensity Solar Radiation at Metre Wavelengths. I. The Apparatus and Spectral Types of Solar Burst Observed, *Australian Journal of Scientific Research A Physical Sciences*, *3*, 387, doi:10.1071/PH500387. 1, 10, 36, 54

Wild, J. P., S. F. Smerd, and A. A. Weiss (1963), Solar Bursts, *Ann. Rev. Astron. Astrophys.*, *1*, 291, doi:10.1146/annurev.aa.01.090163.001451. 12

Withbroe, G. L. (1988), The Temperature Structure, Mass, and Energy Flow in the Corona and Inner Solar Wind, *Astrophys. J.*, *325*, 442, doi:10.1086/166015. 35, 39

Zaitsev, V. V., N. A. Mityakov, and V. O. Rapoport (1972), A Dynamic Theory of Type III Solar Radio Bursts, *Solar Phys.*, *24*(2), 444–456, doi:10.1007/BF00153387. 21, 23

Zakharov, V., S. Musher, and A. Rubenchik (1985), Hamiltonian approach to the description of non-linear plasma phenomena, *Physics Reports*, *129*(5), 285 – 366, doi:https://doi.org/10.1016/0370-1573(85)90040-7. 25, 54

Zakharov, V. E., and A. B. Shabat (1972), Exact theory of two-dimensional self-focusing and one-dimensional self-modulation of waves in nonlinear media, *Soviet Journal of Experimental and Theoretical Physics*, *34*, 62. 24, 54

Zharkova, V. V., K. Arzner, A. O. Benz, P. Browning, C. Dauphin, A. G. Emslie, L. Fletcher, E. P. Kontar, G. Mann, M. Onofri, V. Petrosian, R. Turkmani, N. Vilmer, and L. Vlahos (2011), Recent Advances in Understanding Particle Acceleration Processes in Solar Flares, *Space Sci. Rev.*, *159*(1-4), 357–420, doi:10.1007/s11214-011-9803-y. 17

Ziebell, L. F., R. Gaelzer, J. Pavan, and P. H. Yoon (2008a), Two-dimensional nonlinear dynamics of beam plasma instability, *Plasma Physics and Controlled Fusion*, *50*(8), 085011, doi:10.1088/0741-3335/50/8/085011. 29, 55

Ziebell, L. F., R. Gaelzer, and P. H. Yoon (2008b), Dynamics of Langmuir wave decay in two dimensions, *Physics of Plasmas*, *15*(3), 032303, doi:10.1063/1.2844740. 29, 30, 55

Ziebell, L. F., P. H. Yoon, J. Pavan, and R. Gaelzer (2011), Two-dimensional quasilinear beam-plasma instability in inhomogeneous media, *Plasma Physics and Controlled Fusion*, *53*(8), 085004, doi:10.1088/0741-3335/53/8/085004. 29, 55

Ziebell, L. F., P. H. Yoon, R. Gaelzer, and J. Pavan (2014), Plasma Emission by Weak Turbulence Processes, *Astrophys. J. Lett.*, *795*(2), L32, doi:10.1088/2041-8205/795/2/L32. 29

Ziebell, L. F., P. H. Yoon, L. T. Petruzzellis, R. Gaelzer, and J. Pavan (2015), Plasma Emission by Nonlinear Electromagnetic Processes, *Astrophys. J.*, *806*(2), 237, doi:10.1088/0004-637X/806/2/237. 29

Zucca, P., E. P. Carley, D. S. Bloomfield, and P. T. Gallagher (2014), The formation heights of coronal shocks from 2D density and Alfvén speed maps, *Astron. Astrophys.*, *564*, A47, doi:10.1051/0004-6361/201322650. 36, 49

Zucca, P., D. E. Morosan, A. P. Rouillard, R. Fallows, P. T. Gallagher, J. Magdalenic, K. L. Klein, G. Mann, C. Vocks, E. P. Carley, M. M. Bisi, E. P. Kontar, H. Rothkaehl, B. Dabrowski, A. Krankowski, J. Anderson, A. Asgekar, M. E. Bell, M. J. Bentum, P. Best, R. Blaauw, F. Breitling, J. W. Broderick, W. N. Brouw, M. Brüggen, H. R. Butcher, B. Ciardi, E. de Geus, A. Deller, S. Duscha, J. Eislöffel, M. A. Garrett, J. M. Grießmeier, A. W. Gunst, G. Heald, M. Hoeft, J. Hörandel, M. Iacobelli, E. Juette, A. Karastergiou, J. van Leeuwen, D. McKay-Bukowski, H. Mulder, H. Munk, A. Nelles, E. Orru, H. Paas, V. N. Pand ey, R. Pekal, R. Pizzo, A. G. Polatidis, W. Reich, A. Rowlinson, D. J. Schwarz, A. Shulevski, J. Sluman, O. Smirnov, C. Sobey, M. Soida, S. Thoudam, M. C. Toribio, R. Vermeulen, R. J. van Weeren, O. Wucknitz, and P. Zarka (2018), Shock location and CME 3D reconstruction of a solar type II radio burst with LOFAR, *Astron. Astrophys.*, *615*, A89, doi:10.1051/0004-6361/201732308. 36, 49